

OPTICAL FORCES GENERATED BY PLASMONIC NANOSTRUCTURES

by

MATTHEW MOOCARME

A dissertation submitted to the Graduate Faculty in Physics in partial fulfillment of the requirements for the degree of Doctor of Philosophy, The City University of New York

2017

© 2015

MATTHEW MOOCARME

All Rights Reserved

This manuscript has been read and accepted by the Graduate Faculty in Physics in satisfaction of the dissertation requirement for the degree of Doctor of Philosophy.

**Professor L.T.Vuong**

---

**Professor Vinod Menon**

**Professor Azriel Genack**

**Professor Harry Gafney**

**Dr Aaron Stein**

Supervisory Committee

## Abstract

OPTICAL FORCES GENERATED BY PLASMONIC NANOSTRUCTURES

by

MATTHEW MOOCARME

Adviser: Professor L.T. Vuong

This dissertation consists of four chapters representing the four first author papers published during my Ph.D. program.

**Chapter 1** Magneto-plasmonics is a designation generally associated with ferromagnetic-plasmonic materials because such optical responses from nonmagnetic materials alone are considered weak. Here, we show that there exists a switching transition between linear and nonlinear magneto-optical behaviors in noble-metal nanocolloids that is observable at ultralow illumination intensities and direct current magnetic fields. The response is attributed to polarization-dependent nonzero-time-averaged plasmonic loops, vortex power flows, and nanoparticle magnetization. This work identifies significant mechanical effects that subsequently exist via magnetic-dipole interactions.

**Chapter 2** The mechanical forces associated with surface currents are widely overlooked and point to a new family of plasmonically-driven processes. Here, we investigate the Lorentz forces acting on a free electron gas that is bound to the surface of a nanowire. We demonstrate that appreciable mechanical forces are produced by longer illumination wavelengths between longitudinal and transverse absorption resonances via the excitation of chiral hybrid plasmon modes. We are the first to associate plasmonic activity as the underlying mechanism for nanowire rotation, which explains prior experimental results.

The presence of chiral hybrid plasmon modes yields the greatest net translation and torque forces. The asymmetric plasmon behavior subsequently affects the complex nonlinear dynamics of plasmonic nonspherical nanoparticles in fluids.

**Chapter 3** When plane waves diffract through fractal-patterned apertures, the resulting far-field profiles or diffractals also exhibit iterated, self-similar features. Here we show that this specific architecture enables robust signal processing and spatial multiplexing: arbitrary parts of a diffractal contain sufficient information to recreate the entire original sparse signal.

**Chapter 4** The response of an individual meta-atom is often generalized to explain the collective response of a metasurface in a manner that neglects the interactions between meta-atoms. Here, we study a metasurface composed of tilted achiral meta-atoms with no spatial variation of the unit-cell that derives appreciable optical chirality solely from the asymmetric interactions between meta-atoms. The interactions between meta-atoms are considered to stem from the Lorentz force arising from the Larmor radiation of adjacent plasmonic resonators because their inclusion in a simple model accurately predicts the bonding/anti-bonding modes that are measured experimentally. We also experimentally observe the emergence of multiple polarization eigenmodes, among other polarization-dependent responses, which cannot be modeled with the conventional formalism of transmission matrices. Our results are vital to the precise characterization and design of metasurfaces.

# Acknowledgments

Heartfelt thanks my adviser Prof. Luat Vuong for unlimited support, ideas and pizza. Sincerest of thanks to committee members Prof. Menon, Prof. Genack and Prof. Gafney for their humble guidance, and Dr Stein for candid support at Brookhaven National Laboratory. Finally, thanks to fellow grad students, especially Nicolas Proscia, for their interest and valuable discussions.

# Contents

<b>Contents</b>	vii
<b>List of Figures</b>	x
<b>Nomenclature</b>	xv
<b>1 Ultra-low-intensity magneto-optical and mechanical effects in metal nanocolloids</b>	1
1.1 Introduction . . . . .	1
1.2 Linear Dynamics . . . . .	4
1.2.1 Addition of Magnetic Fields to Equations of Motion . . . . .	4
1.3 Nonlinear Dynamics . . . . .	5
1.3.1 Nonlinear Current Density . . . . .	5
1.3.2 Nonlinear Magnetization . . . . .	6
1.4 Numerical Predictions . . . . .	8
1.4.1 Finite-element simulation Results . . . . .	8
1.5 Experimental Observation . . . . .	8
1.5.1 Observation of Transition from Linear to Nonlinear Dynamics . . .	8
1.6 Discussion . . . . .	11
1.6.1 Magnetization Magnitudes . . . . .	11

1.6.2	Time-Dependent Response . . . . .	11
1.7	Conclusion . . . . .	14
1.8	Experimental Difficulties and Future Work . . . . .	14
<b>2</b>	<b>Plasmon-induced Lorentz forces of nanowire chiral hybrid modes</b>	<b>16</b>
2.1	Introduction . . . . .	16
2.2	Setup and simulations of 2D dynamics . . . . .	19
2.2.1	Calculation of Electromagnetic Fields . . . . .	19
2.2.2	Calculation of Lorentz Force . . . . .	22
2.2.3	Calculation of Torque Forces . . . . .	23
2.3	Translation and compressive plasmonic forces . . . . .	25
2.3.1	Force Visualized for Various Illumination Wavelengths . . . . .	25
2.3.2	Momentum Transfer via Scattering . . . . .	28
2.4	Torque in 3-dimensions . . . . .	30
2.4.1	Torque Visualized for Various Illumination Wavelengths . . . . .	30
2.4.2	Phase Diagram Illustrations . . . . .	31
2.5	Conclusion . . . . .	33
2.6	Future Work . . . . .	34
<b>3</b>	<b>Robustness and spatial multiplexing via diffractal architectures</b>	<b>36</b>
3.1	Introduction . . . . .	36
3.2	Theoretical Description . . . . .	38
3.2.1	Spatial Multiplexing of the Diffractal . . . . .	38
3.2.2	Robust reconstruction of a blocked diffractal signal . . . . .	40
3.3	Experimental Results . . . . .	44
3.4	Discussion of Applications . . . . .	46

<i>CONTENTS</i>	ix
3.5 Conclusion . . . . .	48
3.6 Experimental Difficulties and Future Work . . . . .	50
<b>4 Meta-optical chirality and emergent eigen-polarization modes via plasmon interactions</b>	<b>51</b>
4.1 Introduction . . . . .	51
4.2 The coupling force . . . . .	55
4.3 Coupled equations of motion . . . . .	57
4.4 Mode hybridization and optical chirality . . . . .	59
4.5 Emergent polarization eigenmodes . . . . .	63
4.6 Discussion . . . . .	65
4.7 Conclusion . . . . .	66
4.8 Fabrication Methods and Measurement . . . . .	66
4.8.1 Development . . . . .	67
4.8.2 Recipe . . . . .	70
4.8.3 Transmission Measurement Setup . . . . .	72
4.8.4 Polarization Measurement Setup . . . . .	73
4.9 Experimental Difficulties and Future Work . . . . .	73
<b>Bibliography</b>	<b>75</b>

# List of Figures

1.1	Relative MO shift of bulk gold when external fields are varied. (a) Real and (b) imaginary parts of the refractive index as a function of wavelength under illumination of $1 \text{ W/cm}^2$ RHCP when magnetic fields are varied. . . . .	5
1.2	(a) Surface plots of the nonlinear current density of an aqueous 80-nm gold nanosphere when illuminated by LHCP, linearly-polarized and RHCP light in the $\hat{z}$ direction at the plasmon resonance, 540 nm, at $1 \text{ W/cm}^2$ . (b) Volume- averaged relative change in azimuthal component of the conductivity as a function of wavelength when illumination intensity is varied for RHCP or LHCP. . . . .	7
1.3	Normalized MO changes in transmission for aqueous gold nanocolloid at (a) low magnetic fields (b) intermediate magnetic fields and (c) higher mag- netic fields. Theoretical MO change in transmission of aqueous 80-nm gold nanospheres in the (d) linear and (f) nonlinear analyses. Theoretical MO changes that combine the linear and nonlinear analyses are shown in (e) for intermediate magnetic fields. In all plots the illumination is $1 \text{ W/cm}^2$ and RHCP. . . . .	9

1.4 Numerically calculated (a) amplitude and (b) phase of the longitudinal component of the electric field, $E_z$ , with 540-nm $1 \text{ W/cm}^2$ RHCP illumination intensity. (c) Volume-averaged magnetization as a function of wavelength when illumination intensities are varied. All plots are for an aqueous 80-nm gold nanoparticle. . . . .	12
1.5 Numerically calculated relative change in magnetization (a) of a 80-nm gold dimer nanocluster as a function of angle of rotation, and (b) ellipsoidal gold nanoparticle rotated from minimal to maximal surface area as a function of aspect ratio, illuminated with 540-nm $1 \text{ W/cm}^2$ RHCP. . . . .	13
2.1 (a) System geometry: a gold nanowire (75-nm diameter, rounded-cap, 1025-nm length) is aligned about spherical coordinates $\theta$ and $\phi$ , and a $y$ -polarized electromagnetic wave ( $1 \text{ W/cm}^2$ ) travels in the $-z$ direction. (b) The electric field profile surrounding a nanowire resulting from superposed angular momentum modes $m = 0, \pm 1$ with propagation lengths $k_{\parallel} z = 0, \pi/2$ , and $\pi$ . . . . .	20
2.2 Characteristics of a nanowire in the $x$ - $y$ plane for varying orientation angle $\phi$ with $\theta = 90^\circ$ . (a) Absorption cross-section. (b) Scattering cross-section, ((a), (b) spectra offset for clarity). (c) Net longitudinal force in the direction of light propagation, $-F_z$ , associated with the plasmonic Lorentz force. (d) In-plane torque $T_z$ produced by plasmons $\mathbf{f}_M$ (solid lines) and the induced electric dipole $\mathbf{f}_E$ (dashed lines). . . . .	24
2.3 Forces on the nanowire surface produced by the surface currents (red arrows) and the norm of the surface magnetic field (surface colormap) for oblique geometries that excite the chiral hybrid plasmonic mode, where (a) $\theta = 15^\circ, \phi = 90^\circ$ (b) $\theta = 30^\circ, \phi = 75^\circ$ (c) $\theta = 60^\circ, \phi = 60^\circ$ at $\lambda = 1071\text{nm}$ . . . . .	26

2.4 Net (volume-integrated) Lorentz forces associated with nanowire surface currents $\mathbf{f}_M$ in (a) $x$ -direction, (b) $y$ -direction, and (c) $z$ -directions for illuminating wavelengths $\lambda =$ (i) 441nm (ii) 517nm (iii) 625nm (iv) 790nm (v) 1071nm. . . . .	27
2.5 Far-field radiation patterns for a nanowire aligned (a) in the $x$ - $z$ plane with $\theta = 75^\circ, \phi = 0^\circ$ , (b) $\theta = 60^\circ, \phi = 60^\circ$ for wavelengths $\lambda = 441\text{nm}, 517\text{nm}, 625\text{nm}, 790\text{nm}$ , and 1071nm. . . . .	28
2.6 Torque around the (a) $x$ -axis, (b) $y$ -axis, and (c) $z$ -axis at (i) 441nm, (ii) 535nm, (iii) 625nm, (iv) 790nm, and (v) 1071nm. . . . .	30
2.7 Phase portrait of the torque forces calculated at $\lambda = 1071\text{nm}$ . Arrows in the $x$ and $y$ directions indicate torque that rotates the nanowire in the $\phi$ and $\theta$ directions respectively. . . . .	32
3.1 a) Signal patterns, or fractalized signals (FS) of orders $n = 1, 3$ , and 5. b) Corresponding Fourier transforms of signals on logarithm scale, or diffractal signals (DS). c) Reconstructed Fourier-transforms (RFS) from the 1% black-outlined subset, the blocked diffractal signal (BDS). d) Enlargement of a portion of the $n = 5$ diffractal, which illustrates similar patterns at different length scales. . . . .	41
3.2 The peak signal-to-noise ratio (PSNR) of RFS to FS for various fractal orders as a function of the fractional BDS size. . . . .	43

3.3 a) Light from a $\lambda = 632.8\text{-nm}$ wavelength laser is spatially filtered, expanded, and collimated and illuminates the full area of a 800x600 pixel spatial light modulator (SLM). The 4- $f$ system is composed of 2 5-cm lenses placed after the SLM. The first lens Fourier transforms the fractal signal (FS) at the focal plane. An aperture is placed off-center at the focal plane and only transmits a portion of the diffracted (BDS). The second lens reconstructs the SLM image with the light that is transmitted through the aperture. b) The Sierpinski carpet hologram of order $n=5$ , CCD image in the focal plane of the hologram after the lens, and the reconstructed image. A circle denotes the area utilized to reconstruct the image. . . . .	45
4.1 (a) Model representation: an array of plasmonic resonators (rod-shaped apertures) tilted at $\theta_s$ relative to the base of the unit meta-atom where we separate the resonators into $m$ - and $n$ -type. The interaction force on $m$ -type resonators results from the 4 nearest $n$ -type resonators and vice-versa. (b) The interaction Lorentz force that arises from Larmor radiation [Eq. 4.1] for various $\theta_s$ when resonators oscillate in the $x$ -direction, as a function of time. (c) The interaction force in the parallel ( $x$ ), and perpendicular ( $y$ ) directions when the resonators oscillate in the $x$ -direction, as a function of $\theta_s$ . . . . .	54
4.2 (a) A top-view scanning electron microscope image of the metasurface. (b) The transmission spectra associated with different linear polarization angles, where we observe the presence of bonding and anti-bonding modes. (c) Shift in the wavelengths of the bonding and anti-bonding modes as a function of polarization angle. (d) Interaction forces parallel and perpendicular to the polarization axis experienced by the resonators from Eq. 4.4 as a function of polarization angle. . . . .	60

4.3 (a) The optical rotation (OR) and change in the elliptical component as a function of input polarization at 660nm. Inset: the relationship between $E_x$ and $E_y$ OR and change in the elliptical on the polarization ellipse. (b) OR and circular dichroism (CD) calculated from a transmission (T-)matrix approach (dashed). Overlaid is the experimental measurements of OR (measured at $\psi = +30^\circ$ ), and the CD (solid). . . . .	61
4.4 Eigen-polarization modes of the system at 660nm are shown on (a), the Poincaré sphere, where solid circles represent eigen-polarization states on the near surface of the sphere and hollow circles represent states on the far surface. (b) illustrates the eigen-polarization states measured in the $x - y$ plane. . . . .	64
4.5 Spin curve for ZEP-520A. Image: <a href="https://ebeam.mff.uw.edu/ebeamweb/process/process/zep520a">https://ebeam.mff.uw.edu/ebeamweb/process/process/zep520a</a>	
4.6 The schematic diagram for (a) transmission measurements and (b) polarization measurements. . . . .	72

# Nomenclature

## Chapter 1

$\epsilon$  Material Permittivity

$\epsilon_0$  Permittivity of Free Space

$\eta$  Electron Density

$\gamma$  Decay Rate

$\langle \rangle$  Time-Average

$\omega$  Angular Frequency

$\omega_0$  Angular Frequency associated with harmonic restorative force

$\omega_c$  Cyclotron Frequency

$\omega_p$  Plasma Frequency

$\sigma$  Material Conductivity

$B$  Magnetic Field

$E$  Electric Field

$j$  Current Density

$k$  Restoring Force Constant

$M$  Magnetization

$m^*$  Reduced Mass

$q$  Electric Charge

$r$  Spatial Coordinate

$t$  Time

DC Direct Current

LHCP Left-Handed Circular-Polarization

MO Magneto Optical

RHCP Right-Handed Circular-Polarization

## Chapter 2

$\epsilon$  Dielectric Constant

$\epsilon_0$  Permittivity of Free Space

$\lambda$  Wavelength

$\rho$  Charge Density

$A$  Torque Vectors in Spherical Coordinate System

$B$  Magnetic Field

*c.c.* Complex Conjugate

$E$  Electric Field

$f$  Lorentz Force

$H_m$  Hankel Function of the  $m^th$  Kind

$J$  Current Density

$J_m$  Bessel Function of the  $m^th$  Kind

$k$  Wave-Vector

$P$  Polarization Density

$q$  Electric Charge

$T$  Torque

$v$  Velocity

UV Ultra-Violet

### Chapter 3

$\delta$  Delta Function

$\lambda$  Wavelength

$i_c$   $\sqrt{-1}$

$k$  Wave-Vector

$n$  Fractal Order

$r$  Relative Scaling Factor

$T$  Transmission Function

BDS Blocked Diffractal Signal

DS Diffractal Signal

FS Fractalized Signal

OS Original Signal

PSNR Peak Signal-to-Noise Ratio

RFS Reconstructed Fourier-Transformed Signal

ROS Reconstructed Original Signal

SLM Spatial Light Modulator

## Chapter 4

$\beta$  Ratio of Speed to the Speed of Light

$\chi$  Elliptical Component of Polarization

$\delta$  Perturbation Parameter

$\epsilon$  Material Permittivity

$\epsilon_0$  Permittivity of Free Space

$\Gamma$  Non-Locality Parameter

$\gamma$  Damping Rate

$\lambda$  Wavelength

- $\langle \rangle$  Time-Average
- $\omega$  Angular Frequency
- $\omega_0$  Angular Frequency associated with harmonic restorative force
- $\psi$  Azimuthal Component of Polarization
- $\theta_s$  Aperture Tilt
- $a$  Metasurface Periodicity
- $c$  Speed of Light
- $E$  Electric Field
- $F$  Force
- $F^{int}$  Interaction Force
- $k$  Wave-Vector
- $k_e$  Coulombs Constant
- $L$  Layer Thickness
- $M$  Mass
- $MR$  Milling Rate
- $N_0$  Free Charge Carrier Density
- $P$  Polarization Density
- $q$  Electric Charge

$R$  Lattice Distance

$r$  Spatial Coordinate

$S$  Screening Factor

$t$  Time

$T_{LCP}$  Transmission of Left Circular Polarization

$T_{RCP}$  Transmission of Right Circular Polarization

$x_h/y_h$  Homogeneous Solution in the  $x/y$  direction

CD Circular Dichroism

OA Optical Activity

OR Optical Rotation

PMMA Electron Beam Resist

SEM Scanning Electron Microscope

ZEP High Performance Electron Beam Resist

# Chapter 1

## Ultra-low-intensity magneto-optical and mechanical effects in metal nanocolloids

### 1.1 Introduction

The plasmonic resonances of noble metal nanostructures manifest in the visible spectral range and have a fundamental role in shaping the optical properties of materials [Link and El-Sayed (1999); Cortie and Ford (2007)]. At such resonances the electromagnetic fields are concentrated around sub-wavelength structures producing high local field enhancements, which has been the study of many investigations [Barnes et al. (2003); Kelly et al. (2003); Ozbay (2006)]. Since the resonances are highly dependent on the refractive index of the material, as well as the surrounding medium, methods that modify a materials refractive index *i.e.*, electro-optically [Dicken et al. (2008); Chyou et al. (2005)] or thermally [Nikolajsen et al. (2004)], are realised by a shift in the plasmonic resonance. An external magnetic field can also modulate a material's optical properties if the material exhibits magneto-

optical (MO) behaviour [Temnov et al. (2010); Gonzalez-Diaz et al. (2009); Hai-Dong et al. (2008)]. The concurrent application of a magnetic field is associated with additional phenomena such as increased Faraday rotation [Du et al. (2011)], MO enhancement of localized and propagating surface plasmons [Sepulveda et al. (2010); Torrado et al. (2010)], or introduction of new magnetic modes [Pineider et al. (2013); Tang et al. (2011); Fan et al. (2010)]. Observations of these MO phenomena, however, are generally small unless the plasmonic material is mated with a ferromagnet. Another class of MO responses involves non-oscillating, DC, magnetic modes. Such modes are achieved in non-magnetic media via the polarization-dependent inverse Faraday effect [Hertel (2006)] though this DC or low frequency MO response is claimed to be too small to observe at room temperature and at low intensities due to thermal fluctuations [Gu and Kornev (2010)] (the effect is observed with high intensity lasers,  $>370 \text{ MW/cm}^2$  [Raja et al. (1995)]). Recently, anomalously-large photo-induced magnetic responses are observed in non-ferromagnetic metal nanocolloids [Singh et al. (2012)], however the origin of the effect is unexplained. Here, we are the first to identify and analyse the threshold transition between linear and nonlinear effects, which we attribute to a mechanical response of the nanocolloid.

In this Letter we demonstrate that nonzero time-averaged vortex currents on nanostructures enable the magnetization of non-magnetic materials and that such DC MO plasmonic responses are observable with broadband light illumination intensities less than  $1 \text{ W/cm}^2$ . Moreover, we show that there exists a nonlinear MO response that is explained by the theoretical model of Hertel (2006) when applied to nanostructures [Singh et al. (2012); Brandao and Cavalcanti (2013); Bliokh et al. (2011)]. This coupling between incident and scattered fields yields nonzero time-averaged azimuthal vortex power flows that differ distinctly in character from the polar-coordinate whirlpool flows investigated in other work [Boriskina and Reinhard (2012); Bashevoy et al. (2005)]. We quantify the vortex

power flows associated with azimuthal currents that result in the formation of DC magnetic dipoles. More importantly, we demonstrate that such dipoles are non-negligible and external magnetic fields influence the nanocolloidal optical properties. Experimentally, the response is observed in the extinction spectra of aqueous 80-nm gold nanospheres when illuminated with circularly-polarized light and DC magnetic fields, in which changes occur on minute time-scales. We attribute the retarded response to magnetic-dipole interactions and the mechanical movement and settling of asymmetrical nanoparticles and nanoclusters. The formation of realizable DC magnetic dipoles and the associated mechanical effects are verified in numerical simulations.

We demonstrate that both linear and nonlinear plasmon phenomena lead to MO responses. Linear characteristics associated with volume charge densities are distinct from nonlinear characteristics associated with surface charges, which dominate the MO response above low-threshold magnetic fields. The linear dynamics are described by a conventional Hall-effect Drude model [Mulvaney (1996)], which provides a magnetic-field dependent refractive index via the Lorentz force. In contrast, the nonlinear dynamics are identified with the inverse Faraday effect, which yields a nonlinear current density proportional to the incident electric field intensity [Hertel (2006)]. It is fundamental to our analysis that while there is no net current i.e.,  $\langle \vec{j}_x \rangle = \langle \vec{j}_y \rangle = \langle \vec{j}_z \rangle = 0$ , non-zero time-averaged current loops exist such that  $\langle \vec{j}_\phi \rangle \neq 0$ . This existence of nonzero  $\langle \vec{j}_\phi \rangle$  forms the basis of the nonlinear DC MO response.

## 1.2 Linear Dynamics

### 1.2.1 Addition of Magnetic Fields to Equations of Motion

The linear dynamics of the volume charge density, within the quasi-static limit [Maier (2007)], are governed by the equations of motion with the Lorentz force:  $m^* \frac{d^2 \vec{r}}{dt^2} + m^* \gamma \frac{d\vec{r}}{dt} = q\vec{E} + q(\frac{d\vec{r}}{dt} \times \vec{B})_r - k\vec{r}$ , where  $\vec{r}$  denotes the spatial coordinate,  $m^*$  is the effective mass of the electron,  $\gamma$  is the decay rate,  $q$  is the charge of an electron, and  $k$  is the force constant associated with the restoring force. The electric field propagates in the  $\hat{z}$  direction with time-harmonic circular-polarization of angular frequency  $\omega$  and amplitude  $E_0$ ,  $\vec{E}_\pm = E_0 e^{-i\omega t} (\hat{x} \pm i\hat{y})/\sqrt{2}$ , where  $+(-)i\hat{y}$  represents a right(left)-handed circular-polarized wave or RHCP(LHCP). When an externally-applied DC magnetic field is aligned with the direction of the electric-field propagation,  $\vec{B} = B_0 \hat{z}$ , the equations of motion yield a dielectric function in the form of a gyrotropic tensor:  $\epsilon = 1 + \omega_p^2 \begin{pmatrix} \alpha & -\beta & 0 \\ \beta & \alpha & 0 \\ 0 & 0 & \zeta \end{pmatrix}$ , in which  $\alpha = \frac{\omega_0^2 - \omega^2 - i\gamma\omega}{(\omega_0^2 - \omega^2 - i\gamma\omega)^2 + (\omega\omega_c)^2}$ ,  $\beta = \frac{i\omega\omega_c}{(\omega_0^2 - \omega^2 - i\gamma\omega)^2 + (\omega\omega_c)^2}$ , and  $\zeta = \frac{1}{\omega_0^2 - \omega^2 - i\gamma\omega}$ , where  $\omega_c = qB_0/m^*$  is the cyclotron frequency,  $\omega_p$  is the plasma frequency such that  $\omega_p^2 = \eta q^2/m^* \epsilon_0$ ,  $\omega_0$  is the frequency associated with a harmonic restorative force, and  $\eta$  is the electron density. The Lorentz force is largest when the DC magnetic field is parallel to the propagation of light [Sepulveda et al. (2010)].

As can be seen in Fig. 1.1, around the plasmon resonance (540 nm) there are significant shifts in the real and imaginary parts of the refractive index. This MO model explains the response from small magnetic-field perturbations, however is insufficient to explain the changes in optical properties at higher applied magnetic fields [Singh et al. (2012)]. The MO response of noble metals (calculated with linear dynamics) is significantly smaller compared to that which occurs with ferromagnets in part because the difference between the cyclotron and plasma frequencies is orders of magnitude apart [Schnatterly (1969)].

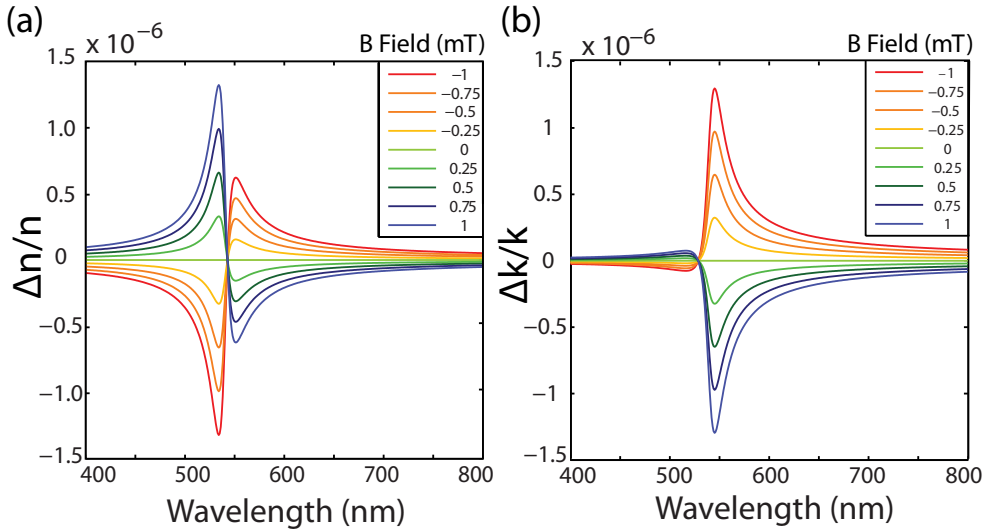


Figure 1.1: Relative MO shift of bulk gold when external fields are varied. (a) Real and (b) imaginary parts of the refractive index as a function of wavelength under illumination of  $1 \text{ W/cm}^2$  RHCP when magnetic fields are varied.

Moreover, the MO response depends on other factors such as the exchange interaction, specific band structure and spin-orbit coupling that allow ferromagnetic materials to have a greater MO response than noble metals [Armelles et al. (2013)].

## 1.3 Nonlinear Dynamics

### 1.3.1 Nonlinear Current Density

In departure from prior investigations of MO effects on nanostructures, we use the analytical expression derived from the continuity equation [Hertel (2006)] to describe a time-averaged solenoidal magnetization current density:

$$\langle \vec{j}_m \rangle = \frac{i}{4q\langle \eta \rangle \omega} \nabla \times (\sigma_0^* \vec{E}^* \times \sigma_0 \vec{E}), \quad (1.1)$$

where  $\langle \eta \rangle$  is the time-averaged electron density,  $\sigma_0$  is the specific conductivity of gold,

and  $\vec{E}$  is the total electric field at the surface. As seen in Eq.(1.1)  $\langle \vec{j}_m \rangle$  is polarization-dependent in its direction and magnitude. For a circularly-polarized  $\vec{E}$  the term  $\vec{E}_\pm \times \vec{E}_\pm^*$  becomes  $\pm i|\vec{E}_0|^2\hat{z}$  and for a linearly-polarized field this term is zero. Note that  $\langle \vec{j}_m \rangle$  scales inversely with  $\langle \eta \rangle$ , which may explain MO effects in non-metallic nanostructures [Kuznetsov et al. (2012)] and also scales with the intensity, in contrast to linear currents which scale with the electric field ( $\vec{j} = \sigma_0 \vec{E}$ ).

### 1.3.2 Nonlinear Magnetization

In our investigation of nanospheres, the time-averaged nonlinear current density is significant only in the azimuthal direction,  $\hat{\phi}$ ,  $\langle \vec{j}_{m,r} \rangle = 0$ ,  $\langle \vec{j}_{m,\theta} \rangle \ll \langle \vec{j}_{m,\phi} \rangle$ . Although linear time-harmonic azimuthal currents exist, the current direction reverses every 1/2 cycle and time-average to zero. Since the nonlinear surface currents produce an anisotropic field-dependent perturbation to the specific conductivity, it is reasonable to employ a formalism similar to that used for the nonlinear polarization with the nonlinear current density as  $\vec{j}_p(\vec{E}) = \vec{j}_p^{(1)}(\vec{E}) + \vec{j}_p^{(2)}(\vec{E}, \vec{E}) + \dots = \sigma_{p,r}^{(1)} E_q + \sigma_{p,r,s}^{(2)} E_r E_s + \dots$ , where  $\sigma_{p,r}^{(1)}$  is the specific conductivity in isotropic media. Using Eq. (1.1) and Levi-Cevita notation  $\sigma_{p,r,s}^{(2)}$  can be written as a third-rank tensor in the form:

$$\sigma_{p,r,s}^{(2)} = \frac{i|\sigma_0|^2}{4q\langle \eta \rangle \omega} \frac{\epsilon_{p,r,s} \hat{\partial}_r \epsilon_{s,t,u} E_t^* E_u}{E_r E_s}. \quad (1.2)$$

A relation for the induced magnetization can also be obtained using  $\vec{j}_m = \nabla \times \vec{M}$ , such that:

$$\vec{M}_p = \frac{i|\sigma_0|^2}{4q\langle \eta \rangle \omega} \epsilon_{p,r,s} E_r^* E_s \quad (1.3)$$

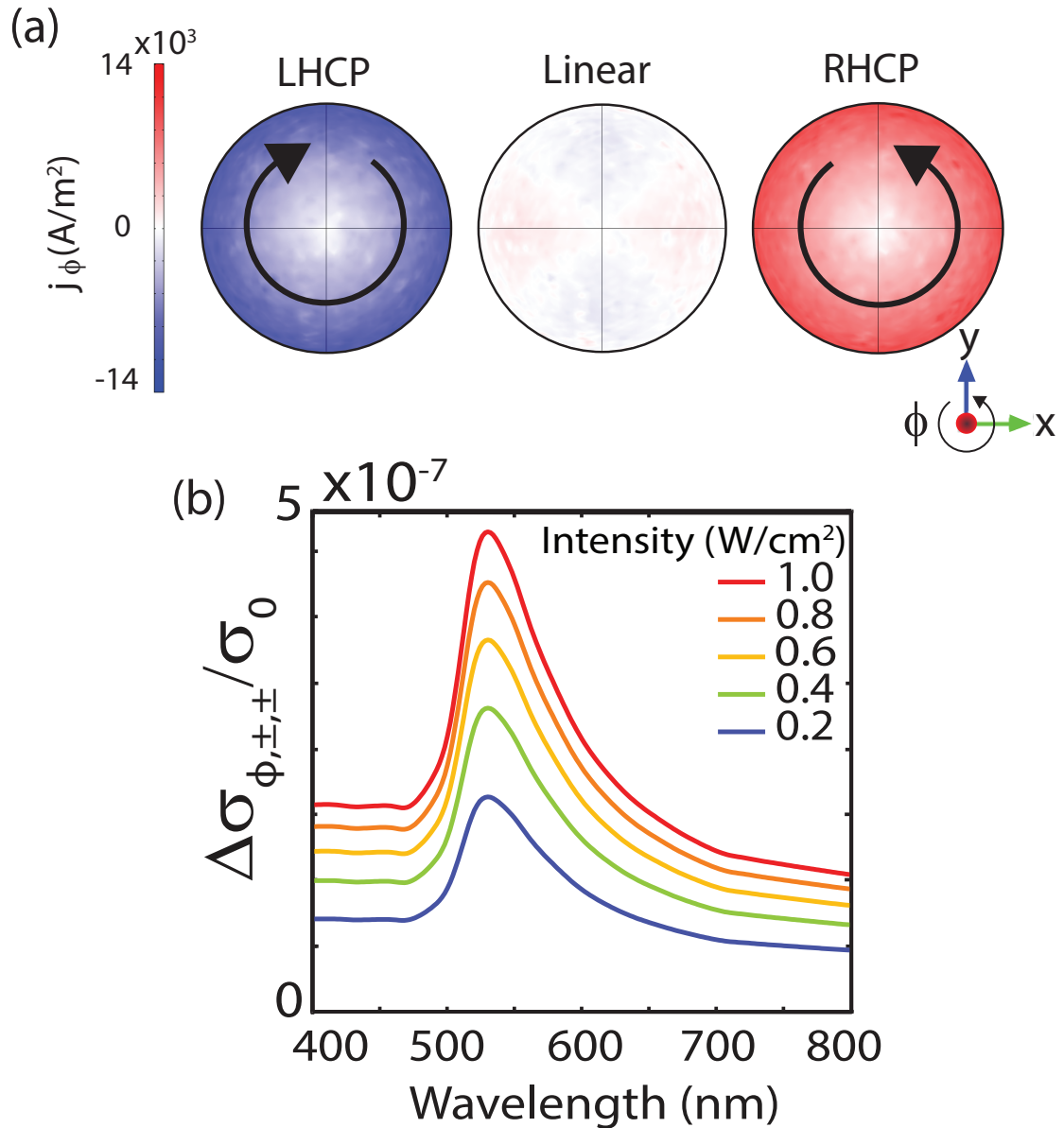


Figure 1.2: (a) Surface plots of the nonlinear current density of an aqueous 80-nm gold nanosphere when illuminated by LHCP, linearly-polarized and RHCP light in the  $\hat{z}$  direction at the plasmon resonance, 540 nm, at 1 W/cm<sup>2</sup>. (b) Volume-averaged relative change in azimuthal component of the conductivity as a function of wavelength when illumination intensity is varied for RHCP or LHCP.

## 1.4 Numerical Predictions

### 1.4.1 Finite-element simulation Results

Numerical, finite-element simulations illustrate the strong polarization dependence of the nonlinear current density that the theoretical analyses predict. As seen in Fig. 1.2(a) the induced nonlinear current density,  $\langle \vec{j}_{m,\phi} \rangle$ , is calculated for an aqueous 80-nm gold nanosphere illuminated in the  $\hat{z}$  direction with different polarizations. To simplify the notation of the nonlinear conductivity response we use only the first subscript of  $\sigma^{(2)}$  which denotes the direction of the anisotropic change. It can be shown that  $\sigma^{(2)}$  is nonzero only for curvilinear coordinates such as  $\phi$  or  $\theta$  in spherical coordinates. The numerical calculations illustrate that  $\sigma_{\phi}^{(2)}$  is negligible for incident linear polarization, and RHCP and LHCP yield the greatest  $\sigma_{\phi}^{(2)}$  with equal direction and magnitude; as illustrated in Fig. 1.2(b), as the light intensity increases, the conductivity of the nanoparticle also increases uniformly across wavelengths for both RHCP and LHCP. Since both the azimuthal currents ( $\propto \nabla \times \vec{E}^* \times \vec{E}$ ) and the electric-field components ( $\vec{E}_{\phi}$ ) reverse direction with polarization handedness, by symmetry, the relative changes in the conductivity tensor are identical for both RHCP and LHCP.

## 1.5 Experimental Observation

### 1.5.1 Observation of Transition from Linear to Nonlinear Dynamics

Experimental data of relative MO changes in transmission spectra are illustrated in Fig. 1.3, alongside analytical results. The experiments were performed with samples of 0.05 mg/mL 80-nm poly-vinyl pyrrolidone(PVP)-capped gold nanoparticles dispersed in aqueous solution

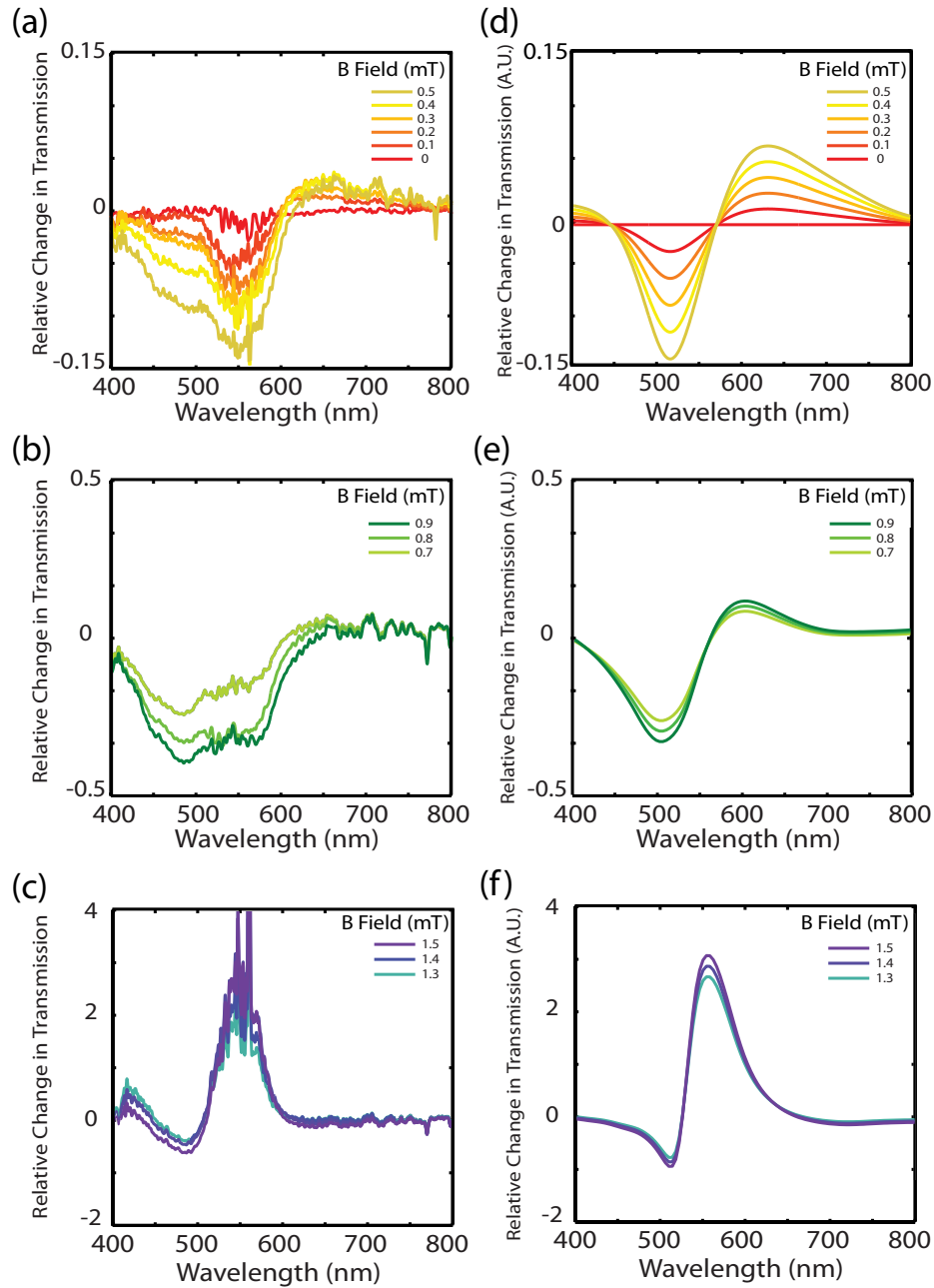


Figure 1.3: Normalized MO changes in transmission for aqueous gold nanocolloid at (a) low magnetic fields (b) intermediate magnetic fields and (c) higher magnetic fields. Theoretical MO change in transmission of aqueous 80-nm gold nanospheres in the (d) linear and (f) nonlinear analyses. Theoretical MO changes that combine the linear and nonlinear analyses are shown in (e) for intermediate magnetic fields. In all plots the illumination is 1 W/cm<sup>2</sup> and RCP.

( $2.5 \times 10^{-6}$  fill factor). A solar simulator, polymer thin-film linear polarizer, and 400-800 nm achromatic quarter-wave plate produce RHCP white light, and a Helmholtz coil generates a uniform magnetic field in the direction of light propagation around the sample. A CCD spectrometer that captures the extinction spectra is placed behind a 0.5-cm optical path length cuvette containing samples.

The dominant response is dependent on the illuminating light polarization at low magnetic fields and is polarization-independent in the presence of higher magnetic fields; a threshold behaviour exists. Experimentally, we associate a magnetic field of 0.9 mT as the bound between the linear (polarization-dependent) and nonlinear (polarization-independent) dynamics. The experimental data [Fig. 1.3(a-c)] shows relative transmission data for RHCP and positive magnetic fields. Below the threshold, differences between the handedness of the polarizations are observed; the MO response is approximately equal and opposite in magnitude. Above, the transmission is similar for both RHCP and LHCP.

The experimental data agrees with analytical theory when the changes of the refractive index [Fig. 1.1] and conductivity [Fig. 1.2(b)] are incorporated to Mie theory [Mie (1908)] and the corresponding relative changes in extinction spectra are computed. These calculated linear and nonlinear MO responses are shown separately in Fig. 1.3(d) and Fig. 1.3(f) respectively, and both linear and nonlinear MO responses are incorporated to analyse the total response at intermediate fields near the threshold [Fig. 1.3(e)]. The relative change in the nonlinear MO response has been scaled to reflect the experimental behaviour. We model the nonlinear response as a function of the external magnetic field, which tunes the strength of the coupling that causes the MO response. The threshold behaviour observed experimentally is expected to occur when the theoretical linear and nonlinear effects are comparable. Moreover, our theoretical model provides excellent quantitative agreement; in our analysis of a single nanosphere the changes in the refractive index and conductivity

via the linear and nonlinear responses are of similar magnitude with  $1\text{-W/cm}^2$  illumination intensities and  $1\text{-mT}$  magnetic fields. The transition between the polarization-dependent linear response and the polarization-independent nonlinear response occurs when either the magnetic field strength or the intensity of light is varied.

## 1.6 Discussion

### 1.6.1 Magnetization Magnitudes

Our understanding of the light scattering at nanostructures is crucial for understanding both linear and nonlinear MO effects. In the limit of thin structures, the scattered component of the electric field is largest in the longitudinal direction,  $E_z$ , and carries phase singularities that change with circular polarization handedness [Vuong et al. (2010); Hasman et al. (2005)]. The locations of the phase singularities, as well as the topological charges themselves vary with nanostructure geometry and are associated with the loops in the *linear* current density. *Nonlinear* current loops are also produced by scattering events that induce surface charge densities, which couple with the incident fields [Eq. 1.1]. It is these nonlinear nonzero time-averaged current loops that lead to the material magnetization  $M_z$ . The amplitude and phase of  $E_z$  and corresponding  $M_z$  for an 80-nm gold nanosphere illuminated with RHCP are shown in Fig. 1.4. Although the non-magnetic nanoparticle magnetizations are small compared to that of a ferromagnet ( $10^5$  times smaller) due to masses on the order  $10^{-18}\text{ kg}$ , the subsequent mechanical motion becomes significant.

### 1.6.2 Time-Dependent Response

The delayed optical response to an applied magnetic field is likely the result of the settling motion of non-spherical nanoparticles and nanoclusters. Aggregates often form as a result

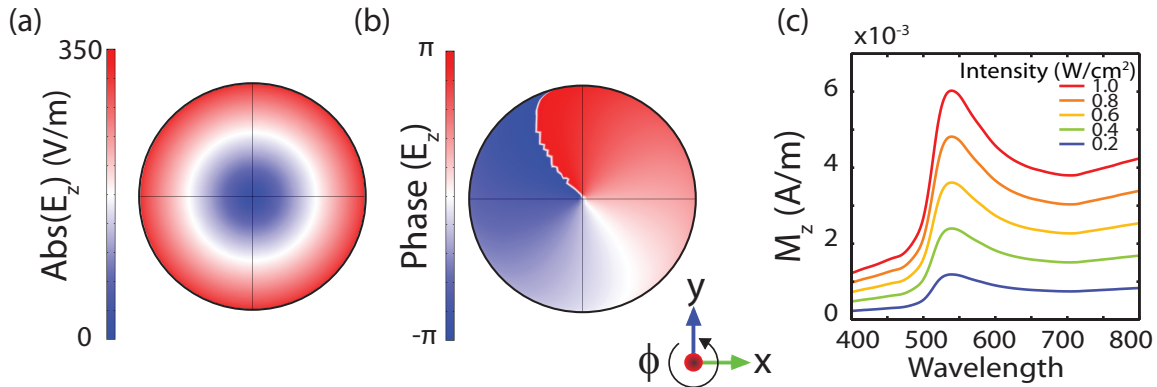


Figure 1.4: Numerically calculated (a) amplitude and (b) phase of the longitudinal component of the electric field,  $E_z$ , with 540-nm  $1 \text{ W}/\text{cm}^2$  RHCP illumination intensity. (c) Volume-averaged magnetization as a function of wavelength when illumination intensities are varied. All plots are for an aqueous 80-nm gold nanoparticle.

of random Brownian motion and magnetic-dipole interactions, so they are considered in our analysis. We also acknowledge that the nanoparticles employed in the experiments are not perfect spheres and exhibit irregularities from the fabrication process; such variations from spherical geometry cause magnetization differences that depend on the nanoparticle orientation with respect to the electric field.

Changes in extinction spectra reflect the magnetization associated with the nanoparticle and nanoclusters reorientation. Structural anisotropy and orientation affect the magnetization of the nanoparticle, which we illustrate with dimer nanoclusters and ellipsoids of different aspect ratios. As can be seen in Fig. 1.5(a) there is a reduction in the magnetization by almost 50% as a dimer nanocluster rotates from minimal to maximal incident surface area with respect to electric field. The relative change in the magnetization is shown in Fig. 1.5(b) as a function of aspect ratio when ellipsoidal nanoparticles of equal volume are rotated from minimal to maximal incident surface area. Ellipsoids with aspect ratio 1 (spheres), exhibit no difference as they are rotated, and greater differences are observed when the aspect ratio increases. To guide the eye, a trendline that reflects the Biot-Savart law is provided in Fig. 1.5(b). Deviations from the trendline are attributed to changes

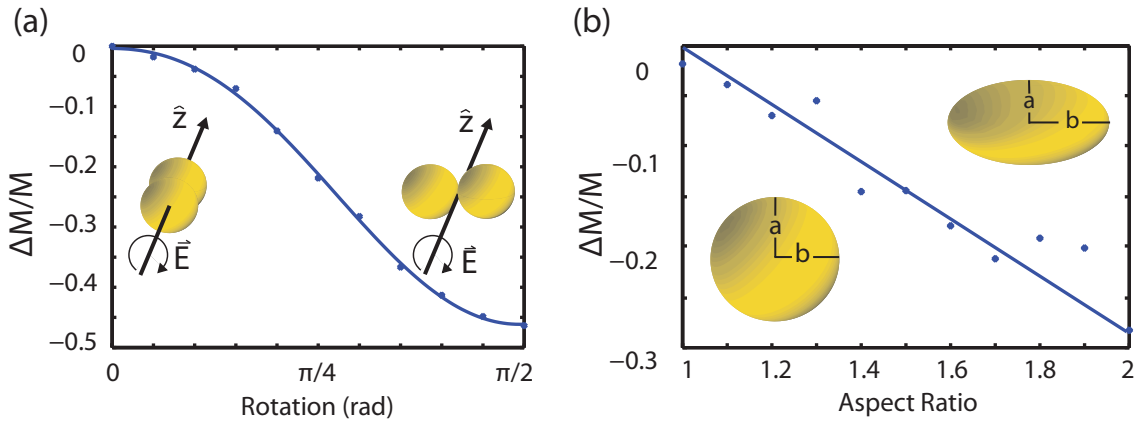


Figure 1.5: Numerically calculated relative change in magnetization (a) of a 80-nm gold dimer nanocluster as a function of angle of rotation, and (b) ellipsoidal gold nanoparticle rotated from minimal to maximal surface area as a function of aspect ratio, illuminated with 540-nm 1 W/cm<sup>2</sup> RHCP.

in the plasmonic eigenfrequency. Regardless, anisotropy in the nanoparticle shape leads to MO magnetization that varies with the orientation, a concept in agreement with prior work Jain et al. (2006); Funston et al. (2009).

There exists a nanoparticle/nanocluster orientation with respect to the external magnetic field that maximises  $\langle \vec{j}_m \rangle$ . The system is expected to stabilize in an orientation that maximises the nanoparticle magnetization. The nanocolloid magnetization is largest at the plasmon resonance when the local electric field and scattering is maximised.

Yet, scattering dynamics present a complex dynamical system that is not fully understood in the context of MO responses. Autocorrelation data reveals significant pulse broadening through gold nanocolloid solution that scales with the square of the sample thickness that suggests a strong scattering [Drake and Genack (1989)] despite low fill factors ( $2.5 \times 10^{-6}$ ). Another possibility for the larger-than-expected results is diffractive coupling between nanoparticles that can exhibit strong long-range interaction [Barnes and Aguie (2009)] that lead to near-field enhancements, which are anticipated to increase in a 3-D matrix. The material properties of the matrix also influence the MO response. For instance,

the presence of any ions or charged particles, common in solvents such as water, modifies the electrodynamics of the system, which subsequently influences the MO response of the system.

## 1.7 Conclusion

In conclusion, we demonstrate that MO responses are observed in non-magnetic nanocolloids at ultra-low illumination intensities and magnetic fields. Metal nanocolloids are magnetized and the optical properties are shifted when excited by coincident elliptically-polarized electric fields and DC magnetic fields. Experimentally-observed extinction spectra are in good agreement with predictions of linear and nonlinear MO effects and we provide new considerations for novel mechanical effects that were previously considered unattainable. Here we demonstrate a theoretical model that successfully explains the transition between linear and nonlinear MO plasmon dynamics of metal nanoparticles. This research provides the theoretical framework to study MO responses in non-magnetic nanostructures. In particular, new methods to identify, optically self-assemble and magnetically torque large quantities of disperse, non-spherical nanoparticles with broadband light sources are realised.

## 1.8 Experimental Difficulties and Future Work

The experimental procedure to study the transmission properties were quite difficult. One recurrent issue that occurred was a time dependence in the transmission properties before any magnetic field was applied. This issue was attributed to thermal stabilization of the system and was overcome by waiting for the transmission properties to thermally stabilize before turning on the magnetic field and taking any measurements.

Care was also taken in the amount of light intensity, as it was found that if the light

intensity was too great, there would be aggregation and settling of the nanoparticles at the bottom of the substrate. Aggregation may affect the results by shifting the plasmonic resonance of the nanoparticles due to the increase in size, which may confound the results. Settling of the nanoparticles is also undesirable since there is a reduction of the nanoparticle density interacting with the electric and magnetic fields that way decrease the MO effect and increase the transmission through the sample, confounding the results.

Future work on this subject may involve a deeper investigation of the threshold between the linear and nonlinear components that cause the respective transmission properties.

# Chapter 2

## Plasmon-induced Lorentz forces of nanowire chiral hybrid modes

### 2.1 Introduction

While light is massless, it imparts momenta that are significant, which: confine ion beams [Petrich et al. (1993)]; propel solar sails [Janhunen and Sandroos (2007)]; rotate and twist objects [Beth (1936); Paterson et al. (2001); Tsai et al. (2014)]; levitate, trap, and move matter [Ashkin (1997); Nieminen et al. (2007); Novotny et al. (1997)]; cool atoms [Weiner et al. (1999)]; and alter the crystallization of solids [Chowdhury et al. (1985)]. Our knowledge of light's momentum transfer is intrinsic to the design of facilities for low-temperature and high-energy physics, cell and molecular biology, and advanced materials research [Ashkin (1997)], and is relevant to an expansive development of optomechanical devices for sensors and electronics technologies [Hugel et al. (2002); Kippenberg and Vahala (2007); Van Thourhout and Roels (2010)]. Currently, the laser trapping of uncharged dielectric matter is commonplace [Ashkin (1997)]; however, the optically-induced mechanics of conducting or plasmonic nanoparticles have been shown to be, at the very least, more

complex [Dienerowitz et al. (2008); Saija et al. (2009); Shvedov et al. (2010); Yan et al. (2012a,b, 2013a); Yan and Scherer (2013); Yan et al. (2013b)]. One challenge stems from the numerous channels through which energy is transferred: particles also move in the presence of electric fields, magnetic fields, and thermal gradients [Velev and Bhatt (2006); Keshoju et al. (2007); Edwards et al. (2006)], which are directly and indirectly produced by plasmons. Understanding these dynamic, momentum-conserving mechanisms involves, in part, understanding the interactions among these fields.

Theoretical considerations of the gradient-intensity trapping forces, radiation pressure forces, and induced-electric-dipole interactions [Ashkin (1997)] are insufficient for predicting the optomechanical behavior of plasmonic nanoparticles. It is increasingly apparent that the excitation of plasmons play a critical role in the optically-induced movement of nonspherical nanoparticles [Yan et al. (2013a)]. For example, a model of the induced electric dipole with an electric field only predicts that silver nanorods will align parallel to the direction of the illuminating linear polarization of light [Tong et al. (2010)], and that nanowires rotate continuously in the presence of circularly-polarized light or optical vortices via the transfer of spin or orbital angular momentum, respectively [Yan and Scherer (2013); Lehmuskerö et al. (2013, 2014)]. However, this theoretical model that considers the nanoparticle polarizability alone cannot discriminate between the different mechanical behaviors associated with different nanorod-ends and particle aspect ratios [Tong et al. (2010)]. Nanoparticle geometry often dictates local surface plasmon modes [Knight et al. (2007)]; further insight into the physical phenomena that underlie the optomechanical behavior of non-spherical plasmonic particles is necessary.

Here we focus our analysis on the Lorentz forces strictly attributed to surface plasmons on metal nanowires, which are of wide technological interest [Knight et al. (2007); Lal et al. (2007); Maier and Atwater (2005)], and potentially relevant to other plasmonic nanostruc-

tures such as carbon nanotubes, where similar chiral plasmonic behavior is tunable from the UV to THz [Slepyan et al. (2006)]. The first successful trapping of a nanowire in a 3D optical trap identified an important role of plasmons. Yan, *et al.*, demonstrate that gold nanowires—but significantly, *not* silver nanowires—are confined by a Gaussian-beam optical trap [Yan et al. (2013a)]. Yan proposes that the macroscopic perspective of optical trapping is insufficient and should be replaced with a plasmonic model [Yan et al. (2012a)] and identifies asymmetric modes with trapping instabilities; nevertheless, to the best of our knowledge, a simple model that connects the dynamic instability of nanowires with its plasmonic behavior has not yet been advanced.

We numerically investigate the plasmonically-induced Lorentz forces that are produced on gold nanowires by the illumination of linearly-polarized electromagnetic plane waves. The plasmonically-induced forces are significant in chiral geometries and when chiral hybrid plasmonic modes [Zhang et al. (2011)] are present. We are the first to identify the electromagnetic torque and compression on the nanowires associated with the surface currents and asymmetric time-averaged fields. Our results identify significant mechanical forces produced by surface plasmons in chiral hybrid modes that are currently neglected. In fact, plasmonically-induced Lorentz forces are expected to critically prevent the stable optical trapping of conducting nanowires, particularly when longer trapping-laser wavelengths *between* strong absorption resonances are employed. Our approach highlights a critical dependence of nanoparticle shape [Knight et al. (2007); Tong et al. (2010)] and plasmon relaxation [Yan et al. (2013a)] on the optically-induced forces, and considerations are relevant to future microfluidic applications.

This chapter is organized as follows. In Sec. 2.2 we describe the chiral geometry of our system, outline the numerical computations associated with Lorentz forces, and illustrate the asymmetric surface plasmon modes. We evaluate the electric dipole and plasmonic

Lorentz forces of nanowires that are aligned in the transverse plane, with outcomes that agree with and clarify prior experimental results. In Sec. 2.3, we describe the axial and translation forces associated with surface plasmons, these forces are generally stronger than those associated with electric dipoles. In Sec. 2.4 we provide an analysis of the torque forces that arise from the 3D scattering. In Sec. 2.5 we conclude. In our studies, we ignore the nonlinear responses that arise due to heat [Shvedov et al. (2010)], steam [Saija et al. (2009); Fang et al. (2013)], the electrochemical response of solvent [Arcenegui et al. (2013)], and nonlinear magneto-optical effects [Singh et al. (2012); Moocarme et al. (2014)], although these effects are not negligible, particularly at high illumination intensities. We ignore surface effects that may arise in the interaction between nanoparticles due to coatings or interfaces, however our work is highly relevant to our understanding of such interactions with plasmonic materials [Bonin et al. (2002)]. The mechanical translation, compression, and torque forces associated with the plasmonic surface currents are significant and interfere with the optical trapping of elongated nanoparticles. Our results indicate that there exists a frequency cut-off at which the chiral plasmon excitation is minimized; avoiding chiral plasmon excitation will provide greater trapping stability.

## 2.2 Setup and simulations of 2D dynamics

### 2.2.1 Calculation of Electromagnetic Fields

In our numerical investigation (COMSOL v4.3a, RF module,  $\sim$ 2 million degrees of freedom), a linearly-polarized plane wave illuminates a gold nanowire immersed in deionized water, whose orientation is determined by  $\theta$  and  $\phi$ , as illustrated in Fig. 2.1(a). The nanowire dimensions are fixed with 75-nm diameter, and 950-nm length. The nanowire terminations are hemispherical, thus the nanowire measures 1025-nm end-to-end. The electromagnetic

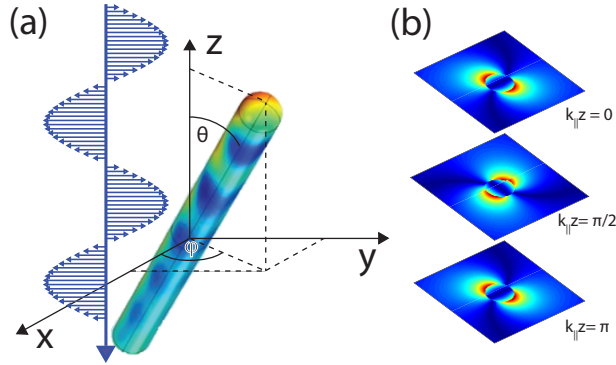


Figure 2.1: (a) System geometry: a gold nanowire (75-nm diameter, rounded-cap, 1025-nm length) is aligned about spherical coordinates  $\theta$  and  $\phi$ , and a  $y$ -polarized electromagnetic wave ( $1 \text{ W/cm}^2$ ) travels in the  $-z$  direction. (b) The electric field profile surrounding a nanowire resulting from superposed angular momentum modes  $m = 0, \pm 1$  with propagation lengths  $k_{\parallel}z = 0, \pi/2$ , and  $\pi$ .

waves are polarized in the  $y$ -direction and propagate in the negative- $z$  direction.

In particular, we are interested in the dynamics that occur when the wire is tilted towards the incoming plane wave, i.e.,  $\theta \neq 90^\circ$ . Such arrangements produce chiral plasmons, which are superpositions of the transverse and longitudinal modes. The signature for such modes is a time-averaged electric-field amplitude on the surface of the nanowire that varies azimuthally and over the length of the sample, a result of the superposition of two or more plasmon modes with varying azimuthal angular momentum number  $m$ , which are excited simultaneously by the incident fields. The phase difference associated with the different angular momentum numbers  $m$  determines the asymmetric nanowire intensity patterns [Zhang et al. (2011)]. In cylindrical coordinates the electromagnetic fields take the form [Chang et al. (2007)]:

$$\begin{aligned}
E_j(r) = \frac{1}{k_j} & \sum_m \left\{ \left[ \frac{m}{s} a_{j,m} F_{j,m} + \frac{k_m^{(\parallel)} k_{j,m}^{(\perp)}}{k_j} b_{j,m} F'_{j,m} \right] i\hat{s} \right. \\
& - \left[ k_{j,m}^{(\perp)} a_{j,m} F'_{j,m} + \frac{mk_m^{(\parallel)}}{k_j s} b_{j,m} F_{j,m} \right] \hat{\phi} \\
& \left. + \frac{[k_{j,m}^{(\perp)}]^2}{k_j} b_{j,m} F_{j,m} \hat{z} \right\} e^{ik_m^{(\parallel)} z + im\phi}
\end{aligned} \tag{2.1}$$

$$\begin{aligned}
H_j(r) = \frac{i}{\omega\mu_0} & \sum_m \left\{ \left[ \frac{k_m^{(\parallel)} k_{j,m}^{(\perp)}}{k_j} a_{j,m} F'_{j,m} + \frac{m}{s} b_{j,m} F_{j,m} \right] i\hat{s} \right. \\
& - \left[ \frac{mk_m^{(\parallel)}}{k_j s} a_{j,m} F_{j,m} + k_{j,m}^{(\perp)} F'_{j,m} \right] \hat{\phi} \\
& \left. + \frac{[k_{j,m}^{(\perp)}]^2}{k_j} a_{j,m} F_{j,m} \hat{z} \right\} e^{ik_m^{(\parallel)} z + im\phi}
\end{aligned} \tag{2.2}$$

where  $(s, \phi, z)$  are the cylindrical coordinates, the wave vectors are related by  $\epsilon_j k_0^2 = [k_{j,m}^{(\perp)}]^2 + [k_m^{(\parallel)}]^2$  where  $\epsilon_j$  is the dielectric constant in region  $j$  and  $k_0$  is the wave vector in vacuum.  $j = 1$  outside the cylinder where  $F_{1,m} = H_m(k_{1,m}^{(\perp)} s)$ , the Hankel function of  $m^{th}$  kind.  $j = 2$  inside the cylinder where  $F_{2,m} = J_m(k_{2,m}^{(\perp)} s)$ , the Bessel function of  $m^{th}$  kind, and primes denote derivatives with respect to the argument.  $a_{j,m}$  and  $b_{j,m}$  are constants determined by boundary conditions. The modes excited in our system are the  $m = 0$ , TM<sub>0</sub> mode and two degenerate first order  $m = \pm 1$  modes, HE <sub>$\pm 1$</sub> . Specifically, chiral-hybrid modes occur when all three of the lower order modes are simultaneously excited and there is a phase difference between the HE<sub>1</sub> and HE<sub>-1</sub> modes. A superposition of the three lowest order modes,  $|m| \leq 1$  are shown in Fig. 2.1(b) at different cross-sections of the nanowire corresponding to  $k_1^{(\parallel)} z = 0, \pi/2$ , and  $\pi$ . In general, the patterns in the electromagnetic fields produced off-resonance correspond to a periodic, asymmetric pattern on the wire

that neither carries mirror symmetry along the length nor across the width of the wire. We anticipate that it is this asymmetry, which arises from the chiral illumination geometry, that produces a net translation and torques via Lorentz forces.

### 2.2.2 Calculation of Lorentz Force

The well-known Lorentz law,  $\mathbf{f}_{Lorentz} = q(\mathbf{E} + [\mathbf{v} \times \mathbf{B}])$ , governs the force on a charge  $q$  with velocity  $\mathbf{v}$  in the presence of electric and magnetic fields,  $\mathbf{E}$  and  $\mathbf{B}$ . While it is true that displacement of a charged particle can be resolved to physical quantities such as dielectric function and plasma frequency the focus of our investigation is related the macroscopic movement of the nanowires. In our study, we investigate the Lorentz forces acting on a free electron gas which is bound to the surface of the nanowire. Such forces arise from time-harmonic electric and magnetic fields and subsequently, the effects of time-harmonic charge densities and surface currents. We rewrite in time-averaged macroscopic force density:

$$\langle \mathbf{f}_{Lorentz} \rangle = \rho[\mathbf{E}^* + (\mathbf{v} \times \mathbf{B}^*)] + c.c. \quad (2.3)$$

$$= \epsilon_0(\nabla \cdot \mathbf{E})\mathbf{E}^* + \mathbf{J} \times \mathbf{B}^* + c.c. \quad (2.4)$$

$$= \mathbf{f}_E + \mathbf{f}_M \quad (2.5)$$

where  $\rho$  is the charge density,  $\epsilon_0$  is the permittivity constant, and *c.c.* refers to the complex conjugate.  $\mathbf{J}$  is the current density and can be determined from the electric field [Eq. 2.1] via the relation  $\mathbf{J} = \sigma\mathbf{E}$ . The volume-integrated terms of Eq. 2.4 yield separate effects. The induced electric-dipole force,  $\mathbf{f}_E$ , depends on the polarizability of the material, which is also shape-dependent [Liaw et al. (2014)] while the Lorentz force associated with surface currents,  $\mathbf{f}_M$ , is the focus of this investigation.

### 2.2.3 Calculation of Torque Forces

We also study the net torque forces associated with Eq. 2.4 with respect to the origin and geometric nanowire center. The torque associated with  $\mathbf{f}_M$  is numerically computed directly:

$$\mathbf{T}_M = \int_V \mathbf{r} \times \mathbf{f}_M dV, \quad (2.6)$$

whereas the time-averaged torque associated with the induced electric dipole is

$$\mathbf{T}_E = \int_V \mathbf{r} \times \mathbf{f}_E dV = \int_V \mathbf{P} \times \mathbf{E}^* dV + c.c., \quad (2.7)$$

where  $\mathbf{P}$  is the polarization and  $\mathbf{r}$  is the radial coordinate vector in spherical coordinates. Eqs 2.4, 2.6, 2.7, are calculated over the volume of the nanowire in the numerical simulations.

We introduce our study with a presentation of the well-studied plasmon-induced forces when the nanowire is normal to the incident electromagnetic wave, which represents the experiments performed when wires are pressed via radiation pressure along a normal surface such as a microscope slide in a 2-D trap [Tong et al. (2010)]. In this configuration, chiral plasmons are not produced; nevertheless, surface plasmons produce significant Lorentz forces. Figure 2.2(a) shows the absorption cross-section for a nanowire in this transverse configuration. When the nanowire is aligned with the polarization of incident radiation ( $\theta = 90^\circ, \phi = 90^\circ$ ), the longitudinal modes ( $\lambda = 625\text{nm}, 790\text{nm}$ ) are present; when it is aligned perpendicular ( $\theta = 90^\circ, \phi = 0^\circ$ ), only the transverse mode ( $\lambda = 510\text{nm}$ ) is present.

The longitudinal components of  $\mathbf{f}_M$  are significant (on the order of pN/(MW/cm<sup>2</sup>)) in the direction of light propagation ( $-z$ ) when the transverse and longitudinal plasmonic resonances are present [Fig. 2.2(c)]. Large longitudinal forces arise between wavelengths  $\lambda = 900\text{-}1100\text{nm}$  in where there is large scattering and low absorption [Fig. 2.2(a), (b)].

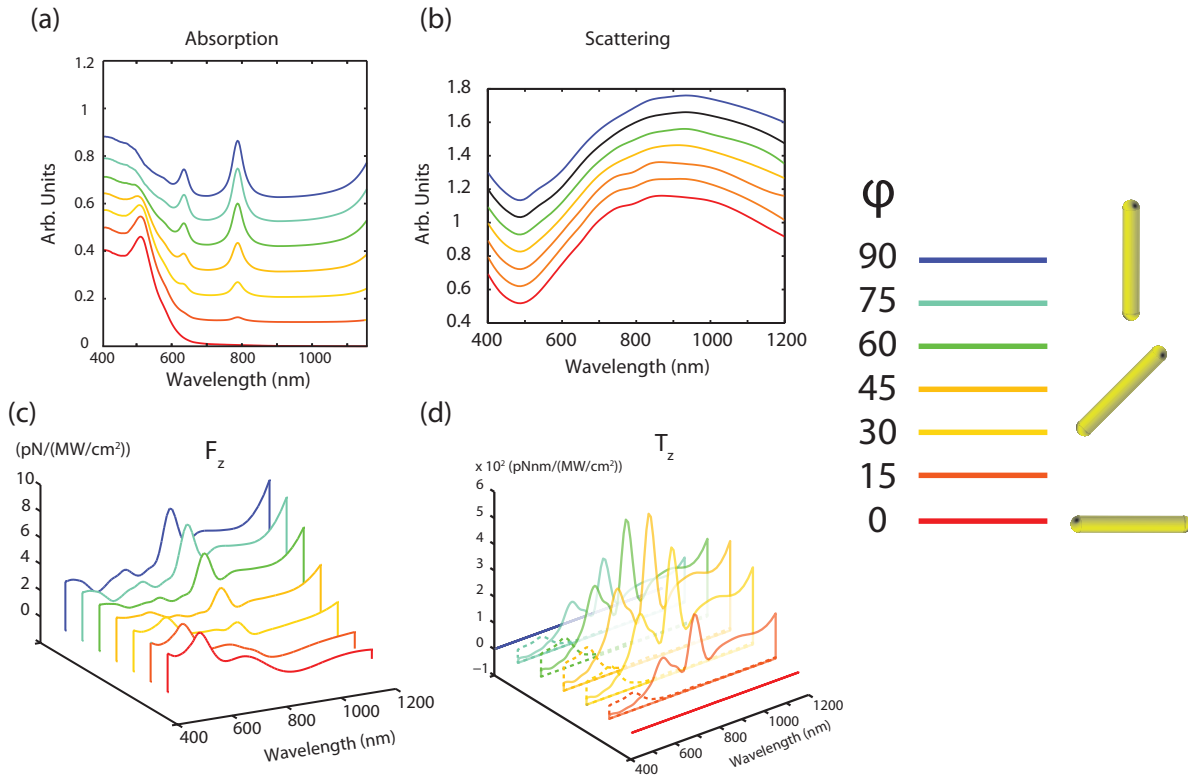


Figure 2.2: Characteristics of a nanowire in the  $x$ - $y$  plane for varying orientation angle  $\phi$  with  $\theta = 90^\circ$ . (a) Absorption cross-section. (b) Scattering cross-section, ((a), (b) spectra offset for clarity). (c) Net longitudinal force in the direction of light propagation,  $-F_z$ , associated with the plasmonic Lorentz force. (d) In-plane torque  $T_z$  produced by plasmons  $\mathbf{f}_M$  (solid lines) and the induced electric dipole  $\mathbf{f}_E$  (dashed lines).

When the wire is perpendicular to the light polarization ( $\phi = 0^\circ$ ), the longitudinal force is positive and pointed in a direction *opposite* to the light propagation, in a manner that is reminiscent of optical tractor beams [Ruffner and Grier (2012)]; when the wire is aligned parallel to the linear polarization of light ( $\phi = 90^\circ$ ), the longitudinal force increases significantly. It has generally been assumed that radiation pressure produces the strong longitudinal forces of nanowires; that longitudinal forces are *also* produced via surface currents implies additional considerations and the importance of understanding plasmonic Lorentz forces. Such plasmonic forces are strong even when there is minimal plasmonic absorption suggesting that the scattering off nanostructures plays a role.

Here we provide a comparison of the longitudinal components of  $\mathbf{T}_E$  and  $\mathbf{T}_M$  [Fig. 2.2(d)] which further points to the importance of plasmonically-induced Lorentz forces although the contributions are qualitatively similar in 2D. Both torque terms are negligible when either  $\phi = 0^\circ$  or  $\phi = 90^\circ$  and both terms are largest at  $\phi = 45^\circ$ . The trends are in agreement with prior experimental results where a nanowire tends to aligns parallel or perpendicular to the illuminating polarization Tong et al. (2010); however, the effect of surface plasmons is significantly larger than that associated with the electric dipole. The underlying physical phenomena associated with nanowires is wavelength-dependent: at the transverse resonance, the in-plane rotation of nanowires is produced by the induced electric dipole force  $\mathbf{f}_E$ . At longer wavelengths, it is the rotation induced by surface plasmons via Lorentz forces  $\mathbf{f}_M$  that dominates. This is a central conclusion of our investigation: plasmonically-induced Lorentz forces are significant at longer wavelengths and are often stronger than electric-dipole induced forces, even when there is minimal absorption due to plasmon excitation.

## 2.3 Translation and compressive plasmonic forces

### 2.3.1 Force Visualized for Various Illumination Wavelengths

A graphical representation of the forces produced by plasmons  $\mathbf{f}_M$  on three oblique geometries are illustrated with arrows in Fig. 2.3 for illuminating wavelength  $\lambda = 1071\text{nm}$ . The chiral-hybrid plasmons result from a superposition of the three lowest order modes ( $|m| \leq 1$ ) [Eq. 2.1]. The nanowire surface color denotes the relative strength of the time-averaged magnetic field. Chiral helices are also visible in the electric field. Both on and off resonance, the Lorentz forces yield compression forces on the nanowire. While the Lorentz forces are generally directed into and towards the axis of the nanowire, it varies in mag-

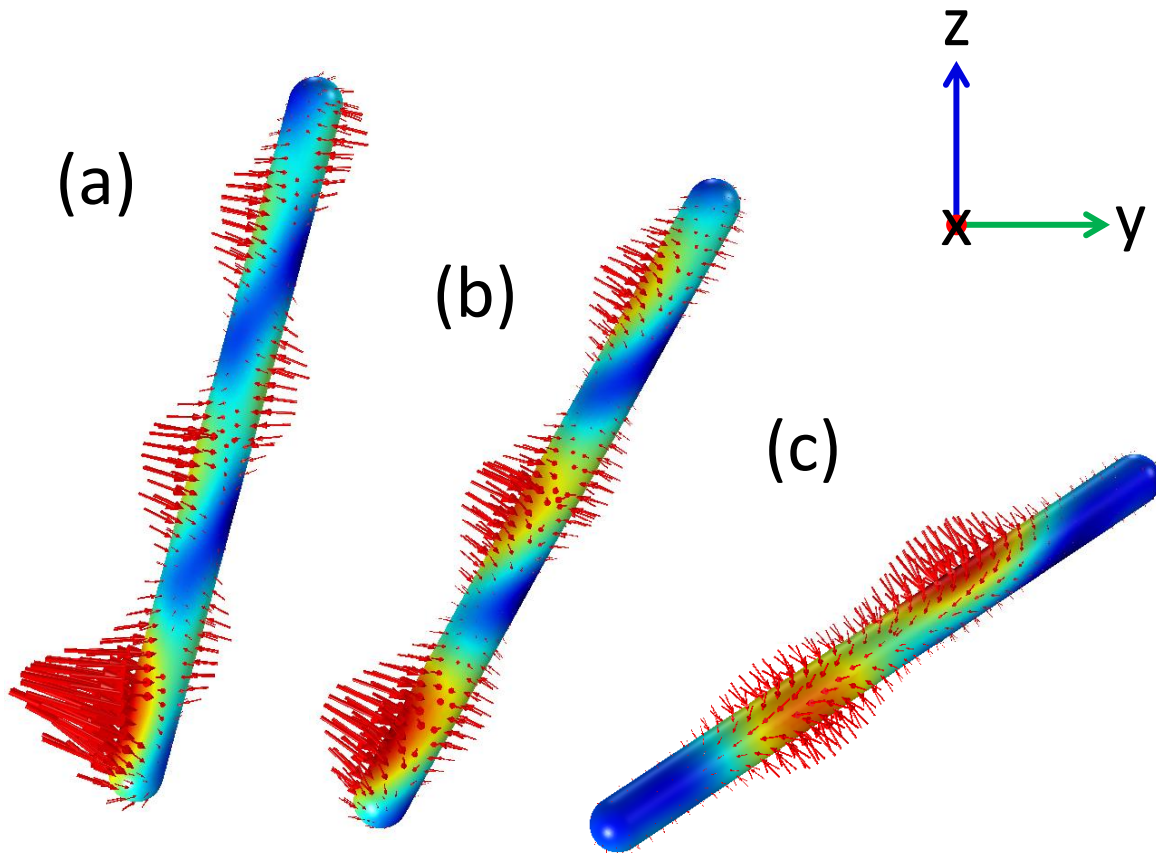


Figure 2.3: Forces on the nanowire surface produced by the surface currents (red arrows) and the norm of the surface magnetic field (surface colormap) for oblique geometries that excite the chiral hybrid plasmonic mode, where (a)  $\theta = 15^\circ, \phi = 90^\circ$  (b)  $\theta = 30^\circ, \phi = 75^\circ$  (c)  $\theta = 60^\circ, \phi = 60^\circ$  at  $\lambda = 1071\text{nm}$ .

nitude along the surface of the nanowire. In oblique illumination geometries ( $\theta \neq 0^\circ$  or  $90^\circ$ ), the magnetic-field and plasmonic Lorentz force patterns are not symmetric across the length or width of the wire. This break in azimuthal and longitudinal symmetry subsequently yields net forces in the  $x, y, z$  direction that would result in translation and torque of the nanowire. The origin of the asymmetrical profile along the length of the nanowire stems from the lossy nature of the material, plasmons are coupled into the nanowire via the termination and propagate the length of the nanowire, which acts like a low-Q Fabry-

Pérot resonator [Ditlbacher et al. (2005)]. The remaining part of this section describes the volume-integrated net translation forces; Sec. 2.4 will discuss the net torque of the nanowires.

Figure 2.4 illustrates  $\mathbf{f}_M$  for  $0 < \theta < 90^\circ$  and  $0 < \phi < 90^\circ$ . From this quarter-hemisphere, all nanowire positions are deduced. Five wavelengths are shown, which are uniformly spaced in the frequency domain. We illustrate a wavelength below the transverse resonance ( $\lambda = 441\text{nm}$ ), wavelengths associated with the transverse ( $\text{HE}_{\pm 1}$ ) and longitudinal ( $\text{TM}_0$ ) modes ( $\lambda = 517, 625,$  and  $790\text{nm}$ ), and a longer, off-resonance wavelength associated with the hybrid chiral plasmon ( $\lambda = 1071\text{nm}$ ). The orientations and wavelengths that correspond to Fig. 2.3 are marked. The color mappings are symmetrized; the components of  $\mathbf{f}_M$  are both positive and negative.

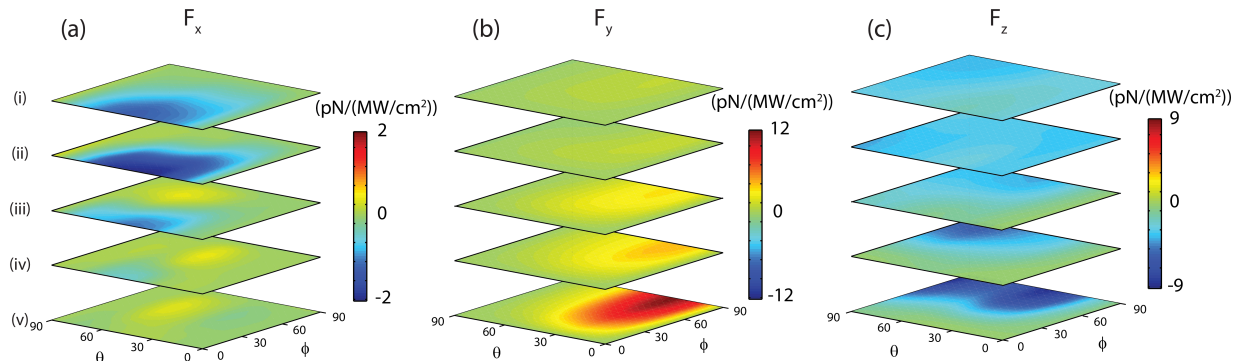


Figure 2.4: Net (volume-integrated) Lorentz forces associated with nanowire surface currents  $\mathbf{f}_M$  in (a)  $x$ -direction, (b)  $y$ -direction, and (c)  $z$ -directions for illuminating wavelengths  $\lambda =$  (i)  $441\text{nm}$  (ii)  $517\text{nm}$  (iii)  $625\text{nm}$  (iv)  $790\text{nm}$  (v)  $1071\text{nm}$ .

We find that the nanowire plasmons not only yield longitudinal forces [Fig. 2.2(c)] but also appreciable forces *perpendicular* to the light Poynting at wavelengths where there is lower absorption and higher scattering. In general, the largest net translation forces are produced in the  $y$ -direction or direction of light polarization. The force perpendicular to the polarization, that is, in the  $x$ -direction, is negative at lower wavelengths, but either positive

or negative at longer wavelengths, depending on the alignment of the wire. Moreover, the net translation forces are small on resonance compared to at longer wavelengths where chiral plasmons are present. For example, at the transverse and longitudinal resonances, that is,  $\lambda = 510\text{nm}$  and  $\lambda = 790\text{nm}$ , the net translation forces are at most  $2\text{pN}/(\text{MW/cm}^2)$ , whereas at the wavelength of  $\lambda = 1071\text{nm}$ , the net translation force is as much as  $15\text{pN}/(\text{MW/cm}^2)$ . Therefore, the Lorentz forces that occur via scattering transfer momentum to the nanowire in a manner that does not require strong plasmonic absorption since there is large scattering [Fig. 2.2(b)] yet low absorption [Fig. 2.2(a)] where Lorentz forces are greatest.

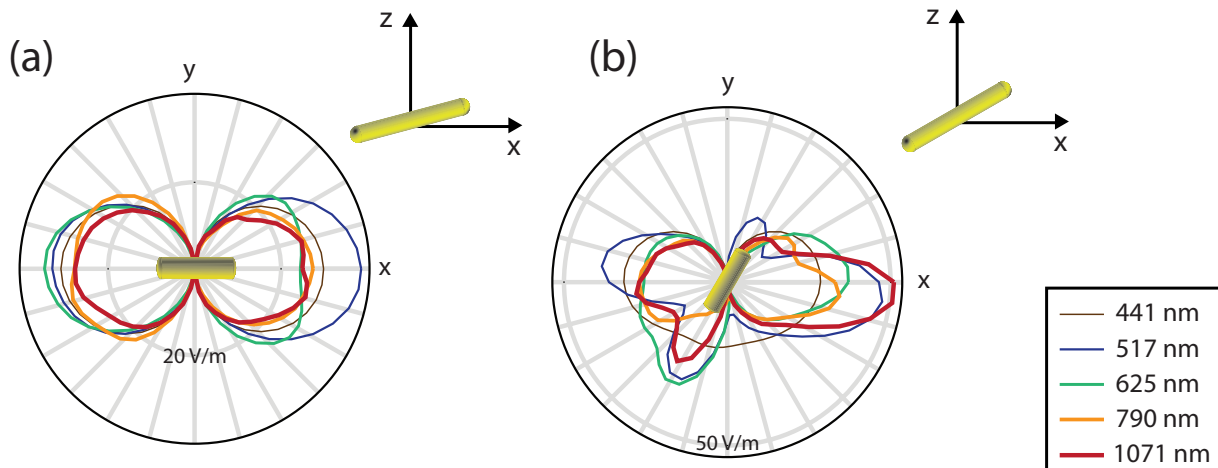


Figure 2.5: Far-field radiation patterns for a nanowire aligned (a) in the  $x$ - $z$  plane with  $\theta = 75^\circ$ ,  $\phi = 0^\circ$ , (b)  $\theta = 60^\circ$ ,  $\phi = 60^\circ$  for wavelengths  $\lambda = 441\text{nm}$ ,  $517\text{nm}$ ,  $625\text{nm}$ ,  $790\text{nm}$ , and  $1071\text{nm}$ .

### 2.3.2 Momentum Transfer via Scattering

We expect that momentum transfer in the transverse  $x$ - $y$  plane associated with plasmons is observable in the scattered fields in order for linear momentum to be conserved and simulations indicate that momentum conservation is visible in the far-field power. Figure 2.5 shows the electric field norm in the far field for two geometries to illustrate transverse

forces, from which the scattering dynamics can be extrapolated. We infer momentum transfer to the nanowire by the symmetry of the dipole radiation patterns. In Fig. 2.5(a), the nanowire is aligned in the  $x$ - $z$  plane with  $\theta = 75^\circ$  and  $\phi = 0^\circ$ . At this orientation, we calculate the Lorentz force in the  $x$ -direction to be either negative ( $\lambda = 441, 517\text{nm}$ ) or positive ( $\lambda = 625, 790, 1071\text{nm}$ ) depending on the illuminating wavelength [Fig. 2.4(a)]. We interpret that positive  $F_x$  at a wavelength of  $\lambda = 441\text{nm}$  is largely attributed to reflection since this wavelength is below the transverse-resonance cutoff. At higher wavelengths, the  $x$ -direction shifts in the far-field radiated power correspond with the sign of the plasmonic Lorentz forces in the  $x$ -direction. The shape of the far-field radiation corresponds to the characteristic dipole radiation from excitation of the longitudinal  $\text{TM}_0$  mode.

Similarly, in Fig. 2.5(b) we show similar far-field normalized power for geometry  $\theta = 60^\circ$  and  $\phi = 60^\circ$ . Below the cutoff for plasmon excitation ( $\lambda = 441\text{nm}$ ), we infer from the radiation pattern that momentum transfer in the  $y$ -direction due to reflection. At higher wavelengths, an ‘antenna’ behavior of the wire is apparent, the radiation pattern exhibits directionality. The dipole radiation mode in the  $y$ -direction and transverse modes are uncoupled at  $\lambda = 517\text{nm}$ , and the far-field radiation pattern is an ‘ $x$ ’ shape that is aligned with the axis of the nanowire. The size of the arms of the ‘ $x$ ’ shape determine the relative strengths of the dipole modes present, the arm perpendicular to the nanowire axis corresponds to the fundamental,  $\text{TM}_0$  mode and the arm parallel to the  $\text{HE}_{\pm 1}$  modes.

At longer wavelengths the plasmonic Lorentz forces are significant [Fig. 2.4]. For wavelengths and orientations that produce significant Lorentz forces we observe far-field radiation patterns that differ greatly in symmetry from dipole radiation patterns one might expect. For wavelengths of  $\lambda = 625, 790$ , and  $1071\text{nm}$ , the center of radiation pattern moves in the positive  $x$  and negative  $y$ -direction, corresponding with  $\mathbf{f}_M$  that is negative in the  $x$  and positive in the  $y$ -directions [Fig. 2.4]. Figure 2.5 indicates that the

plasmonically-induced Lorentz forces result in 50-70% changes in far-field radiated power, which is experimentally measurable.

## 2.4 Torque in 3-dimensions

### 2.4.1 Torque Visualized for Various Illumination Wavelengths

The vector components of the dipole moment and plasmonically-induced Lorentz torque [ $\mathbf{T}_E + \mathbf{T}_M = (T_x, T_y, T_z)$ ] are shown in Fig. 2.6 for five wavelengths (441, 517, 625, 790, and 1071nm as chosen in the previous section). Large values of  $T_x$  and  $T_z$  represent large torques that rotate the nanowire in both the polar and azimuthal directions.  $T_x$  and  $T_z$  increase in magnitude as wavelength increases which correlates well to the existence of chiral hybrid modes at longer wavelengths. Subsequently, whether  $T_x$  and  $T_y$  are positive or negative depends on the polar orientation of the nanowire.

The orientations that produce large net translation forces [Fig. 2.4] do not necessarily coincide with large torques [Fig. 2.6]; the greater the asymmetry in  $\mathbf{f}_E$  and  $\mathbf{f}_M$ , the greater the torque. We find that the maximal torques produced by plasmons ( $\mathbf{T}_M$ ) are an order of magnitude larger than the maximal torques produced by dipole moments ( $\mathbf{T}_E$ ). Moreover,

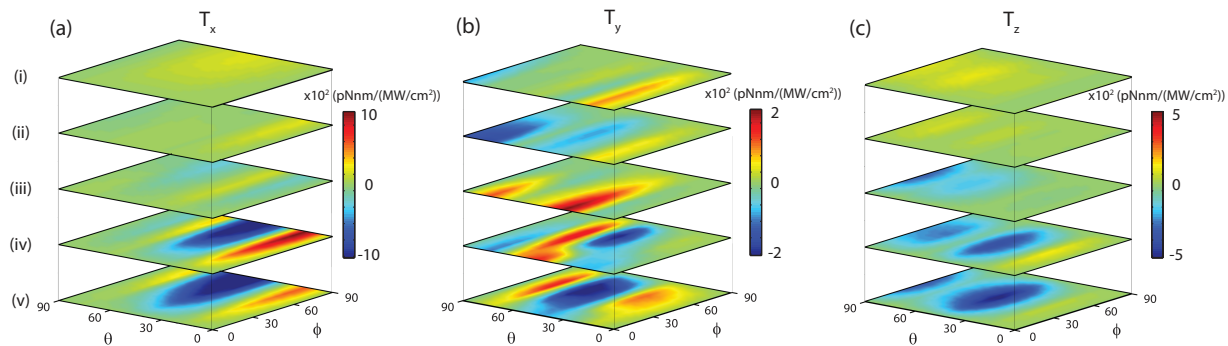


Figure 2.6: Torque around the (a)  $x$ -axis, (b)  $y$ -axis, and (c)  $z$ -axis at (i) 441nm, (ii) 535nm, (iii) 625nm, (iv) 790nm, and (v) 1071nm.

the magnitude of  $\mathbf{T}_E$  is negligible at wavelengths above 600nm; above 600nm,  $\mathbf{T}_M$  dominates. The magnitude of the  $\mathbf{T}_E$  is the same sign in our hemisphere quadrant of  $\theta$  and  $\phi$  since  $\mathbf{f}_E$  uniformly aligns the induced dipole with the axis of field polarization. In contrast,  $\mathbf{T}_M$  changes sign with nanowire orientation and illuminating wavelength [Fig. 2.6], which reflects the sensitive nature of the chiral hybrid plasmon.

### 2.4.2 Phase Diagram Illustrations

When the nanowire is free to rotate in three dimensions, the rotational behavior becomes complicated. The torque on the nanowire causes rotation which subsequently changes the torque on the nanowire. The results of this system that only accounts for Lorentz forces yields nonlinear dynamics that are beyond the scope of this paper; nonetheless, we illustrate the dynamics with a phase portrait of the torques in spherical coordinates. The rotation in the  $\theta$  and  $\phi$  directions associated with  $\mathbf{T}_E + \mathbf{T}_M$  are:

$$A_\theta = -\sin \phi T_x + \cos \phi T_y \quad (2.8)$$

$$A_\phi = T_z. \quad (2.9)$$

The phase portrait, i.e. vectors  $[A_\phi, A_\theta]$  as a function of  $\theta, \phi$  of the nanowire are plot in Fig. 2.7.  $A_\theta$  and  $A_\phi$  are not equivalent to the angular acceleration since the rotational inertia, which changes as a function of angle, has not been taken into consideration. Moreover, the angular velocity will also influence the angular acceleration when the rotational inertia changes. Nonetheless, we gather understanding of the nanowire's stable orientations and dynamics from Fig. 2.7.

Points of stability occur when the angular motion is zero, which occurs when the torque is zero. Stable points occur when the vector field flows toward the point of zero torque; un-

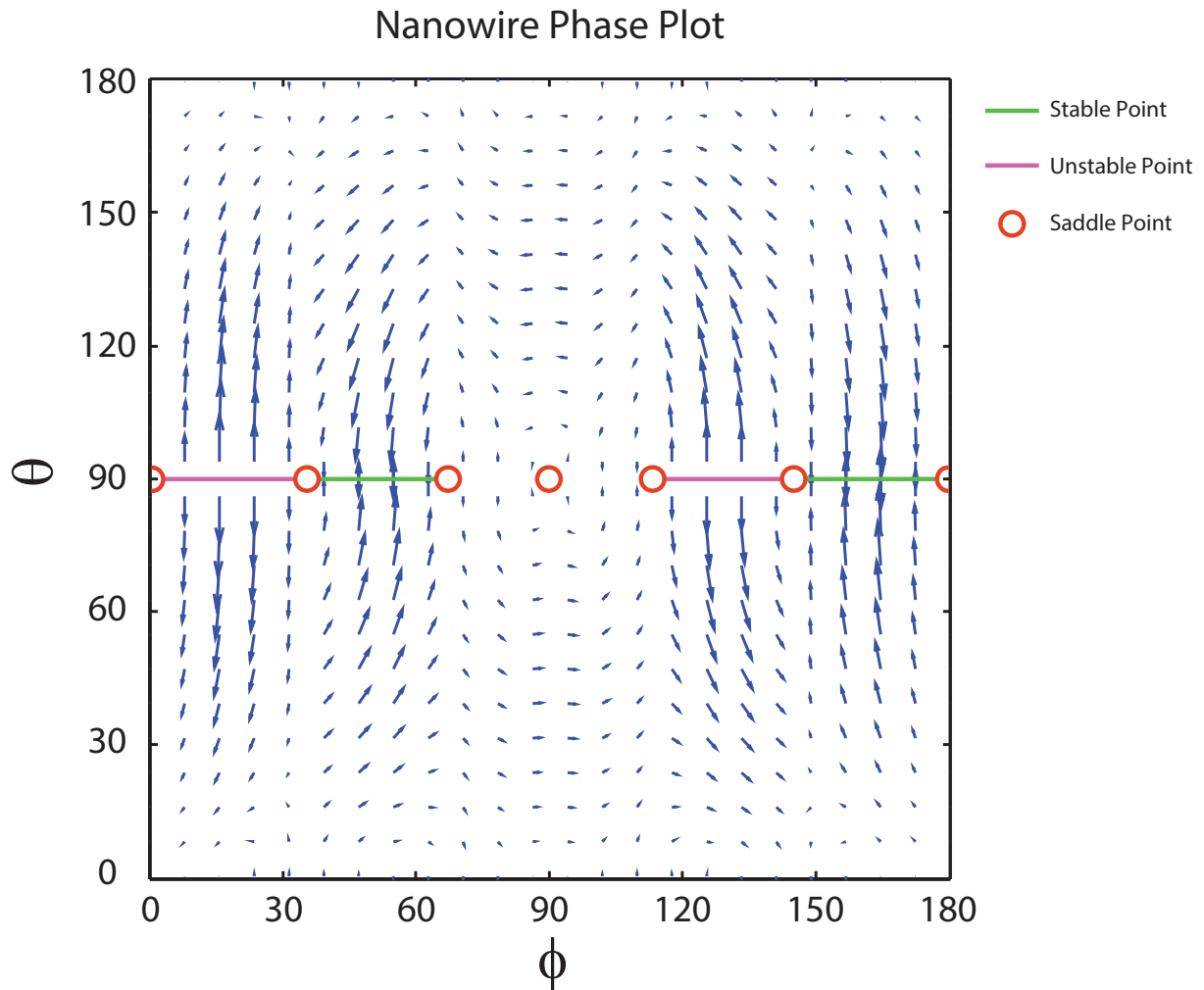


Figure 2.7: Phase portrait of the torque forces calculated at  $\lambda = 1071\text{nm}$ . Arrows in the  $x$  and  $y$  directions indicate torque that rotates the nanowire in the  $\phi$  and  $\theta$  directions respectively.

stable points occur when the vector field flows away from the point of zero torque [Strogatz (1994)]. Saddle points occur when the vector field flows toward the point of zero torque in one direction, and away in another.

Similar to our observation with 2D nanowire dynamics [Sec. 2.2], the nanowire aligns either parallel or perpendicular to the axis of polarization in a 3D system, settling at a stable point. Stable points occur when either  $\theta$  or  $\phi$  are equal to  $0^\circ$  or  $180^\circ$ , and  $\theta = 90^\circ$

consistent with the strong orientational trapping observed in previous research [Yan et al. (2012b); Tong et al. (2010)]. Interestingly, along the line of  $\theta = 90^\circ$  stable, unstable and saddle points exist and illustrate many rich and complicated dynamics already reported with the optical trapping of nanowires. Around stable fixed points oscillatory dynamics occur: the nanowire will rotate, but more specifically, it will rock and spin in an oscillatory manner. Fig. 2.7 also explains the rotational accelerations and rapid reversals seen in light-driven experiments [Shelton et al. (2005)] that are associated with the saddle point behavior and sharp inflections, such as those dynamics indicated at  $\theta = 90^\circ$ .

We allude to competing dynamics between the induced electric dipole and surface plasmons and are the first to explain the prior experimental observations that often contradict. It has been previously reported that nanowires align parallel or perpendicular to the linear polarization of an optical trap. A theoretical model that limits consideration to  $\mathbf{T}_E$  only explains the stable alignment of the dipole parallel to the polarization. Yet moreover, prior experiments employ trapping wavelengths in the near-IR [Tong et al. (2010)], where we predict the magnitude of  $\mathbf{T}_E$  to be negligible. Our model is the first to predict and explain the stable orientations of the nanowire, with longitudinal axis both parallel and perpendicular to the field polarization.

## 2.5 Conclusion

In conclusion, we have shown that plasmonically-induced Lorentz forces are significant and greater than dipole-moment-induced forces, particularly at long-wavelength excitation between plasmon resonances. The nanowire forces produced by plasmons lead to axial compression, which changes spatially along the nanowire surface depending on the nanowire orientation. The existence of chiral plasmons coincides with spiral magnetic-field patterns that produce net transverse forces and torques, which we predict are experimentally observ-

able in the far-field radiated power and polarization. The plasmonically-induced Lorentz forces are expected to interfere with the optical trapping of nanowires; selection of a laser-trap wavelength that prevents the excitation of the chiral plasmonic modes will enable greater control over the optical manipulation of nanowires.

The rotational dynamics present a highly nonlinear and complicated problem due to the sensitive nature of the plasmonic resonance that conventional ray optics cannot explain. The plasmonically-induced Lorentz forces and torques produce rotational motion consistent with the spinning, rocking, and rapid reversals in rotation observed experimentally with elongated plasmonic nanoparticles. Plasmonically-induced torque may oppose the dipole-induced torque, although the Lorentz torque dominates almost completely above the transverse resonance of the nanowire. Our theoretical investigation is the first to properly explain the stable positions of nanowires under illumination of linearly-polarized electromagnetic fields, and reveals a rich system of optomechanical plasmonically driven dynamics that has not yet been explored.

Our work points to novel methods that manipulate conducting nanoparticles that do not result in the extreme absorption and heating generally associated with the excitation of plasmons; we show that strong plasmonically-induced Lorentz forces occur off-resonance where plasmonic absorption is minimal. This outcome is highly relevant to the development of new devices and mechanisms that efficiently leverage the nonlinear mechanical dynamics of conducting nanoparticles in fluids, not limited to elongated conducting particles but also chiral nanoparticles, polymer materials, and carbon metastructures.

## 2.6 Future Work

Future work on this subject may involve experimental verification of the theoretical and numerical components of the work shown here. An experiment may consist of an microscope

setup with two tightly focused beams at different wavelengths. One beam would act as the optical trapping beam that would stabilize the nanowire at the focal point of the microscope setup similar to the setups described in the references [Ashkin (2001); Lee and Padgett (2012); Kuo (2001); Lang and Block (2003)], and the other would act as the excitation beam that would generate the Lorentz forces described in this chapter.

# Chapter 3

## Robustness and spatial multiplexing via diffractal architectures

### 3.1 Introduction

Many natural systems exhibit fractal properties [Mandlebrot (1982)]; in fact, scale invariance underlies many self-similar phenomena, from frost crystallization to animal colouration to stock-market pricing. In the realm of optics, the fractal anatomy of systems is widely associated with aggregated dielectric and metal colloids Sorensen (2001), crystals [Macke et al. (1996)], and tissues [Schmitt and Kumar (1998)]. Fractal systems are also observed in nonlinear optics [Soljacic et al. (2000); Segev et al. (2012)] and fractalized optical properties can even efficiently characterize or enhance the response of materials [Stockman et al. (1992); Tsai et al. (1994)]. Less well utilized are the features of diffractals, or the diffraction patterns of fractal signals [Berry (1979); Horvath et al. (2010); Hou et al. (2004)]. Diffractals feature in methods of encrypting data [Barrera et al. (2012)] as a versatile approach to double random-phase encoding [Unnikrishnan et al. (2000)]. However, to differentiate from previous work we exploit fractal architecture to improve transmission robustness.

Here, we explore diffractals for their application in signal processing [Verma et al. (2013, 2012)]. We show that the free-space propagation of diffractal-signal architectures provides algorithmic value and spatial multiplexing properties; any arbitrary subsection of a diffractal contains sufficient information to recreate the original sparse signal that is transmitted with a specific fractal architecture. In a manner similar to compressive imaging [Duarte et al. (2007); Howland and Howell (2013)]—where sparse signals reveal greater information via the diffraction through structures—here the fractal structuring within the signal sparseness prevents the loss of information.

Like other applications of fractals in communications applications, the diffractal architecture exhibits trade-offs. Fractal antennas for the radio frequency and microwave regimes are known for being compact and versatile over wide spectral bands but are power intensive [Radonic et al. (2012); Puente-Baliarda et al. (1998)]; fractal encoding algorithms enable image compression with higher-resolution at the expense of greater algorithmic complexity [Jacquin (1993)]; here, our research identifies that diffractal architectures prevent the loss of information but require greater signal preprocessing. This investigation extends our understanding of fractal structures in signal communications and may increase robustness and transmission rates of satellite, wireless, and interplanetary communication systems, *i.e.*, networks that support a large number of roaming receivers.

The remainder of this chapter is organized as follows. First, we formalize the form of a transmitted fractal signal, show that its far-field diffraction pattern or diffractal is also a fractal, and illustrate the reciprocal nature of fractals with the Sierpinski carpet. Secondly, we demonstrate the robust retrieval of a signal from a diffractal; the original signal is reconstructed even when the majority of the diffractal signal is blocked. Finally, we discuss the future applications for diffractal spatial multiplexing in free-space communication systems and conclude.

## 3.2 Theoretical Description

### 3.2.1 Spatial Multiplexing of the Diffractal

We generate the fractal transmittance pattern from any base matrix via recursive iterations where the matrix is resized and convolved with itself repeatedly [Allouche and Shallit (2003)].

The base matrix  $B(x, y)$  adopts a general form,

$$B_i(x, y) = \sum_j \delta(xr^{i-1} - x_j, yr^{i-1} - y_j), \quad (3.1)$$

where the subscript denotes the iteration  $i$ ,  $r > 1$  is the relative scaling between iterations, and  $\delta(x - x_j, y - y_j)$  is the Dirac delta function at  $x = x_j$  and  $y = y_j$ . The fractal transmittance function  $T(x, y)$  is calculated recursively,

$$T_n(x, y) = T_{n-1}(x, y) * B_{n-1}(x, y), \quad (3.2)$$

where the subscript denotes the order of the fractal or its expression at the  $n^{th}$  iteration,  $T_0$  is the initial profile of 1's, and  $*$  denotes the convolution operator.

Subsequently, the diffractal is the Fourier transform or the far-field of the transmittance function  $\tilde{T}$  [Horvath et al. (2010)],

$$\tilde{T}_n(k_x, k_y) = \tilde{T}_0(k_x, k_y) \prod_{i=1}^n \tilde{B}_i(k_x, k_y). \quad (3.3)$$

The Sierpinski carpet is one example of a fractal that is generated by this process and via the iterated substitution of a  $3 \times 3$  base matrix of ones with removal of the center

element:

$$\left\{ 0 \rightarrow \begin{bmatrix} 0 & 0 & 0 \\ 0 & 0 & 0 \\ 0 & 0 & 0 \end{bmatrix}, 1 \rightarrow \begin{bmatrix} 1 & 1 & 1 \\ 1 & 0 & 1 \\ 1 & 1 & 1 \end{bmatrix} \right\}. \quad (3.4)$$

The second substitution of Eq. 3.4 represents the mathematical expression for the base matrix  $B_0(x, y)$ . In the case of the Sierpinski-carpet base-matrix elements,  $r = 3$ , and  $x_j$  and  $y_j$  are the perimeter coordinates of a  $3 \times 3$  9-unit block centered at the origin, and  $(x_j, y_j) \in [(1, 1), (1, 0), (1, -1), (0, -1), (-1, -1), (-1, 0), (-1, 1), (0, 1)]$ . Since each of the Dirac delta functions in  $B_0(x, y)$  yields a phase shift in the Fourier domain, *i.e.*,  $\mathcal{F}\{\delta(\alpha x - x_i)\} = e^{2\pi i c k_x x_i} / |\alpha|$ , its scaled Fourier Transform at the  $i^{th}$  iteration of the Sierpinski carpet [Eq. 3.1] becomes:

$$\tilde{B}_i(k_x, k_y) = (2/r)^{i-1} [\cos(2\pi 3^{1-i} k_x) \cos(2\pi 3^{1-i} k_y) + \cos(2\pi 3^{1-i} k_x) + \cos(2\pi 3^{1-i} k_y)]. \quad (3.5)$$

With each iteration, the spatial frequency components  $k_x, k_y$  of the diffractal increase by a factor of 3 and spread the diffractal across a 3-times wider  $k_x, k_y$ -range, which is evident in Eq. 3.5; the cutoff of  $\tilde{T}_n$  scales in proportion with  $k_x, k_y \propto r^{n-1}$ .

We calculate the Sierpinski carpet  $T$  recursively [Eq. 3.2]: a second-order fractal is generated from the Kronecker tensor product of the base matrix  $\begin{bmatrix} 1 & 1 & 1 \\ 1 & 0 & 1 \\ 1 & 1 & 1 \end{bmatrix}$  with itself; a third-order fractal is generated from the Kronecker tensor product of a second-order fractal and the same base matrix [see Code File 1 Moocarme (2015a)]. Sierpinski carpets of  $n = 1, 3$ , and 5 are shown in Fig. 3.1a) with the corresponding diffractals  $\tilde{T}$  [Fig. 3.1b)].

```
function carpetHolo = Sierpinski(fracOrder);

carpetBase = ones(3); % Initialize matrix
carpetBase(2,2) = 0;
% Zero middle element
```

```

if fracOrder==0;
    % For zero order case
    carpetHolo = carpetBase;
else
    % For higher order cases
    carpetHolo= kron(carpetBase ,carpetBase );
    % For loop iterates the Kronecker tensor product
    for i = 1:fracOrder-1
        carpetHolo = kron(carpetHolo ,carpetBase );
    end
end
end

```

As the fractal order increases,  $\tilde{T}$  exhibits smaller self-similar features at higher  $k_x, k_y$ ; the diffractal also exhibits a fractal architecture, as observed in other literature [Berry (1979); Horvath et al. (2010)]. Moreover, when  $n$  is large, an arbitrary subsection of  $\tilde{T}$  closely resembles the whole, and the self-similarity is already apparent with  $n = 5$  [Fig. 3.1c-d)]. The iterated, self-similar, wide-spatial-frequency features contained in the diffractal  $\tilde{T}_n$  [Eq. 3.3] enable robust reconstruction of itself, which is described in the next subsection.

### 3.2.2 Robust reconstruction of a blocked diffractal signal

We now refer to the sparse matrix  $B_0$  and transmitted signal  $T$  as the original and fractalized signal, OS and FS, respectively; the diffractal signal DS is  $\tilde{T}$ , or, the Fourier transform of FS; BDS refers to an off-axis subsection of DS that is filtered; a reconstructed fractalized signal RFS refers to the inverse-Fourier transform of BDS; a regenerated version of the original signal ROS interpolates RFS in order to obtain OS.

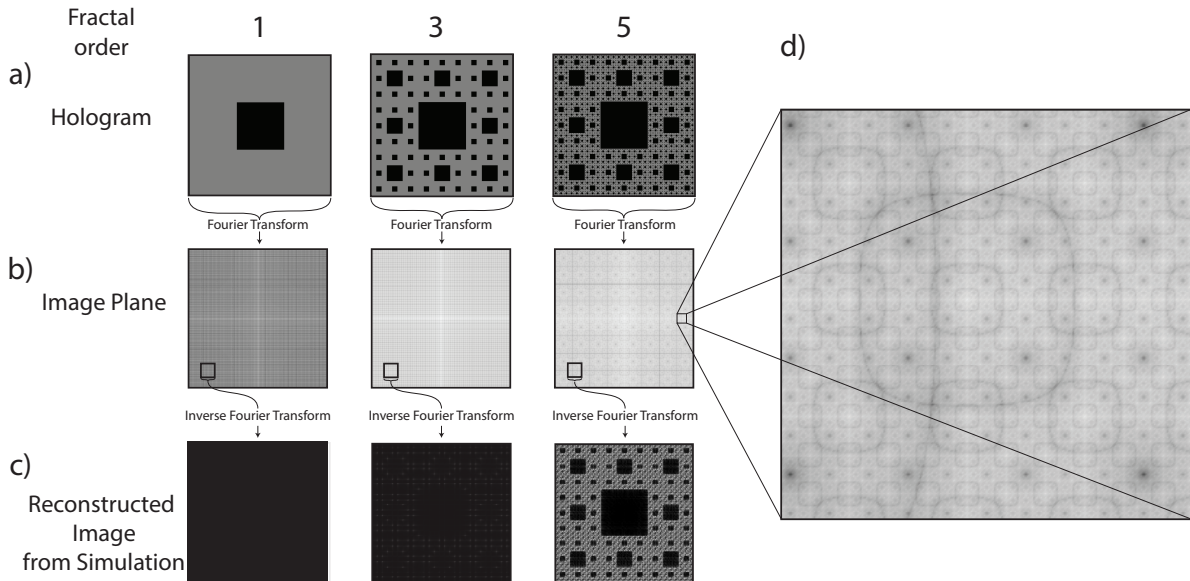


Figure 3.1: a) Signal patterns, or fractalized signals (FS) of orders  $n = 1, 3$ , and  $5$ . b) Corresponding Fourier transforms of signals on logarithm scale, or diffractal signals (DS). c) Reconstructed Fourier-transforms (RFS) from the 1% black-outlined subset, the blocked diffractal signal (BDS). d) Enlargement of a portion of the  $n = 5$  diffractal, which illustrates similar patterns at different length scales.

In Fig. 3.1(b), a subsection or BDS is outlined with a black square, which represents 1% of DS. The corresponding RFS from BDS are shown in Fig. 3.1(c). For  $n = 1, 3$ , RFS is ostensibly blank because BDS carries negligible power. In contrast, when  $n = 5$ , RFS carries features that resemble FS. We refer to the capacity to reproduce FS with 1% of the off-axis area from DS as *robust* reconstruction.

Robust reconstruction—where RFS resembles FS—is possible even when the size of BDS is significantly reduced [Verma et al. (2013)]. A corresponding increase in the FS fractal order  $n$  will yield RFS that resembles FS when BDS is arbitrarily small. With the example of the Sierpinski carpet, Fig. 3.1(a)–3.1(c), if the size of BDS is reduced to 1% of OS, then a comparable RFS is produced by increasing the fractal order of FS from  $n = 1$  to  $n = 5$ .

Here, we also refer to robust reconstruction as the capacity to regenerate OS from RFS from a simple threshold function [see Code File 2 Moocarme (2015b)]. The threshold function of the Sierpinski carpet divides RFS into a  $3 \times 3$  array (identical size as OS) and measures the intensity in each of the 9 elements. Above a certain threshold value, the element is assigned a value of 1, and otherwise assigned a value of 0. The  $3 \times 3$  array that is processed with the threshold function, ROS, is theoretically identical to OS when OS is transmitted with the diffractal architecture.

```
function recon = reconFun( Threshold , carpetBaseLength , carpetHolo )
    % Ratio of length of hologram
    normLength = length(carpetHolo)/carpetBaseLength;

    % Convert to array of cells
    cellHolo = mat2cell( carpetHolo , repmat( normLength , 1 , ...
        carpetBaseLength ) , repmat( normLength , 1 , carpetBaseLength ) );

    % Calculate mean, determine if above threshold value, and plot
    pcolor( double( cell2mat( cellfun( @mean2 , cellHolo ))>Threshold ) );
end
```

The comparison between RFS and FS in peak signal-to-noise ratio (PSNR) for various fractal orders as a function of the fractional BDS size is shown in Fig. 3.2. The error bars represent the standard deviation from the mean value of 200 random locations of BDS. Since the size of RFS is reduced from FS, RFS is resized with nearest-neighbour interpolation. We provide 2 observations from Fig. 3.2: first, when BDS is greater than 0.01% of the fractional size of FS, larger fractal orders produce higher PSNR; second, as the fractional area of BDS increases the location of BDS becomes irrelevant since the standard

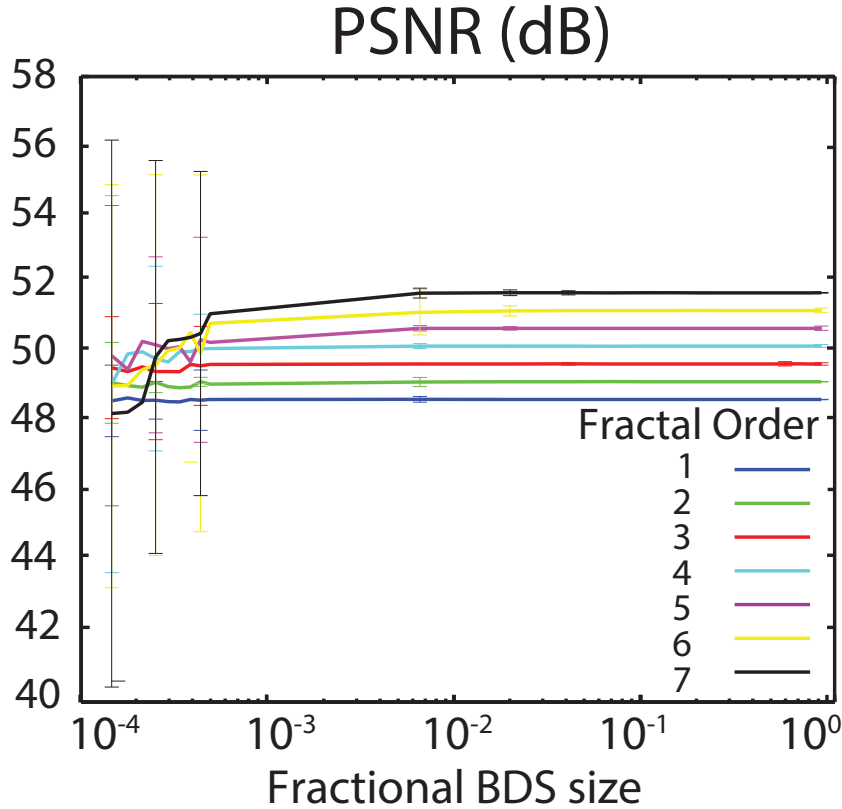


Figure 3.2: The peak signal-to-noise ratio (PSNR) of RFS to FS for various fractal orders as a function of the fractional BDS size.

deviation around the mean diminishes. For fractional BDS sizes smaller than 0.01% lower fractal orders yield a higher PSNR since the minimum size matrix needed to completely recreate FS is larger for higher fractal orders. For example the minimum size matrix needed to recreate FS of order 1 is  $3 \times 3$ , for FS of order 2 it is  $9 \times 9$ , etc.

We observe that ROS is generally identical to OS when BDS is above 0.01% and the fractal order is greater than 3, regardless of BDS location. A partial explanation for the robust reconstruction is that increasing-order FS carry arbitrarily-high  $k_x, k_y$  and enable arbitrarily-small BDS to carry the information of FS or OS. If we strictly limit OS to binary or Dirac-delta functions, then FS has no  $k_x, k_y$  cut-off and as  $n$  approaches infinity,

fractaled features appear in FS without a  $k_x, k_y$  cut-off. In fact, the amplitude of the additional  $k_x, k_y$  gained from each iteration scales inversely with  $r^{n-1}$ , which provides a detection limit only in practice; in theory, each iteration generates high- $k_x, k_y$  copies of OS [Eq. (3.4)] that are spatially distributed from the origin.

Yet it is worth noting that the robust reconstruction is achieved because the diffractal architecture also couples  $k_x$  and  $k_y$  in iterated products [Eq. (3.3)]. As a result, RFS will resemble FS when either the BDS size *or location* changes. In a manner similar to spatial filtering, RFS will produce outlines of FS if  $n$  is not sufficiently large; however, unlike a high-pass spatial filter of a multi-scale random high- $k_x, k_y$  pattern [Duarte et al. (2007)], a change in the location or the size of BDS will not distort the outline of RFS. Subsequently, the diffractal architecture provides superior performance over other algorithms that regenerate sparse data, OS [Duarte et al. (2007); Howland and Howell (2013)].

### 3.3 Experimental Results

We experimentally demonstrate the features of diffractals with a 4-*f* optical arrangement where the 2-dimensional Fourier transform of a collimated fractal image, DS, lies in the focal plane of an imaging lens Goodman (2005). The experimental setup that produces, filters and reconstructs FS is shown in Fig. 3.3a) and experimentally reconstructed images, RFS, are shown in Fig. 3.3b). An aperture of area approximately  $0.8\text{mm}^2$  blocks the majority of DS. The placement of the aperture is shifted roughly 4mm horizontally and 5mm vertically from the central point, in the focal plane of the lens. The SLM image has a resolution of  $800 \times 600$  pixels (16mm  $\times$  12mm).

When we employ diffractal architectures of high orders ( $n > 4$ ), we observe the phenomenon that is shown numerically: the placement of the aperture in DS is irrelevant in order to reconstruct the original image. When the aperture is moved laterally in the focal

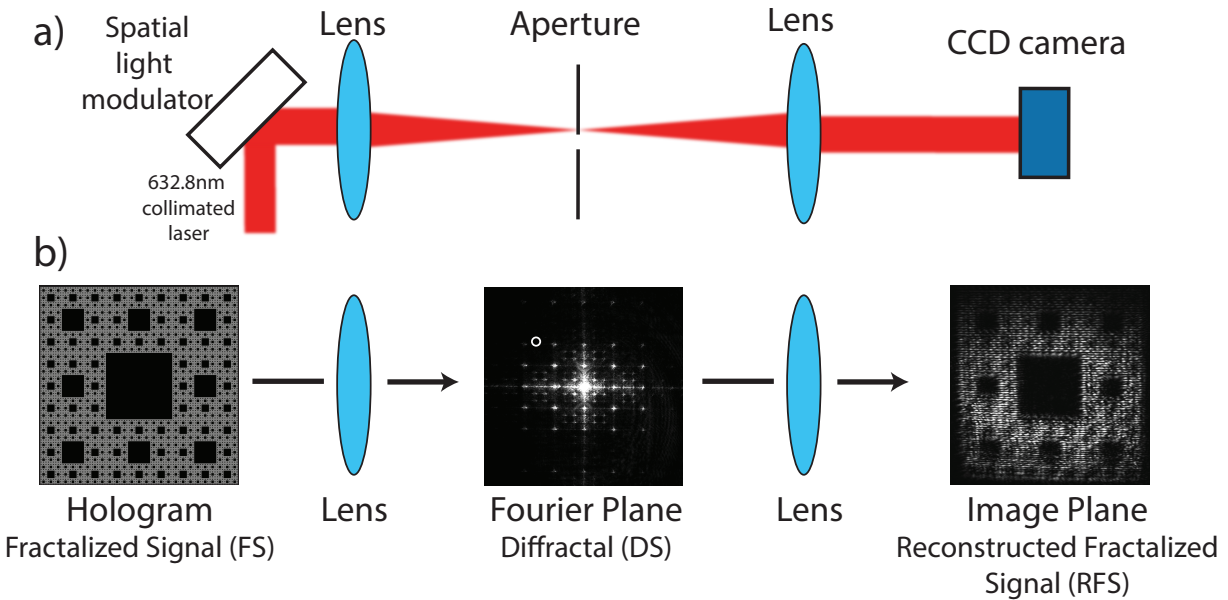


Figure 3.3: a) Light from a  $\lambda = 632.8\text{-nm}$  wavelength laser is spatially filtered, expanded, and collimated and illuminates the full area of a 800x600 pixel spatial light modulator (SLM). The 4-*f* system is composed of 2 5-cm lenses placed after the SLM. The first lens Fourier transforms the fractal signal (FS) at the focal plane. An aperture is placed off-center at the focal plane and only transmits a portion of the diffractal (BDS). The second lens reconstructs the SLM image with the light that is transmitted through the aperture. b) The Sierpinski carpet hologram of order  $n= 5$ , CCD image in the focal plane of the hologram after the lens, and the reconstructed image. A circle denotes the area utilized to reconstruct the image.

plane, RFS maintains strong resemblance to FS. In fact, only the intensity of RFS diminishes as the aperture translates further from the DS center; the outline remains fixed as the aperture moves. For smaller fractal orders, RFS resembles FS only when the aperture is placed within 0.8mm of the center, where the spatial frequency components are concentrated. The signal-to-noise of the experiment and CCD camera sensitivity limit effective reconstruction, while the highest order  $n$  is of FS is limited by the number of SLM pixels.

### 3.4 Discussion of Applications

Here we make the distinction that diffractals are specific fractal structures. Not all fractals enable robust signal communications and the recursive transformation employed to generate FS and DS in Eqs. 3.1 and 3.5 differ fundamentally. For example, both of the Fourier Transform pairs FS and DS are fractals and carry iterated, self-similar features, but if we reverse their roles in our transmission system, the reconstruction will instead depend severely on the size and location of BDS. In fact, if in the example of the Sierpinski carpet, the center subsection becomes BDS, then the ROS will not resemble the OS, regardless of fractal order. The diffractal is unique from general fractals and self-similar scale-invariance alone is an insufficient precondition for our system of robust reconstruction and spatial multiplexing.

It may seem contradictory that higher-order fractals lead to more robust signal transmission since the finer structure of a higher-order fractal is itself harder to reconstruct. There are two perspectives of diffractals that explain the robust reconstruction. Firstly, the self-similar structures of higher-order fractals have a greater spatial frequency range and finer detail, and subsequently smaller BDS carry sufficient information to reconstruct OS. Secondly, the higher-order diffractals carry higher spatial-frequency components where the  $k_x$  and  $k_y$  components are coupled, and subsequently the location of the subsection in DS is unimportant. Here we have shown that BDS of arbitrary size and location carry sufficient information to reconstruct OS but in practice, there exists clear limitations for the robust reconstruction even in the limit of infinite-order FS.

Note: it may also seem contradictory that an infinitesimally-sized BDS with infinitesimal power can carry information— this is not actually true: there is a minimal size for BDS fixed by the pixelation of the SLM. There exists a trade-off with the diffractal architecture between robust reconstruction and high bit rate; a greater bit-rate is achieved with a larger

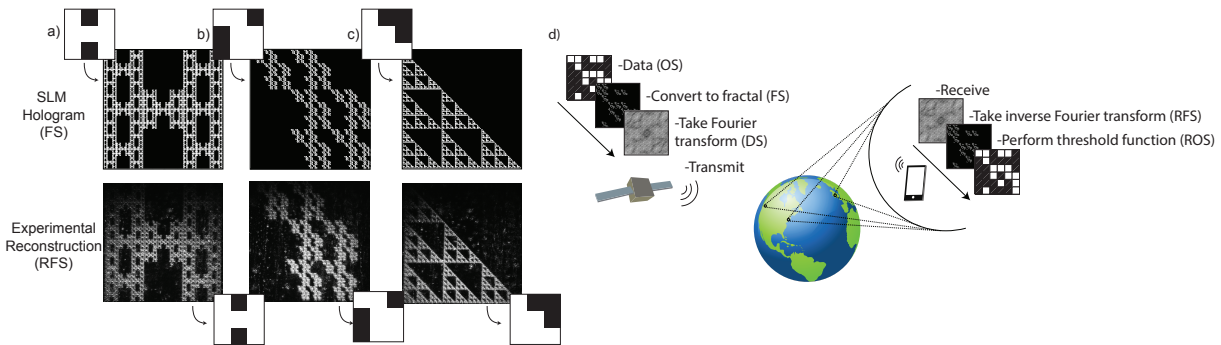


Figure 3.4: Three examples of 512 9-bit spatial patterns, associated with base matrices a)  $\begin{bmatrix} 1 & 0 & 1 \\ 1 & 1 & 1 \\ 1 & 1 & 0 \end{bmatrix}$ , b)  $\begin{bmatrix} 1 & 1 & 0 \\ 0 & 1 & 1 \\ 0 & 1 & 1 \end{bmatrix}$ , and c)  $\begin{bmatrix} 1 & 0 & 0 \\ 1 & 1 & 0 \\ 1 & 1 & 1 \end{bmatrix}$ . The fractal signals FS are shown with their corresponding experimentally-reconstructed fractal signals RFS from the experimental setup in Fig. 3.3a). The lower-right inset shows the reconstructed original signal ROS. d) Example application: transmitted fractal signal FS is received at a far-field distance as a diffractal signal DS, where a roaming set of receivers, with only a diffractal subsection BDS, reconstructs the original signal OS.

base matrix, which can limit the maximum fractal order that is transmitted. For example, with the  $3 \times 3$  or 9-element OS, there are 512 possible spatial bits, three of which are illustrated in Fig. 3.4a-c). A  $4 \times 4$  base matrix requires  $(\frac{4}{3})^{2n}$  more pixels than a  $3 \times 3$  to achieve the same fractal order,  $n$ . With a limited SLM pixel resolution, there is a choice between the generation of higher-order fractals and the utility of higher spatial bits.

If the trade-off between bit-rate and robust reconstruction are mitigated, then the diffractal architecture could support a large number of roaming receivers with only one transmitter, such as wireless or satellite networks shown in Fig. 3.4d). The self-similar properties of the diffractal architecture and their corresponding far-field pattern provide a method to reach a large number of receivers, possibly moving, without signal degradation. The processing times required in the calculation of FS from OS are not trivial and scale with  $r^{2n}$ . Secondly, the refresh rates of a spatial light modulator or similar adaptive-optics device present constraints on the maximum achieved bit rate, which requires further consideration.

This can be applied to more complex shapes and structures, for example, an  $16 \times 16$  pixel smiley face. The Fourier transform of the smiley face is taken; part of the Fourier transform is blocked; and a reconstruction of the image is attempted via the inverse Fourier transform. The same experimental procedure as shown in Fig. 3.3 is utilized. As can be seen from Fig. 3.5 when just the image is sent through the experimental setup the image reconstructed is not recognizable at all. However when the image is fractalized even just one order the image becomes recognizable. Unfortunately due to the limitations of pixels on the SLM no higher orders can be achieved.

Fractal structures have been utilized in signal communications and data compression for decades. Fractal antennas for the radio frequency and microwave regimes are known for being compact and versatile over wide spectral bands [Radonic et al. (2012); Puente-Baliarda et al. (1998)]. Fractal encoding algorithms enable image compressing with higher-resolution compression at the expense of greater algorithmic complexity [Jacquin (1993)]. The trade-off for higher resolution fractal-compressed images is higher processing times, which presents a limitation of their presence in data communications. Recently, however, there has been a resurgence of interest in fractal architecture due to their robust properties in optical transmission.

## 3.5 Conclusion

We have shown that the diffractal architecture provides the beneficial features of spatial multiplexing and robust reconstruction. We have centered our demonstrations with the Sierpinski carpet, a familiar fractal, although our results could have been demonstrated with 511 other patterns similarly imprinted with the diffractal architecture. Data that is transmitted with the diffractal architecture is highly robust to intermediate-obstacle signal

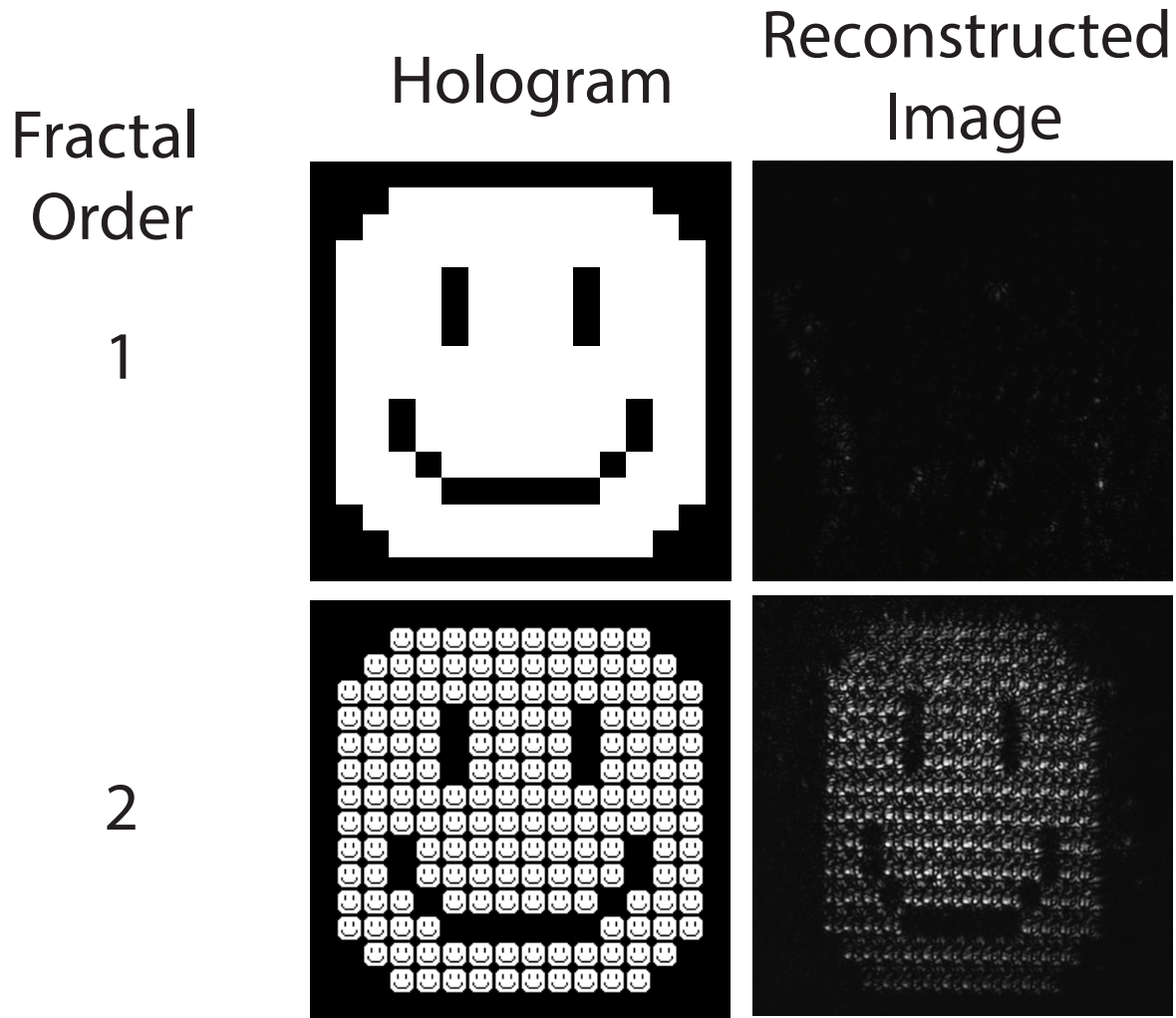


Figure 3.5: As an example of a more complicated image, a smiley face is fractalized, the Fourier transform is taken, 99% of the signal is blocked at the focal plane, and the image is reconstructed. This is compared to the original signal that is not fractalized.

blocks and diffractal subsections of arbitrary size and location carry sufficient information to regenerate the original signal without distorting outlines of its pattern. Our research illuminates potential applications in data transmission systems when one transmitter sends data to a large number of moving receivers or through noisy media.

## 3.6 Experimental Difficulties and Future Work

A SLM works well for experimentation because of its facile reconfigurability, however the resolution is limited to  $800 \times 600$  pixels, that limits the complexity of the data image sent in the process. Ways to overcome this could be to use photolithography to create transmission structures with a larger pattern on a glass film, however the structure would lose the reconfigurability that the SLM possesses. Transmission could even be created by printing the transmission structure pattern on transparency sheets, which would be a cheap alternative method to achieve similar results with a lower resolution.

# Chapter 4

## Meta-optical chirality and emergent eigen-polarization modes via plasmon interactions

### 4.1 Introduction

Metamaterials are composed of sub-wavelength components, or meta-atoms that individually alter the intensity and phase of light. When placed on a 2D surface, metamaterials are known as metasurfaces [Zhao and Alu (2011)] and have enabled many applications from quarter [Yu et al. (2011)], half-wave plates[Ding et al. (2015)], and cross-polarizers [Qin et al. (2016)], to ultra-thin lenses [Aieta et al. (2012); Ni et al. (2013)]. Chiral metasurfaces can ultimately be defined as those that exhibit a response dependent on the incident circular-polarization handedness, though the specific mechanism behind the phenomena has been debated; it has been argued that planar structures such as metasurfaces cannot exhibit true optical activity (OA) or circular dichroism (CD) without the excitation of magnetic resonances since certain 3D symmetry properties are not satisfied [Hentschel et al.

(2012); Eftekhari and Davis (2012)]. The equivalent response from planar metasurfaces can be achieved by alternate methods such as the interaction of plasmon modes [Eftekhari and Davis (2012); Fan and Govorov (2010)], or by non-radiative dissipation [Khanikaev et al. (2016)], and is named optical chirality. The difference in transmission from different polarization states due to optical chirality produces an *equivalent* effect to OA and CD.

Optical chirality in metamaterials is produced in several ways. Not surprisingly, a chiral metamaterial can be composed of chiral meta-atoms, in which the mirror image of the structure cannot be superimposed on the original [Zhang et al. (2014); Tang et al. (2016)]. Intrinsically chiral materials are chiral due to the geometry of the meta-atoms themselves, and exhibit chiral behavior at normal illumination incidence. Helices [Kuzyk et al. (2012)], gammadiions [Cao et al. (2013); Kwon et al. (2008)], or nanoparticle assemblies [Fan et al. (2010); Guerrero-Martinez et al. (2011)] are common examples of intrinsically chiral meta-atoms that exhibit a strong chiral response. Another approach that achieves chiral asymmetry is the creation of a linear phase gradient, *i.e.*, illumination at oblique incidence [Yannopapas (2009); Cao and Cryan (2012); Cao et al. (2015b,a); Proscia et al. (2016)] or spatial variation of the unit cell [Aieta et al. (2012); Yu et al. (2011); Shaltout et al. (2014)]. The chiral response that arises from the linear phase gradient of either of these approaches is associated with extrinsic chirality.

In this Letter we instead focus our investigation on the optical chirality that arises solely from the interactions between achiral meta-atoms. We postulate that the nonlinear coupling between meta-atoms originates from an interaction force derived from the Liénard-Wiechert potential [Jackson (1999)], which accurately predicts measured changes in the experimental transmission spectra. We study rectangular plasmonic resonators whose arrangement leads to chiral phenomena at normal incidence, or identical tilted achiral nanostructures in a lattice that lead to a chiral response. The individual nanostructures are achiral, yet the

periodic array is chiral [Plum et al. (2011); Prosvirnin and Zheludev (2005)], and thus any chiral response distills the interaction between plasmonic structures. Optical chirality is expected when the lines of mirror symmetry of the nanostructures do not coincide with the lattice array —the mirror image cannot be superimposed with the original. “Meta-optical chirality” refers to the macroscopic optical chirality that is both observed in the far-field and attributed to the interactions between plasmonic resonators. While many have alluded to the coupling between meta-atoms, few have addressed the origin of the interaction force.

Experimentally, we employ a simple Babinet-inverted rod (dimensions  $\approx \lambda/5$ ) as the meta-atom of our metasurface and arrange the nanorods in a square array. When rod-shaped nanoapertures are tilted at an angle of  $22.5^\circ$  and illuminated with low-intensity visible light ( $\ll 1W/cm^2$ ), we measure CD on the order of 0.6 degrees of ellipticity. In comparison, while optimized and twisted split ring resonators can reach CD up to 16 degrees in the near infrared [Decker et al. (2010)], such meta-atoms require small features ( $\approx \lambda/20$ ). The relatively-large dimensions of the rod nanoapertures support dipolar plasmon resonances and can be fabricated easily with robust large-area processes. Herein we demonstrate an approach that leverages the interactions between simpler meta-atoms in order to achieve an optical chirality. The general approach boasts facile design, circumvents the complex structures that intrinsically chiral materials generally require, and forgoes the oblique illumination angle-of-incidence that is the crux of extrinsically chiral materials.

The chiral response exhibited by our metasurface is both appreciable and unexpected since plasmonic interactions generally manifest as nonlinear optical responses, which require high illumination intensities [Metzger et al. (2012); Kauranen and Zayats (2012)]; here we observe optical chirality at intensities far below those generally required to yield nonlinear optical responses. We interrogate the metasurface with a continuum of polarization states and find that we cannot characterize the metasurface simply from its response

from orthogonal circular-polarization modes. In fact, we find that a conventional transmission matrix description of the polarization properties is insufficient to accurately describe the optical behavior of the metasurface. An alternative analytic representation is provided and supports a description of intensity-independent, weakly-nonlinear plasmonic limit cycles. The model also explains why we observe the emergence of multiple eigen-polarization modes, which we also measure experimentally. This work furthers our understanding of metasurface design and breaks from the long-standing convention of transmission matrices.

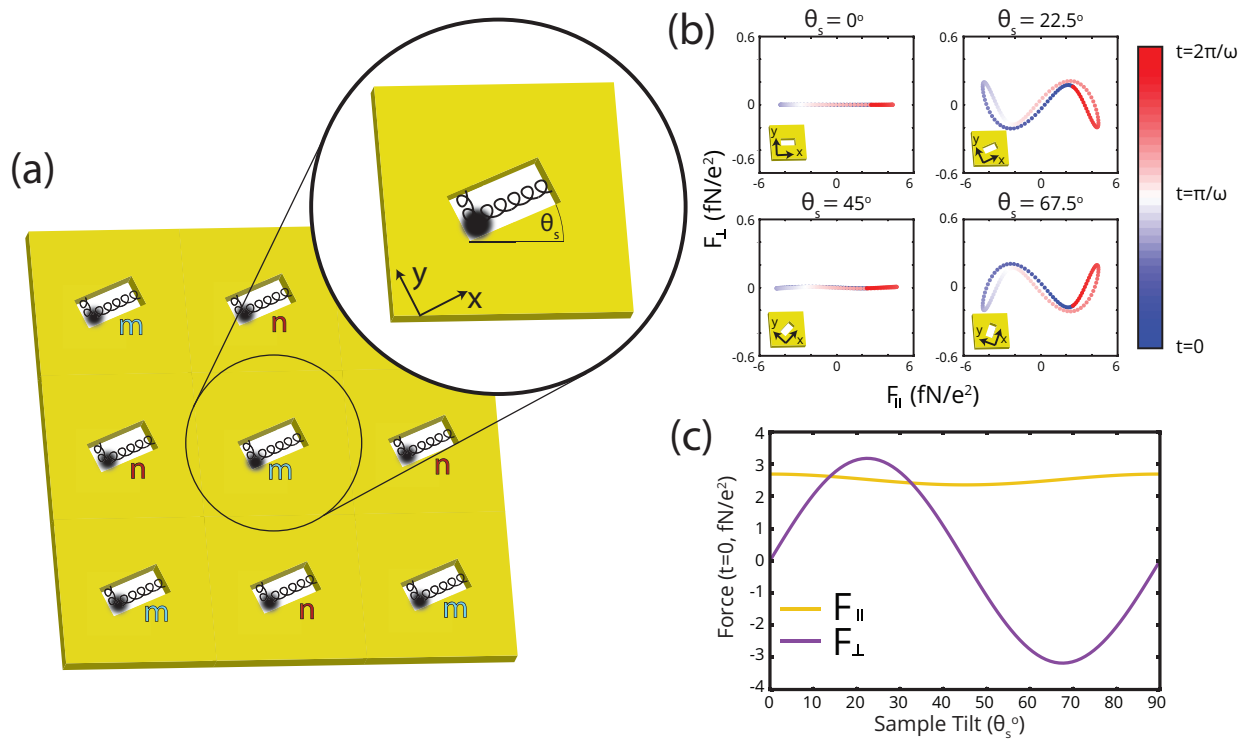


Figure 4.1: (a) Model representation: an array of plasmonic resonators (rod-shaped apertures) tilted at  $\theta_s$  relative to the base of the unit meta-atom where we separate the resonators into *m*- and *n*-type. The interaction force on *m*-type resonators results from the 4 nearest *n*-type resonators and vice-versa. (b) The interaction Lorentz force that arises from Larmor radiation [Eq. 4.1] for various  $\theta_s$  when resonators oscillate in the *x*-direction, as a function of time. (c) The interaction force in the parallel (*x*), and perpendicular (*y*) directions when the resonators oscillate in the *x*-direction, as a function of  $\theta_s$ .

## 4.2 The coupling force

In our model, we define the interaction between neighboring plasmonic resonators as the Lorentz force produced from the oscillation of adjacent resonators. The interaction force is derived from the electromagnetic field of an accelerating charged particle given by the Liénard-Wiechert potential [Jackson (1999)]. The force from an  $m^{th}$  charge on the  $n^{th}$ ,  $\vec{F}_{mn}^{int}$ , is:

$$\vec{F}_{mn}^{int} = k_e q_n q_m \left( \frac{\hat{\boldsymbol{\nu}}_{mn} - \vec{\beta}_n}{(1 - \vec{\beta}_n \cdot \hat{\boldsymbol{\nu}}_{mn})^3 R_{mn}^2} \right) + \frac{k_e q_n q_m}{c} \left( \frac{\hat{\boldsymbol{\nu}}_{mn} \times [(\hat{\boldsymbol{\nu}}_{mn} - \vec{\beta}_n) \times \dot{\vec{\beta}}_n]}{(1 - \vec{\beta}_n \cdot \hat{\boldsymbol{\nu}}_{mn})^3 R_{mn}} \right) \quad (4.1)$$

where  $k_e$  is Coulomb's constant =  $1/4\pi\epsilon_0$ ,  $\epsilon_0$  is the permittivity of free space,  $\vec{\beta}_n = \dot{\vec{r}}_n/c$ ,  $c$  is the speed of light,  $\hat{\boldsymbol{\nu}}_{mn} = \frac{\vec{r}_m - \vec{r}_n}{|\vec{r}_m - \vec{r}_n|}$  is the unit direction from the  $m^{th}$  charge to the  $n^{th}$ ,  $R_{mn}$  is the lattice distance,  $q_n$  is the charge of the  $n^{th}$  particle, and  $\vec{r}_m, \vec{r}_n$  are the positions of the  $m^{th}$ , and  $n^{th}$  resonator, respectively, from the origin. When the charges are stationary, Eq. 4.1 collapses to the Coulomb force between two charged particles. The first term of Eq. 4.1 is referred to as the “velocity field” since it is independent of acceleration, and the second term is the “acceleration field”. With motion of the charges restricted to the 2-D plane of the metasurface, the interaction forces created by the surrounding resonators are produced in the plane of the metasurface. Though charges also oscillate in the  $z$ -direction, an investigation into the coupled behavior of the longitudinal fields is beyond the scope of this study. The associated Lorentz forces may explain the near-to-far-field coupling [Vuong et al. (2010)].

A representation of the model is shown in Fig. 4.1(a), in which we tilt all nanostructures by  $\theta_s$  relative to the base of the unit cell. The tilt effectively restricts the direction of motion of the resonator and we incorporate the interaction force into the equations of motion for a Lorentz-Drude plasmonic resonator [Rakic et al. (1998)]. We model metasurfaces in which

there is no spatial variation of the unit cell, *i.e.*, all nanoapertures are tilted at the angle,  $\theta_s$ . For analytical reasons the  $x$  and  $y$ -axes also rotate by  $\theta_s$  such that the long (short)-axis of the plasmonic resonator is always parallel with the  $x$  ( $y$ )-axis. The  $\theta_s$  determines the directions of  $\vec{\beta}_m$ , and  $\vec{\nu}_{mn}$  in Eq. 4.1. We place the resonators in a checkerboard-like pattern of  $m$ - and  $n$ -type oscillations, and calculate the motion of each set of resonators. The second-order terms cancel by symmetry, and subsequently the interaction force between resonators scales inversely with the distance cubed. The four closest resonators provide the interaction force that couple motion in the  $x$ - and  $y$ -directions, and between  $m$ - and  $n$ -type resonators. Interaction forces from diagonal dipoles are between like-type resonators ( $m$ - $m$ ,  $n$ - $n$ ) and are neglected, in part because the increased distance between resonators reduces the interaction force, and also because we focus on the interactions between  $m$ - and  $n$ -type.

The total interaction force from the Larmor radiation of the four closest resonators is shown in Fig. 4.1(b-c), where  $\beta = -i\omega x_0/c\hat{i}$  and  $x_0$  is the maximum displacement of the charge oscillation, where we let  $x_0 = 20\text{nm}$ . Each resonator oscillates in the  $x$ -direction and produces a force in both parallel ( $x$ ) and perpendicular ( $y$ ) directions,  $F_{\parallel}$  and  $F_{\perp}$ . We calculate that  $F_{\parallel}$  is approximately 20 times larger than  $F_{\perp}$ . The  $F_{\parallel}$  —which is always co-aligned with the long axis of the nanostructures—is maximal when the nanostructures are oriented at  $0^\circ$  or  $90^\circ$  with the edge of the unit cell.  $F_{\parallel}$  couples the parallel motion between adjacent resonators in the formation of hybrid modes, which we document in the next section. When the angle of the nanostructure,  $\theta_s$ , is  $0^\circ$ ,  $45^\circ$ , or  $90^\circ$ ,  $F_{\perp}$  is zero, as shown in Fig. 4.1(b-c). These angles correspond to the lines of symmetry of the square lattice; the array is not intrinsically chiral. Alternatively, the magnitude of  $F_{\perp}$  is maximized at  $22.5^\circ$ , and  $67.5^\circ$  which would correspond to opposite-handed chiral structures.  $F_{\perp}$  couples to the orthogonal dipole moment of the adjacent resonators and is the source of optical chirality in our metasurface, which is further documented in the following section. Though our model

incorporates the Liénard-Wiechert potential from rectangular nanostructures, the model can be generalized to model the interaction forces from arbitrary plasmonic shapes and arrays.

### 4.3 Coupled equations of motion

We sum the interaction force [Eq. 4.1] from the four neighboring resonators to the Lorentz-Drude model and incorporate its interaction as a perturbation with the parameter,  $\delta$ :  $M\ddot{\vec{r}}_{m/n} = -M\omega_0^2\vec{r}_{m/n} - M\gamma\dot{\vec{r}}_{m/n} + q\vec{E}e^{-i\omega t} + \delta\sum_{n/m}\vec{F}_{mn}^{int}$ , where  $r$  is the displacement of the resonator from its equilibrium position,  $M$  is its mass,  $\omega_0$  is the natural harmonic frequency of the resonator,  $q$  is its charge,  $\gamma$  is the velocity-dependent damping rate,  $E_0$  is the strength of the incident driving electric field, with frequency  $\omega$ , subscript  $m/n$  refers to the motion of either  $m$ - or  $n$ -type resonators, and dot formalism corresponds to derivatives with respect to time,  $t$ . We adopt a separate solution for the displacement of the  $m$ - and  $n$ -type resonators shown below:

$$x/y(t) = \frac{E_{x/y}q/M}{\omega_{0x/y}^2 - i\gamma\omega - \omega^2}e^{-i\omega t} + \underbrace{x_h/y_h(t)}_{\text{homogeneous solution}} + \underbrace{\delta x_1/\delta y_1(t)}_{\text{perturbed solution}}, \quad (4.2)$$

which includes a homogeneous solution,  $x_h, y_h$ , often neglected [Metzger et al. (2016, 2012); Rakic et al. (1998)]. The homogeneous solution is the general solution to the equations of motion in the absence of an external electric field and its solution is determined from the initial conditions. Even though the homogeneous solution is neglected in Optics texts, it is generally present in studies of vibrations and when solving for the limit cycles of weakly nonlinear oscillators [Strogatz (1994)]. No exact analytical solution exists for the system in which the interaction force is included; our quantitative perturbative approach employs

a Taylor expansion of the interaction force,

$$\vec{F}_{mn}^{int} \approx \frac{k_e q_n q_m}{R_{mn}} \left[ \frac{(\hat{\boldsymbol{\nu}}_{mn} - \vec{\beta}_n)}{R_{mn}} + \left( \hat{\boldsymbol{\nu}}_{mn} \times [(\hat{\boldsymbol{\nu}}_{mn} - \vec{\beta}_n) \times \dot{\vec{\beta}}_n] \right) \frac{1}{c} \right] \\ \times \left( 1 + 3\vec{\beta}_n \cdot \hat{\boldsymbol{\nu}}_{mn} - 6(\vec{\beta}_n \cdot \hat{\boldsymbol{\nu}}_{mn})^2 - 10(\vec{\beta}_n \cdot \hat{\boldsymbol{\nu}}_{mn})^3 \right). \quad (4.3)$$

We consider the low-power case where the transmitted polarization is independent of illumination intensity and we linearize the interaction force with the electric field. The system remains nonlinear because the optical response cannot be described by a superposition of incident fields.

$$\begin{bmatrix} \ddot{x}_{1,m} \\ \ddot{y}_{1,m} \end{bmatrix} + \begin{bmatrix} \omega_{0x}^2 & 0 \\ 0 & \omega_{0y}^2 \end{bmatrix} \begin{bmatrix} x_{1,m} \\ y_{1,m} \end{bmatrix} + \gamma \begin{bmatrix} \dot{x}_{1,m} \\ \dot{y}_{1,m} \end{bmatrix} = \frac{1}{M} q_m \underbrace{\begin{bmatrix} \kappa_{1x,n} & \kappa_{3x,n} \\ \kappa_{3y,n} & \kappa_{1y,n} \end{bmatrix} \begin{bmatrix} E_x \\ E_y \end{bmatrix}}_{F^{int}}, \\ \begin{bmatrix} \ddot{x}_{1,n} \\ \ddot{y}_{1,n} \end{bmatrix} + \begin{bmatrix} \omega_{0x}^2 & 0 \\ 0 & \omega_{0y}^2 \end{bmatrix} \begin{bmatrix} x_{1,n} \\ y_{1,n} \end{bmatrix} + \gamma \begin{bmatrix} \dot{x}_{1,n} \\ \dot{y}_{1,n} \end{bmatrix} = \frac{1}{M} q_n \underbrace{\begin{bmatrix} \kappa_{1x,m} & \kappa_{3x,m} \\ \kappa_{3y,m} & \kappa_{1y,m} \end{bmatrix} \begin{bmatrix} E_x \\ E_y \end{bmatrix}}_{F^{int}}, \quad (4.4)$$

where

$$\kappa_{1x} = A_x \left[ 3ka + 2i + 6 + 3k^2 \left( -\langle x_h \rangle^2 (3ka \cos(4\theta_s) + A) + \langle y_h \rangle^2 (9ka \cos(4\theta_s) + A) + \langle x_h y_h \rangle 9ka \sin(4\theta_s) \right) \right], \quad (4.5)$$

$$\kappa_{1y} = A_y \left[ 3ka + 2i + 6 + 3k^2 \left( \langle y_h \rangle^2 (3ka \cos(4\theta_s) + A) + \langle x_h \rangle^2 (9ka \cos(4\theta_s) + A) - \langle x_h y_h \rangle 9ka \sin(4\theta_s) \right) \right], \quad (4.6)$$

$$\kappa_{3x} = 3A_x k^2 \left[ 3ka \sin(4\theta_s) (3\langle x_h \rangle^2 - \langle y_h \rangle^2) - 3\langle x_h y_h \rangle (9ka \cos(4\theta_s) + A) \right], \quad (4.7)$$

$$\kappa_{3y} = 3A_y k^2 \left[ -3ka \sin(4\theta_s) (3\langle y_h \rangle^2 - \langle x_h \rangle^2) - 3\langle x_h y_h \rangle (9ka \cos(4\theta_s) + A) \right], \quad (4.8)$$

and where  $A_x = \frac{2k_e q_m q_n k}{Ma^2} g_x$ ,  $A_y = \frac{2k_e q_m q_n k}{Ma^2} g_y$ ,  $A = 3ka + 4i$ ,  $a$  is the periodicity of the metasurface,  $k$  is the incident wavevector,  $\langle \rangle$  denotes the time-average, and  $g_{x/y} = \frac{1}{\omega_{0x/y}^2 - i\gamma\omega - \omega^2}$ .

While Eq. 4.4 may resemble a transmission-matrix formalism, the equations of motion of one type of resonator are coupled to the other by its homogeneous solution and subsequently, there are four coupled equations of motion instead of two. When the  $m$ -type resonators are excited, they generate Lorentz forces via the Liénard-Wiechert potential, which contribute to both parallel and perpendicular motions of the  $n$ -type resonators.

The perpendicular Lorentz force couples to the orthogonal modes of the different resonators, which leads to optical chirality in the metasurface. In order to understand the terms of Eq. 4.8, we isolate the case where the plasmonic resonators move in either the  $x$ - or  $y$ -directions in the fundamental solution. The perturbative interaction becomes  $\kappa_{3x/y} = \pm \frac{9k_e q_m q_n 2k^4}{Ma} g_{x/y} \langle y_h/x_h \rangle^2 \sin(4\theta_s)$ , which is zero when  $\theta_s = 0^\circ, 45^\circ, 90^\circ$ , etc., in agreement with the exact evaluation of  $F^{int}$  [Fig. 4.1(b-c)]. Maximal optical chirality is achieved when the nanostructures are tilted at  $\theta_s = 22.5^\circ$  and  $67.5^\circ$ .

## 4.4 Mode hybridization and optical chirality

Experimentally, we fabricate a metasurface that maximizes  $F_\perp$  or  $\kappa_{3x/y}$  with  $\theta_s = 22.5^\circ$ , in which rod nanoapertures are arranged on a 30-nm gold film and measure 160nm by 80nm, as shown in Fig. 4.2(a). The periodicity,  $a$ , varies the relative strength of the interaction force. We utilize a periodicity of 375nm in a square array, which is small enough to observe the coupling between nanoapertures, yet large enough so that the individual responses are

still present.

The wavelength-dependent transmission properties are explored in Fig. 4.2(b), which shows the transmission for linearly-polarized light. The axis of the illuminating linear polarization is rotated counter-clockwise from  $0^\circ$  (vertical) through  $90^\circ$  (horizontal) to  $180^\circ$  (vertical). We observe two absorption dips in the transmission around 600nm and 730nm

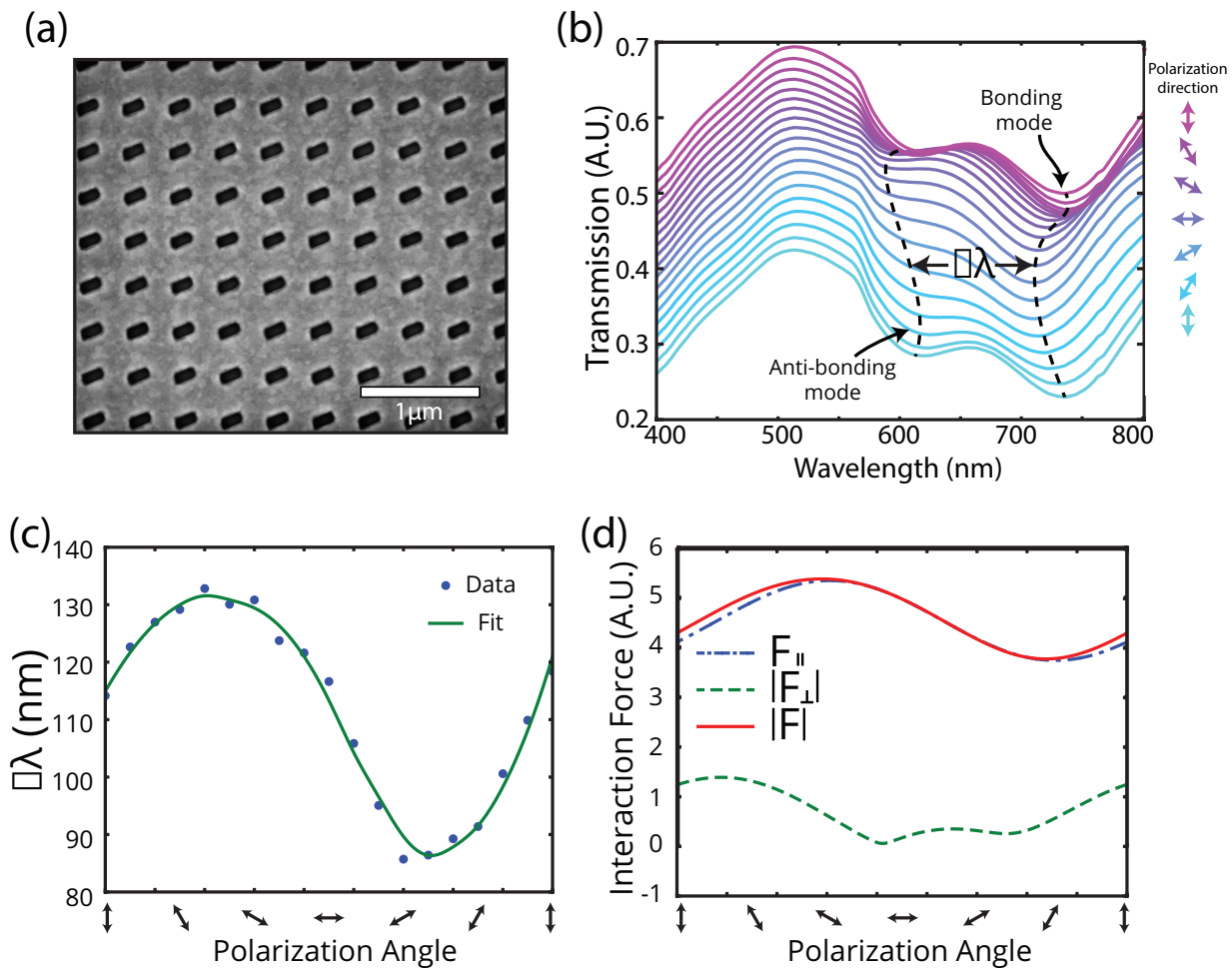


Figure 4.2: (a) A top-view scanning electron microscope image of the metasurface. (b) The transmission spectra associated with different linear polarization angles, where we observe the presence of bonding and anti-bonding modes. (c) Shift in the wavelengths of the bonding and anti-bonding modes as a function of polarization angle. (d) Interaction forces parallel and perpendicular to the polarization axis experienced by the resonators from Eq. 4.4 as a function of polarization angle.

that correspond to the mode-splitting or mode hybridization of the plasmonic dipolar resonance [Prodan et al. (2003)]. The spectral locations of the bonding and anti-bonding modes correspond to the mode coupling or interaction force  $F^{int}$ . When the periodicity decreases,  $F^{int}$  increases and the resonances separate further; if the separation between meta-atoms increases, then the transmission resonances collapse to the transmission profile of a single resonator [Prodan et al. (2003)]. The trends associated with meta-atom spacing indicate that the transmission dips observed are not a Wood's anomaly grating effect, which is related to lattice absorption. Wood's anomaly resonances would scale in proportion with the metasurface spacing. Moreover, Wood's anomalies are characterized by ultrasharp resonances [Yang et al. (2016)] which are not observed.

The parallel component of the interaction force leads to the mode-splitting in the metasurface. The spectral difference between the bonding and anti-bonding modes is shown in Fig. 4.2(c) with a Savitzky-Golay filter [Savitzky and Golay (1964)] overlaid. We evaluate

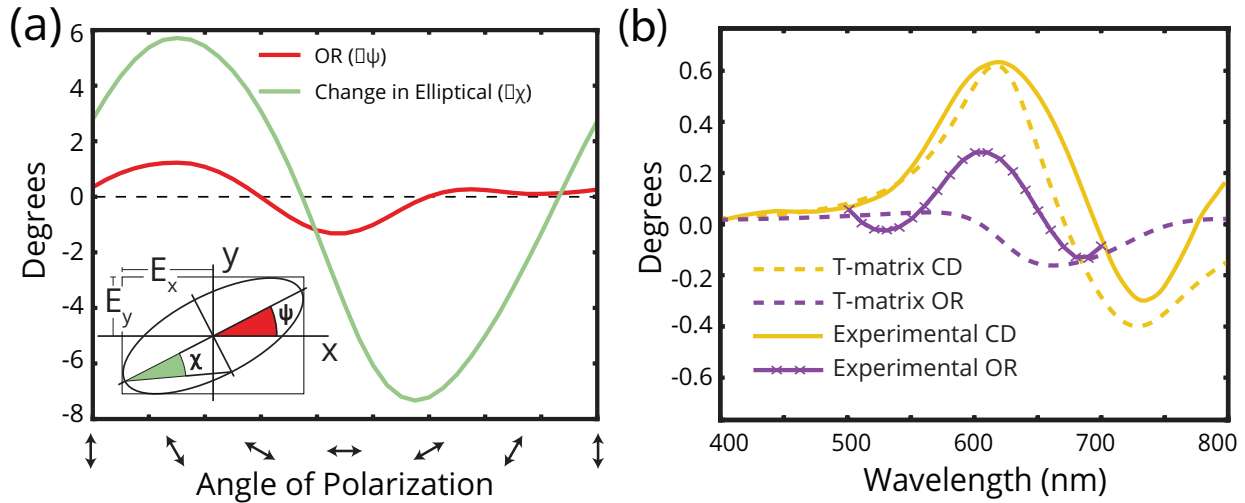


Figure 4.3: (a) The optical rotation (OR) and change in the elliptical component as a function of input polarization at 660nm. Inset: the relationship between  $E_x$  and  $E_y$  OR and change in the elliptical on the polarization ellipse. (b) OR and circular dichroism (CD) calculated from a transmission (T-)matrix approach (dashed). Overlaid is the experimental measurements of OR (measured at  $\psi = +30^\circ$ ), and the CD (solid).

the interaction force in our approximation [Eq. 4.4] in order to relate our model to the mode splitting. The components of the interaction force,  $F_{\perp}$ ,  $F_{\parallel}$ , and  $|F| = \sqrt{F_{\perp}^2 + F_{\parallel}^2}$  are shown in Fig. 4.2(d), where the input polarization is rotated from  $0^\circ$  to  $180^\circ$ . The  $F_{\parallel}$  and the trendline of the spectral shift both exhibit maximal values between  $45^\circ$  and  $55^\circ$ , where the illuminating linear polarization connects opposite ends of vertically-adjacent resonators. The minimal values of the spectral splitting occur between  $135^\circ$  and  $145^\circ$  and correspond with an angle where the illuminating linear polarization connects opposite ends of horizontally-adjacent resonators. Differences between our model and experiment result from the fact that in our model, we only consider the resonator displacement of 20nm whereas in experiment, the effective resonator dipole is the length of the nanorod, or 180nm. Moreover, our approximation of  $F^{int}$  only accounts for the four nearest resonators and incorporates only time-harmonic terms. Nevertheless, the strength of the parallel force  $F_{\parallel}$  scales approximately with the experimentally-measured spectral splitting of transmission resonances.

The interaction force leads to other experimentally-measured polarization-dependent metasurface responses. We illuminate the metasurface with linearly-polarized light (ellipticity  $\chi < 1^\circ$ ) at a wavelength  $\lambda = 660\text{nm}$  and observe that the transmitted changes in the azimuthal and elliptical components of the fields,  $\Delta\psi$  and  $\Delta\chi$ , depend on the angle of linear polarization [Fig. 4.3(a)]. The change in azimuth  $\Delta\psi$  denotes optical rotation (OR) and the change in the elliptical component  $\Delta\chi$  denotes the phase accumulation between the  $E_x$  and  $E_y$ -components. When the illuminating polarization angle rotates a full revolution, the trendline for the OR exhibits 4 inflection points. The OR and the perpendicular interaction force  $F_{\perp}$  follow a similar trend [Fig. 4.2(d)], which is expected since  $F_{\perp}$  is the source of the optical chirality in our metasurface.

Optical chirality is conventionally determined by the off-diagonal elements of transmis-

sion matrix of the metasurface [Wu et al. (2016); Plum et al. (2016, 2011)] but there are limits to this transmission matrix formalism. The polarization density of the material is calculated with the relation  $\vec{P} = N_0q\vec{r}$ , where  $N_0$  is the free charge carrier concentration of the material,  $q$  is the charge of the particles, and  $\vec{r}$  is the direction and subsequently:

$$\vec{P} = N_0q \begin{bmatrix} x_0 + x_1 \\ y_0 + y_1 \end{bmatrix} = \epsilon_0(\epsilon - 1)\vec{E}(\omega, r) + \Gamma(\nabla \times \vec{E}(\omega, r)), \text{ and the non-locality parameter, } \Gamma_{x/y} = \frac{iN_0q_m q_n \kappa_{3x/y}}{k(\omega_{0x/y}^2 - i\gamma\omega - \omega^2)}, \text{ and } \Gamma \text{ is the mean of } \Gamma_x \text{ and } \Gamma_y.$$

The relations for OR =  $\frac{\omega}{2c}\Re(\Gamma)$ , and CD =  $\frac{2\omega}{c}\Im(\Gamma)$ , are shown as a function of the incident wavelength for tilt angle of  $\theta_s = 22.5^\circ$  in Fig 4.3(b) and the experimental observation is overlaid. The CD is defined as the differential circular-polarization absorption as  $CD(^o) = (T_{RCP} - T_{LCP}) \times 32.982^\circ$  in degrees of ellipticity [Barron (2009)]. The experimental results for CD qualitatively agree well with the analytical theory for the CD, where peaks in CD are present at both dipolar modes. In a transmission-matrix calculation, there is less agreement between the real component of  $\Gamma$  and the experimentally-measured OR. We expect that CD may be more accurately modeled with transmission matrices because the rotating circular polarization averages all linear-polarization responses, and reduces the polarization-dependence illustrated in Fig. 4.2. The discrepancies between theoretical and experimental OR indicate the limit of the transmission matrix formalism that assumes that all resonators oscillate in-phase, which may not be true when an interaction force is present between meta-atoms.

## 4.5 Emergent polarization eigenmodes

We interrogate the metasurface with a continuum of polarization states and observe polarization-dependent responses other than OR that cannot be recreated by transmission matrices. We characterize the properties of the metasurface eigen-polarization modes at a wavelength of 660nm on the Poincaré sphere [Fig. 4.4(a)]. Figure 4.4(b) shows the eigen-polarization

modes mapped onto the  $x - y$  plane, where the wave travels in the  $z$ -direction. The eigen-polarization modes of the system are interpreted as eigenmodes of the coupled equations of motion of the system.

We measure six eigen-polarization modes of the metasurface, where a standard transmission matrix approach asserts the existence of only two [Gevorgyan and Rafayelyan (2013)]. Two of the six eigen-polarization modes are approximately linearly-polarized, and the remaining four are elliptically-polarized. The presence of the multiple eigen-polarization modes cannot be characterized by the conventional, single transmission matrix formulation —which assumes that adjacent resonators are excited in phase —and supports an alternative model of coupled resonators.

There is potentially a misconception that transmission matrices should describe any metasurface optical response that is independent of the illumination intensity. The optical response from our metasurface is linear because the transmitted polarization does not change with illumination intensity and would not produce the prototypical nonlinear optical response, for example, higher-harmonic generation, particularly at low illumination intensity.

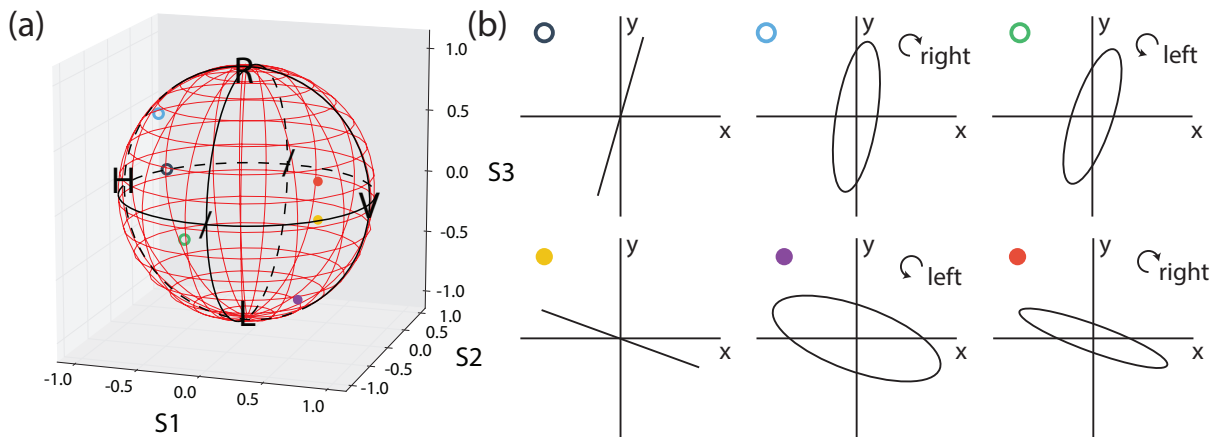


Figure 4.4: Eigen-polarization modes of the system at 660nm are shown on (a), the Poincaré sphere, where solid circles represent eigen-polarization states on the near surface of the sphere and hollow circles represent states on the far surface. (b) illustrates the eigen-polarization states measured in the  $x - y$  plane.

tion intensities. At the same time, the transmitted polarization from our metasurface is nonlinear in a manner that the optical response cannot be described by a superposition of incident fields. It appears insufficient to characterize the polarization properties of the metasurface by deriving a transmission matrix from the optical response of select linear or orthogonal circular polarizations. The corresponding system of equations in our model predicts multiple polarization eigenmodes that are observed at visible wavelengths and at low illumination power, independent of illumination intensity.

## 4.6 Discussion

The inclusion of an interaction force leads to responses that are not predicted via transmission matrices, such as polarization-dependent OR or multiple eigen-polarization modes, which we measure in this investigation. Discrepancies from a transmission matrix formalism may be minimal when the interaction force is small and when meta-atoms are separated significantly far apart [Haus (2014)]. However, initial calculations suggest that the Larmor radiation from adjacent meta-atoms achieves intensities comparable to that of the incident electric field, even at low illumination intensities, due to the strong acceleration of charges on sub-wavelength nanostructures at visible wavelengths. Moreover, the constructive interference of Larmor fields in periodic lattice structures such as metasurfaces is measurable. The Larmor radiation field may be engineered to produce a desired electromagnetic response. One method to increase the Larmor radiation, and thus the optical chirality, is to reduce the periodicity of the nanostructures since the interaction force [Eq. 4.1] scales with the inverse distance between resonators. However, as Lee and Park (2016) showed, the dependence on periodicity does not continue to increase the interactions forces indefinitely since at the limit of zero periodicity we expect the scattering cross section of the array of coupled plasmonic resonators to reduce to that of a single resonator. In order to satisfy

this condition, a screening factor of  $S = 1 - e^{-\sqrt{2/3}ka}$  is employed so that the interaction forces converge to zero at zero periodicity.

## 4.7 Conclusion

In conclusion we have proposed a facile design approach to achieve optical chirality at normal incidence in planar arrays of achiral nanoapertures that leverages the interaction force between coupled resonators. Optical chirality results from perpendicular Lorentz forces associated with the Liénard-Wiechert potentials when plasmonic resonators are sufficiently close. Bonding/anti-bonding modes observed in the transmission spectra result from the parallel components of the interaction forces. We have studied the polarization properties and demonstrated that our metasurface exhibits both OR and CD equivalent responses at normal incidence in the visible regime, a property found only in chiral materials. The OR depends on the incident angle of polarization and cannot be fully described by transmission matrices. We further demonstrate this principle through the measurements of several eigen-polarization modes. The presence of appreciable optical chirality in our metasurface indicate Larmor radiation plays a significant role in the polarization properties of metasurfaces.

## 4.8 Fabrication Methods and Measurement

The device can be fabricated by depositing a nanopatterned gold layer onto an ohmic conductor. The gold layer can be deposited onto the ohmic contact via thermal deposition which can give accurate layer thicknesses. Layer thicknesses are determined using a Filmetrics spectral reflectance analyzer. A calibration layer is first deposited on a substrate to correctly determine the rate of deposition for particular equipment settings. Once the

rate of the metal are determined, the layer can be deposited, and the layer thicknesses determined using the spectral reflectance analyzer. Following, a layer of high resolution positive electron beam resist, ZEP-520A, is spin-coated on the gold layer. ZEP-520A is required to show the sharp definitions and high resolution that the nanostructure design demands. The nanostructure is patterned into the ZEP-520A resist using electron beam lithography, using ion beam milling the patterned resist is removed and gold where the resist was etched away. This process can be done to leave either gold nanostructures or a gold film with nanoapertures.

The patterns are created in Adobe Illustrator since the dimensions of the objects can be accurately inputted. Adobe Illustrator also has the feature of exporting to DXF and DWG files. These files are compatible with the BEAMER software that is provided at Brookhaven National Lab to create the patterns compatible with the electron beam lithography machine.

### 4.8.1 Development

#### Electron beam resist

The electron beam resist used was ZEP-520A, the resist thicknesses as a function of spin speed and dilution has been studied elsewhere [Bojko (2013)], the thickness data is given as follows in Fig. 4.5. ZEP-520A has the properties of showing very high resolution, a rectangle pattern profile, and high sensitivity. This is important for this work since the structures that will fabricated are on the order of  $10^{-8}m(10nm)$ , and thus the electron beam resist needs to show the greatest contrast for the nanostuctures to be well defined and have the desired optical properties.

Another common electron beam resist that was considered is PMMA. PMMA is the most common electron beam resist used since it offers high resolution, is easy to handle and film

characteristics have been well-studied. Though, like ZEP-520A, PMMA also provides high resolution it exhibits low contrast, which could lead to undesired optical properties.

Characteristics of ZEP-520A, are that it has a positive tone, resolution of at least 20nm, has a dry etch resistance similar to many photo resists. The film life, however is relatively short compared to other electron-beam resists such as PMMA.

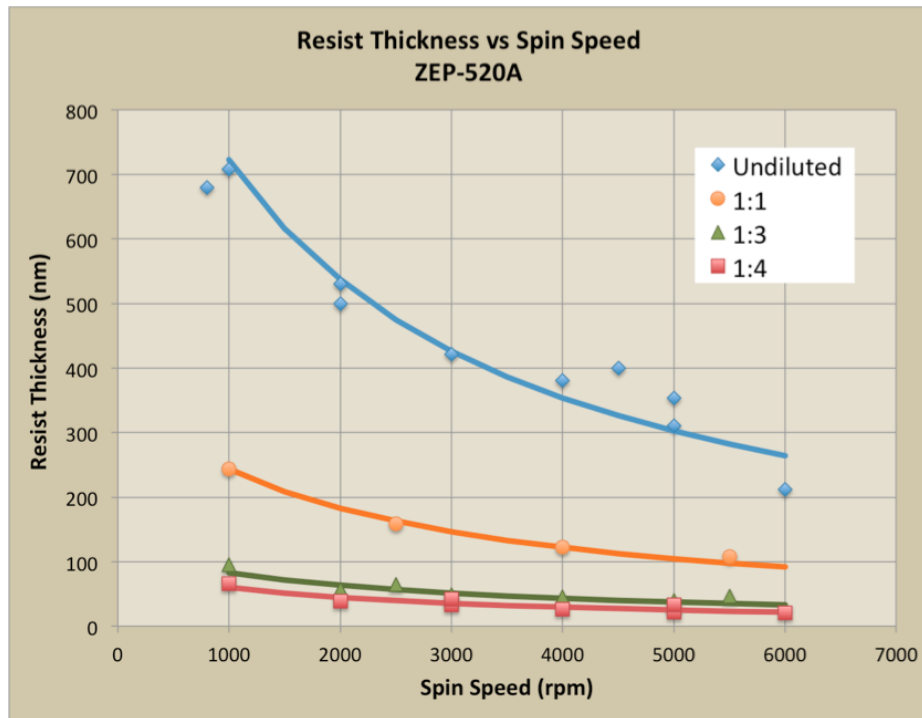


Figure 4.5: Spin curve for ZEP-520A.

Image: <https://ebeam.mff.uw.edu/ebeamweb/process/process/zep520a.html>

## Fracturing

The shot pitch of the electron beam lithography machine is set to 0.125nm. Since at some points of the structure the shot pitch is not exactly divisible by the shape size, the dimensions of the shape produced may be slightly off (by a maximum of one shot pitch) To solve this problem shot pitch fracturing is enabled, such that some extra pixels are overlapped and the correct dimensions specified are achieved [BEA (2010)]. This is

important in fabricating the structures since they have very small feature sizes. Plasmonic effects are highly sensitive to structure dimensions, thus, shot pitch fracture is necessary to retain the specific dimensions of the nanostructures, and by relation the plasmonic response is preserved.

### Proximity effect correction

From looking at SEM images of the 2D nanostructures it is clear that the shapes do not have as sharp corners as originally intended. The reason for this is due to scattering of the electron beam in the resist and substrate leading to undesired resist etching in the proximity of the beam, known as the proximity effect [Owen and Rissman (1983)]. Though the individual shapes are the same size the edges of nanostructures are likely to experience the proximity effect.

One way to use proximity effect correction is via dose modulation, in which each individual shape in a pattern is given a dose such that the shape prints the correct size. Generally, the proximity effect can be thought of as larger-patterned areas receive larger doses due to the electron scattering. To compensate the larger areas receive slightly lower dosages, or alternatively, the smaller areas receive slightly higher dosages.

Another method to resolve the proximity effect is via pattern biasing. In this method the larger dose that greater area patterns receive from the proximity effect is compensated by making the area either smaller or less dense.

Practically it is easier to implement the second method on the electron beam lithography machine, as it keeps the dosage the same throughout the writing of the pattern, only varying the pattern itself.

## Developers

There are a number of different developers available for use. Xylenes is a common developer since the dosage needed is low, so patterns can be written faster, however the contrast is generally low. Amyl-acetate has a higher contrast, and hexyl-acetate has the highest contrast, though the higher the contrast, the higher dosage generally needed to write the pattern and develop effectively. Better yet is to use hexyl-acetate at low temperature.

### 4.8.2 Recipe

The recipe of rod-shaped nanoapertures is as follows: First on a glass substrate a 3-nm wetting layer of chromium was deposited, followed by a 30-nm layer of gold with an electron beam evaporator. The thicknesses of the layers were accurately measured via a Filmetrics F20-UV thin film analyzer that is available both at Brookhaven national lab and at the Vuong lab. From an initial test sample the rates of the electron beam evaporator were accurately determined to produce reliable film thicknesses. The rates of chromium and gold were deposited at a rate of  $0.4\text{\AA}$  per second to produce film with high uniformity and low surface roughness(<2nm).

Next a layer of ZEP 520a is spin-coated onto the sample. The thickness of which is determined by the thickness of gold and the ion-milling rates of both gold and ZEP 520a. Since the desired result is a gold film with rod-shaped apertures that propagate the entire thickness of the film, once the pattern is written on the resist, and developed, there will be rod-shaped apertures in the resist. At the ion-milling stage, where the pattern is written gold is exposed to the ion miller and will be milled away, everywhere else only the resist is exposed to the ion miller and will be milled. Ideally, as the resist is milled away, and the gold is milled away where the pattern is written, once the entire layer of resist is completely

milled away, so is the gold, where the pattern is written. Therefore the layer of resist that needs to be spin-coated is equal to:

$$L_{ZEP} = \frac{MR_{Au}}{MR_{ZEP}} \times L_{Au}, \quad (4.9)$$

where  $MR_{AU}$  is the milling rate of gold,  $MR_{ZEP}$  is the milling rate of the resist, ZEP 520a,  $L_{Au}$  is the layer thickness of gold, and  $L_{ZEP}$  is the layer thickness of ZEP 520a.

Using a two test samples of substrates with gold and spin-coated ZEP 520a, by measuring the thicknesses of the respective layers both before and after a specified time of ion-milling, the milling rates for both gold and ZEP 520a were determined to be around  $0.1\text{\AA/s}$  and  $1\text{\AA/s}$  respectively. With a gold layer thickness of 30nm, the layer of ZEP 520a that was spin-coated necessarily had to be over 300nm. In this way, in the ion milling process the layer of resist will be completely milled away at the same time that the gold will be milled away where the pattern is written.

Once the layer of resist needed is known the spin speed can be determined via the spin curve given in Fig 4.5. From here we can see that a 1:1 dilution of ZEP 520a with a spin speed around 500rpm.

Next, a  $1.5\text{mm} \times 1.5\text{mm}$  area pattern is written on the resist with the electron beam lithography machine. A via trial-and-error a dosage of  $500\mu\text{C/cm}^2$  was used. Trial-and-error was performed by setting a variety of dosages, running the pattern, developing, and inspecting under a scanning electron microscope to determine which particular dosages were under/over-exposed, and which worked best. In the same way the current of the electron beam was determined to be 250pA.

Once the pattern is written the sample was developed, hexyl-acetate was determined to be the best developer due to its high contrast especially at low temperature conditions. The

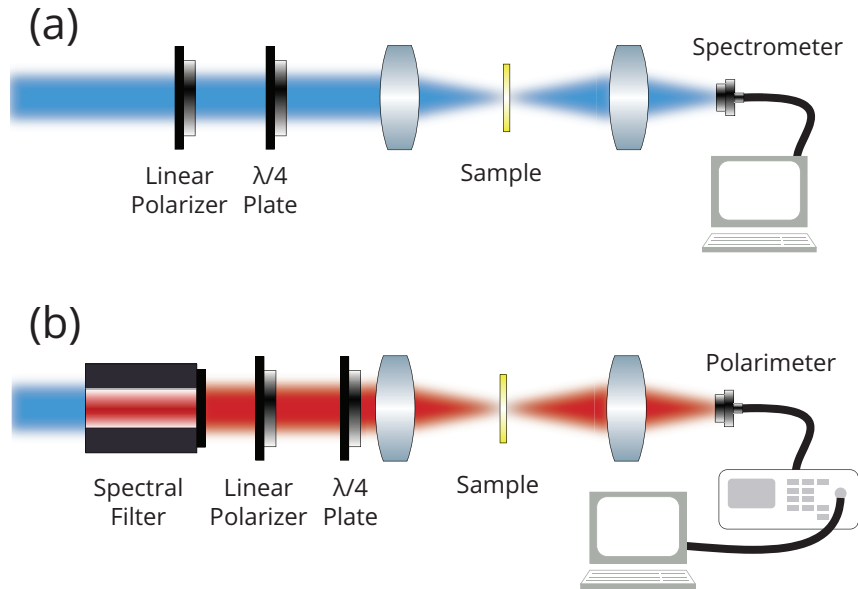


Figure 4.6: The schematic diagram for (a) transmission measurements and (b) polarization measurements.

sample was developed in hexyl-acetate at  $-25^{\circ}C$  in a propylene glycol bath for 90 seconds followed by a rinse in iso-propyl alcohol.

Finally the sample was ion-milled such that the remainder of the resist is removed. The sample was visually inspected for any resist.

Figure 4.2(a) shows a scanning electron microscope image of the metasurface from the top.

### 4.8.3 Transmission Measurement Setup

To measure the optical chirality from the metasurface we use a xenon solar simulator that provides stable broadband illumination between 400nm and 1000nm. The polarization state of light is controlled with a wire grid polarizer a 400-nm to 800-nm achromatic quarter-wave plate. The spectrum from the sample is captured via a CCD-coupled spectrometer [Fig. 4.6(a)].

#### 4.8.4 Polarization Measurement Setup

The eigen-polarization states are determined in a similar setup described above, however a spectral filter is used and the CCD-coupled spectrometer is replaced with a polarimeter to determine the polarization of transmitted light [Fig. 4.6(b)].

### 4.9 Experimental Difficulties and Future Work

It has been demonstrated that chiral phenomena exists in regular arrays of rod-shaped nanoapertures tilted at  $22.5^\circ$ . To further establish this phenomena, arrays of nanoapertures may be fabricated with varying tilt angles and periodicities. Variation of the periodicity would affect the coupling between nanostructures, and variation of the tilt angle would vary the strength of the perpendicular force generated that leads to the chiral phenomena observed.

The same effect may also be achieved with nanostructures, i.e., the non Babinet-inverted structure. The recipe for this type of metasurface was attempted however, due to the lift-off step, which can be quite difficult to perform, this type of metasurface was not pursued. The type of metasurface is fabricated in much the same manner as the one investigated, however the gold film is deposited after the electron beam lithography process. This makes the fabrication challenging as the non-conductive property of the glass substrate creates a difficult environment to perform the electron beam lithography.

Future work may also involve exploration into the optical forces that arise with the chiral phenomena, named optical rectification. Transverse Lorentz forces arise when light is illuminated on the metasurface [Proscia et al. (2016)] that are realised as a voltage which are theoretically measurable on this metasurface. Moreover due to the non-centrosymmetric pattern that the rod-shaped nanoapertures exhibit when tilted at angles such as that stud-

ied here,  $\theta_s = 22.5^\circ$ , the transverse voltages should exist even at normal incidence. These measurements typically require intense pulsed laser fields ( $>1\text{MW}/\text{cm}^2$ ) and sensitive voltage measurement instruments.

# Bibliography

- (2010). Layout BEAMER Advanced Features. [https://www.nanolithography.gatech.edu/training/Layout\\_BEAMER\\_Advanced\\_Features.pdf](https://www.nanolithography.gatech.edu/training/Layout_BEAMER_Advanced_Features.pdf).
- Ajeta, F., Genevet, P., Yu, N., Kats, M. A., Gaburro, Z., and Capasso, F. (2012). Out-of-Plane Reflection and Refraction of Light by Anisotropic Optical Antenna Metasurfaces with Phase Discontinuities. *Nano Letters*, 12(3):1702–1706.
- Allouche, J. and Shallit (2003). *Automatic Sequence: Theory, Applications, Generalizations*. Cambridge University Press.
- Arcenegui, J. J., Garcia-Sanchez, P., Morgan, H., and Ramos, A. (2013). Electro-orientation and electrorotation of metal nanowires. *Physical Review E*, 88:063018.
- Armelles, G., Cebollada, A., Garcia-martin, A., and Gonzalez, M. (2013). Magnetoplasmonics: combining magnetic and plasmonic functionalities. *Advanced Optical Materials*, 1:10–35.
- Ashkin, A. (1997). Optical trapping and manipulation of neutral particles using lasers. *Proceedings of the National Academy of Sciences*, 94(10):4853–4860.
- Ashkin, A. (2001). *History of Optical Trapping and Manipulation of Small Neutral Particles, Atoms, and Molecules*, pages 1–31. Springer Berlin Heidelberg, Berlin, Heidelberg.
- Barnes, W. and Aguie, B. (2009). Diffractive coupling in gold nanoparticle arrays and the effect of disorder. *Optics Letters*, 34:401–403.
- Barnes, W., Dereux, A., and Ebbesen, T. (2003). Surface plasmon subwavelength optics. *Nature*, 424:824–830.
- Barrera, J. F., Tebaldi, M., Amaya, D., Furlan, W. D., Monsoriu, J. A., Bolognini, N., and Torroba, R. (2012). Multiplexing of encrypted data using fractal masks. *Optics Letters*, 37(14):2895–2897.
- Barron, L. D. (2009). *Molecular Light Scattering and Optical Activity*. Cambridge University Press, New York, NY, USA, 2nd edition.

- Bashevoy, M., Fedotov, V., and Zheludev, N. (2005). Optical whirlpool on an absorbing metallic nanoparticle. *Optics Express*, 13(21):8372–8379.
- Berry, M. (1979). Diffractals. *Journal of Phys A - Mathematical and General*, 12(6):781–797.
- Beth, R. A. (1936). Mechanical detection and measurement of the angular momentum of light. *Physical Review*, 50:115–125.
- Bliokh, K. Y., Ostrovskaya, E. A., Alonso, M. A., Rodríguez-Herrera, O. G., Lara, D., and Dainty, C. (2011). Spin-to-orbital angular momentum conversion in focusing, scattering, and imaging systems. *Optics Express*, 19(27):26132–26149.
- Bojko, R. (2013). ZEP-520A Process Information. <https://ebeam.mff.uw.edu/ebeamweb/process/process/zep520a.html>.
- Bonin, K., Kourmanov, B., and Walker, T. (2002). Light torque nanocontrol, nanomotors and nanorockers. *Optics Express*, 10(19):984–989.
- Boriskina, S. V. and Reinhard, B. M. (2012). Molding the flow of light on the nanoscale: from vortex nanogears to phase-operated plasmonic machinery. *Nanoscale*, 4:76–90.
- Brandao, P. A. and Cavalcanti, S. B. (2013). Optical spin-to-orbital plasmonic angular momentum conversion in subwavelength apertures. *Optics Letters*, 38(6):920–922.
- Cao, T. and Cryan, M. J. (2012). Enhancement of circular dichroism by a planar non-chiral magnetic metamaterial. *Journal of Optics*, 14(8).
- Cao, T., Wei, C., and Mao, L. (2015a). Numerical study of achiral phase-change metamaterials for ultrafast tuning of giant circular conversion dichroism. *Scientific Reports*, 5.
- Cao, T., Wei, C.-W., Mao, L.-B., and Wang, S. (2015b). Tuning of giant 2D-chiroptical response using achiral metasurface integrated with graphene. *Optics Express*, 23(14):18620–18629.
- Cao, T., Zhang, L., Simpson, R. E., Wei, C., and Cryan, M. J. (2013). Strongly tunable circular dichroism in gammadion chiral phase-change metamaterials. *Optics Express*, 21(23):27841–27851.
- Chang, D. E., Sørensen, A. S., Hemmer, P. R., and Lukin, M. D. (2007). Strong coupling of single emitters to surface plasmons. *Physical Review B*, 76:035420.
- Chowdhury, A., Ackerson, B., and Clark, N. (1985). Laser-induced freezing. *Physical Review Letters*, 55(8):833–836.

- Chyou, J., Chu, C., Shih, Z., Lin, C., Chen, S., and Shu, F. (2005). Fabrication and metrology of an electro-optic polymer light modulator based on waveguide-coupled surface plasmon resonance. *Optical Engineering*, 44(3):034001–034001–7.
- Cortie, M. and Ford, M. (2007). A plasmon-induced current loop in gold semi-shells. *Nanotechnology*, 18(23):235704.
- Decker, M., Zhao, R., Soukoulis, C. M., Linden, S., and Wegener, M. (2010). Twisted split-ring-resonator photonic metamaterial with huge optical activity. *Optics Letters*, 35(10):1593–1595.
- Dicken, M. J., Sweatlock, L. A., Pacifici, D., Lezec, H. J., Bhattacharya, K., and Atwater, H. A. (2008). Electrooptic modulation in thin film barium titanate plasmonic interferometers. *Nano Letters*, 8(11):4048–4052.
- Dienerowitz, M., Mazilu, M., and Dholakia, K. (2008). Optical manipulation of nanopartides: a review. *Journal of Nanophotonics*, 2(1):021875–021908.
- Ding, F., Wang, Z., He, S., Shalaev, V. M., and Kildishev, A. V. (2015). Broadband high-efficiency half-wave plate: A supercell-based plasmonic metasurface approach. *ACS Nano*, 9(4):4111–4119. PMID: 25790895.
- Ditlbacher, H., Hohenau, A., Wagner, D., Kreibig, U., Rogers, M., Hofer, F., Ausseneegg, F. R., and Krenn, J. R. (2005). Silver nanowires as surface plasmon resonators. *Physical Review Letters*, 95:257403.
- Drake, J. and Genack, A. (1989). OBSERVATION OF NONCLASSICAL OPTICAL DIFFUSION. *Physical Review Letters*, 63(3):259–262.
- Du, G.-X., Saito, S., and Takahashi, M. (2011). Magnetic field effect on the localized plasmon resonance in patterned noble metal nanostructures. *IEEE Transactions on Magnetics*, 47(10):3167–3169.
- Duarte, M. F., Davenport, M. A., Wakin, M. B., Laska, J. N., Takhar, D., Kelly, K. F., and Baraniuk, R. G. (2007). Multiscale random projections for compressive classification. In *Image Processing, 2007. ICIP 2007. IEEE International Conference on*, volume 6, pages VI – 161–VI – 164.
- Edwards, B., Mayer, T. S., and Bhiladvala, R. B. (2006). Synchronous electrorotation of nanowires in fluid. *Nano letters*, 6(4):626–632.
- Eftekhari, F. and Davis, T. J. (2012). Strong chiral optical response from planar arrays of subwavelength metallic structures supporting surface plasmon resonances. *Physical Review B*, 86(7).

- Fan, J. A., Wu, C., Bao, K., Bao, J., Bardhan, R., Halas, N. J., Manoharan, V. N., Nordlander, P., Shvets, G., and Capasso, F. (2010). Self-assembled plasmonic nanoparticle clusters. *Science*, 328(5982):1135–1138.
- Fan, Z. and Govorov, A. O. (2010). Plasmonic circular dichroism of chiral metal nanoparticle assemblies. *Nano Letters*, 10(7):2580–2587. PMID: 20536209.
- Fang, Z., Zhen, Y.-R., Neumann, O., Polman, A., Garca de Abajo, F. J., Nordlander, P., and Halas, N. J. (2013). Evolution of light-induced vapor generation at a liquid-immersed metallic nanoparticle. *Nano Letters*, 13(4):1736–1742. PMID: 23517407.
- Funston, A. M., Novo, C., Davis, T. J., and Mulvaney, P. (2009). Plasmon coupling of gold nanorods at short distances and in different geometries. *Nano Letters*, 9(4):1651–1658.
- Gevorgyan, A. H. and Rafayelyan, M. S. (2013). Optics of anisotropic metamaterial based structurally chiral photonic crystals. *Journal of Optics*, 15(12):125103.
- Gonzalez-Diaz, J. B., Garcia-Martin, J. M., Garcia-Martin, A., Navas, D., Asenjo, A., Vazquez, M., Hernandez-Velez, M., and Armelles, G. (2009). Plasmon-enhanced magneto-optical activity in ferromagnetic membranes. *Applied Physics Letters*, 94(26).
- Goodman, J. W. (2005). *Introduction to Fourier optics*. Roberts and Co.
- Gu, Y. and Kornev, K. G. (2010). Plasmon enhanced direct and inverse faraday effects in non-magnetic nanocomposites. *Journal of the Optical Society of America B*, 27(11):2165–2173.
- Guerrero-Martinez, A., Lorenzo Alonso-Gomez, J., Auguie, B., Magdalena Cid, M., and Liz-Marzan, L. M. (2011). From individual to collective chirality in metal nanoparticles. *Nano Today*, 6(4):381–400.
- Hai-Dong, D., Jin, L., Wei-Ren, Z., Wei, Z., Xu-Sheng, L., Ting, S., Qiao-Feng, D., Li-Jun, W., Sheng, L., and Gopal, A. V. (2008). Enhancement of switching speed by laser-induced clustering of nanoparticles in magnetic fluids. *Applied Physics Letters*, 92(23):233103.
- Hasman, E., Biener, G., Niv, A., and V., K. (2005). Space-variant polarization manipulation. *Progress in Optics*, 47:215–289.
- Haus, H. (2014). *Waves and Fields in Optoelectronics*. Prentice Hall.
- Hentschel, M., Schaeferling, M., Weiss, T., Liu, N., and Giessen, H. (2012). Three-Dimensional Chiral Plasmonic Oligomers. *Nano Letters*, 12(5):2542–2547.
- Hertel, R. (2006). Theory of the inverse faraday effect in metals. *Journal of Magnetism and Magnetic Materials*, 303(1):L1–L4.

- Horvath, P., Smid, P., Vaskova, I., and Hrabovsky, M. (2010). Koch fractals in physical optics and their Fraunhofer diffraction patterns. *Optik*, 121(2):206–213.
- Hou, B., Xu, G., Wen, W., and Wong, G. (2004). Diffraction by an optical fractal grating. *Applied Physics Letters*, 85(25):6125–6127.
- Howland, G. A. and Howell, J. C. (2013). Efficient High-Dimensional Entanglement Imaging with a Compressive-Sensing Double-Pixel Camera. *Physical Review X*, 3(1).
- Hugel, T., Holland, N., Cattani, A., Moroder, L., Seitz, M., and Gaub, H. (2002). Single-molecule optomechanical cycle. *Science*, 296(5570):1103–1106.
- Jackson, J. D. (1999). *Classical electrodynamics*. Wiley, New York, NY, 3rd ed. edition.
- Jacquin, A. (1993). Fractal Image-Coding - A Review. *Proceedings of the IEEE*, 81(10):1451–1465.
- Jain, P. K., Eustis, S., and El-Sayed, M. A. (2006). Plasmon coupling in nanorod assemblies: optical absorption, discrete dipole approximation simulation, and exciton-coupling model. *Journal of Physical Chemistry B*, 110(37):18243–18253.
- Janhunen, P. and Sandroos, A. (2007). Simulation study of solar wind push on a charged wire: basis of solar wind electric sail propulsion. *Annales Geophysicae*, 25(3):755–767.
- Kauranen, M. and Zayats, A. V. (2012). Nonlinear plasmonics. *Nature Photonics*, 6(11):737–748.
- Kelly, K., Coronado, E., Zhao, L., and Schatz, G. (2003). The optical properties of metal nanoparticles: The influence of size, shape, and dielectric environment. *Journal of Physical Chemistry B*, 107(3):68–677.
- Keshoju, K., Xing, H., and Sun, L. (2007). Magnetic field driven nanowire rotation in suspension. *Applied Physics Letters*, 91(12):123114.
- Khanikaev, A. B., Arju, N., Fan, Z., Purtseladze, D., Lu, F., Lee, J., Sarriugarte, P., Schnell, M., Hillenbrand, R., Belkin, M. A., and Shvets, G. (2016). Experimental demonstration of the microscopic origin of circular dichroism in two-dimensional metamaterials. *Nature Communications*, 7.
- Kippenberg, T. J. and Vahala, K. J. (2007). Cavity opto-mechanics. *Optics Express*, 15(25):17172–17205.
- Knight, M. W., Grady, N. K., Bardhan, R., Hao, F., Nordlander, P., and Halas, N. J. (2007). Nanoparticle-mediated coupling of light into a nanowire. *Nano Letters*, 7(8):2346–2350. PMID: 17629348.

- Kuo, S. C. (2001). Using optics to measure biological forces and mechanics. *Traffic*, 11(2):757–763.
- Kuznetsov, A. I., Miroshnichenko, A. E., Fu, Y. H., Zhang, J., and Luk'yanchuk, B. (2012). Magnetic light. *Scientific Reports*, 2.
- Kuzyk, A., Schreiber, R., Fan, Z., Pardatscher, G., Roller, E.-M., Hoegele, A., Simmel, F. C., Govorov, A. O., and Liedl, T. (2012). DNA-based self-assembly of chiral plasmonic nanostructures with tailored optical response. *Nature*, 483(7389):311–314.
- Kwon, D.-H., Werner, P. L., and Werner, D. H. (2008). Optical planar chiral metamaterial designs for strong circular dichroism and polarization rotation. *Optics Express*, 16(16):11802–11807.
- Lal, S., Link, S., and Halas, N. J. (2007). Nano-optics from sensing to waveguiding. *Nature Photonics*, 1(11):641–648.
- Lang, M. J. and Block, S. M. (2003). Resource letter: Lbot-1: Laser-based optical tweezers. *American Journal of Physics*, 71(3):201–215.
- Lee, M. P. and Padgett, M. J. (2012). Optical tweezers: a light touch. *Journal of Microscopy*, 248(3):219–222.
- Lee, S. and Park, Q.-H. (2016). Dynamic coupling of plasmonic resonators. *Scientific Reports*, 6.
- Lehmuskero, A., Li, Y., Johansson, P., and Käll, M. (2014). Plasmonic particles set into fast orbital motion by an optical vortex beam. *Optics Express*, 22(4):4349–4356.
- Lehmuskero, A., Ogier, R., Gschneidtner, T., Johansson, P., and Kll, M. (2013). Ultrafast spinning of gold nanoparticles in water using circularly polarized light. *Nano Letters*, 13(7):3129–3134.
- Liaw, J.-W., Lo, W.-J., and Kuo, M.-K. (2014). Wavelength-dependent longitudinal polarizability of gold nanorod on optical torques. *Optics Express*, 22(9):10858–10867.
- Link, S. and El-Sayed, M. (1999). Spectral properties and relaxation dynamics of surface plasmon electronic oscillations in gold and silver nanodots and nanorods. *Journal of Physical Chemistry B*, 103(40):8410–8426.
- Macke, A., Mueller, J., and Raschke, E. (1996). Single scattering properties of atmospheric ice crystals. *Journal of the Atmospheric Sciences*, 53(19):2813–2825.
- Maier, S. (2007). *Plasmonics: Fundamentals and Applications*. Springer.
- Maier, S. A. and Atwater, H. A. (2005). Plasmonics: Localization and guiding of electromagnetic energy in metal/dielectric structures. *Journal of Applied Physics*, 98(1):9.

- Mandlebrot, B. (1982). *The Fractal Geometry of Nature*. Freeman, New York.
- Metzger, B., Hentschel, M., Lippitz, M., and Giessen, H. (2012). Third-harmonic spectroscopy and modeling of the nonlinear response of plasmonic nanoantennas. *Optics Letters*, 37(22):4741–4743.
- Metzger, B., Hentschel, M., Nesterov, M., Schumacher, T., Lippitz, M., and Giessen, H. (2016). Nonlinear optics of complex plasmonic structures: linear and third-order optical response of orthogonally coupled metallic nanoantennas. *Applied Physics B- Lasers and Optics*, 122(4).
- Mie, G. (1908). Beitrge zur optik trber medien, speziell kolloidaler metallsungen. *Annalen der Physik*, 25:377.
- Moocarme, M. (2015a). Sierpinski carpet generator. <https://github.com/moocarme/Diffractions/blob/master/Sierpinski.m>.
- Moocarme, M. (2015b). Sierpinski carpet reconstruction algorithm. <https://github.com/moocarme/Diffractions/blob/master/reconFun.m>.
- Moocarme, M., Dominguez-Juarez, J. L., and Vuong, L. T. (2014). Ultralow-intensity magneto-optical and mechanical effects in metal nanocolloids. *Nano Letters*, 14(3):1178–1183.
- Mulvaney, P. (1996). Surface plasmon spectroscopy of nanosized metal particles. *Langmuir*, 12(3):788–800.
- Ni, X., Ishii, S., Kildishev, A. V., and Shalaev, V. M. (2013). Ultra-thin, planar, Babinet-inverted plasmonic metalenses. *Light: Science & Applications*, 2.
- Niemiinen, T. A., Knorer, G., Heckenberg, N. R., and Rubinsztein-Dunlop, H. (2007). Physics of optical tweezers. In Berns, MW and Greulich, KO, editor, *Laser Manipulation of Cells and Tissues*, volume 82 of *Methods in Cell Biology*, pages 207–236. Elsevier Academic Press Inc.
- Nikolajsen, T., Leosson, K., and Bozhevolnyi, S. (2004). Surface plasmon polariton based modulators and switches operating at telecom wavelengths. *Applied Physics Letters*, 85(24):5833–5835.
- Novotny, L., Bian, R. X., and Xie, X. S. (1997). Theory of nanometric optical tweezers. *Physical Review Letters*, 79:645–648.
- Owen, G. and Rissman, P. (1983). Proximity Effect Correction for Electron-Beam Lithography by Equalization of Background Dose. *Journal of Applied Physics*, 54(6):3573–3581.
- Ozbay, E. (2006). Plasmonics: Merging photonics and electronics at nanoscale dimensions. *Science*, 311(5758):189–193.

- Paterson, L., MacDonald, M., Arlt, J., Sibbett, W., Bryant, P., and Dholakia, K. (2001). Controlled rotation of optically trapped microscopic particles. *Science*, 292(5518):912–914.
- Petrich, W., Grieser, M., Grimm, R., Gruber, A., Habs, D., Miesner, H., Schwalm, D., Wanner, B., Wernoe, H., Wolf, A., Grieser, R., Huner, G., Klein, R., Kuhl, T., Neumann, R., and Schroder, S. (1993). Laser cooling of stored high-velocity ions by means of the spontaneous force. *Physical Review A*, 48(3):2127–2144.
- Pineider, F., Campo, G., Bonanni, V., Fernandez, C. d. J., Mattei, G., Caneschi, A., Gatteschi, D., and Sangregorio, C. (2013). Circular magnetoplasmonic modes in gold nanoparticles. *Nano Letters*, 13(10):4785–4789.
- Plum, E., Fedotov, V. A., and Zheludev, N. I. (2011). Asymmetric transmission: a generic property of two-dimensional periodic patterns. *Journal of Optics*, 13(2):024006.
- Plum, E., Fedotov, V. A., and Zheludev, N. I. (2016). Specular optical activity of achiral metasurfaces. *Applied Physics Letters*, 108(14).
- Prodan, E., Radloff, C., Halas, N., and Nordlander, P. (2003). A hybridization model for the plasmon response of complex nanostructures. *Science*, 302(5644):419–422.
- Proscia, N. V., Moocarme, M., Chang, R., Kretzschmar, I., Menon, V. M., and Vuong, L. T. (2016). Control of photo-induced voltages in plasmonic crystals via spin-orbit interactions. *Optics Express*, 24(10).
- Prosvirnin, S. L. and Zheludev, N. I. (2005). Polarization effects in the diffraction of light by a planar chiral structure. *Physical Review E*, 71:037603.
- Puente-Baliarda, C., Romeu, J., Pous, R., and Cardama, A. (1998). On the behavior of the Sierpinski multiband fractal antenna. *IEEE Transactions on Antennas and Propagation*, 46(4):517–524.
- Qin, F., Ding, L., Zhang, L., Monticone, F., Chum, C. C., Deng, J., Mei, S., Li, Y., Teng, J., Hong, M., Zhang, S., Alù, A., and Qiu, C.-W. (2016). Hybrid bilayer plasmonic metasurface efficiently manipulates visible light. *Science Advances*, 2(1).
- Radonic, V., Palmer, K., Stojanovic, G., and Crnojevic-Bengin, V. (2012). Flexible Sierpinski Carpet Fractal Antenna on a Hilbert Slot Patterned Ground. *International Journal of Antennas and Propagation*.
- Raja, M., Allen, D., and Sisk, W. (1995). Room-temperature inverse faraday effect in terbium gallium garnet. *Applied Physics Letters*, 67(15):2123–2125.
- Rakic, A., Djurisic, A., Elazar, J., and Majewski, M. (1998). Optical properties of metallic films for vertical-cavity optoelectronic devices. *Applied Optics*, 37(22):5271–5283.

- Ruffner, D. B. and Grier, D. G. (2012). Optical conveyors: A class of active tractor beams. *Physical Review Letters*, 109:163903.
- Saija, R., Denti, P., Borghese, F., Maragò, O. M., and Iatì, M. A. (2009). Optical trapping calculations for metal nanoparticles. Comparison with experimental data for Au and Ag spheres. *Optics Express*, 17(12):10231–10241.
- Savitzky, A. and Golay, M. J. E. (1964). Smoothing and differentiation of data by simplified least squares procedures. *Analytical Chemistry*, 36(8):1627–1639.
- Schmitt, J. M. and Kumar, G. (1998). Optical scattering properties of soft tissue: a discrete particle model. *Applied Optics*, 37(13):2788–2797.
- Schnatterly, S. E. (1969). Magnetoreflection measurements on the noble metals. *Physical Review*, 183:664–667.
- Segev, M., Soljacic, M., and Dudley, J. M. (2012). Fractal optics and beyond. *Nature Photonics*, 6(4):209–210.
- Sepulveda, B., Gonzalez-Diaz, J. B., Garcia-Martin, A., Lechuga, L. M., and Armelles, G. (2010). Plasmon-induced magneto-optical activity in nanosized gold disks. *Physical Review Letters*, 104(14):147401.
- Shaltout, A., Liu, J., Shalaev, V. M., and Kildishev, A. V. (2014). Optically Active Metasurface with Non-Chiral Plasmonic Nanoantennas. *Nano Letters*, 14(8):4426–4431.
- Shelton, W., Bonin, K., and Walker, T. (2005). Nonlinear motion of optically torqued nanorods. *Physical Review E*, 71(3):036204.
- Shvedov, V. G., Rode, A. V., Izdebskaya, Y. V., Desyatnikov, A. S., Krolikowski, W., and Kivshar, Y. S. (2010). Giant optical manipulation. *Physical Review Letters*, 105:118103–118107.
- Singh, N. D., Moocarme, M., Edelstein, B., Punnoose, N., and Vuong, L. T. (2012). Anomalously-large photo-induced magnetic response of metallic nanocolloids in aqueous solution using a solar simulator. *Optics Express*, 20(17):19214–19225.
- Slepyan, G. Y., Shuba, M. V., Maksimenko, S. A., and Lakhtakia, A. (2006). Theory of optical scattering by achiral carbon nanotubes and their potential as optical nanoantennas. *Physical Review B*, 73:195416.
- Soljacic, M., Segev, M., and Menyuk, C. (2000). Self-similarity and fractals in soliton-supporting systems. *Physical Review E*, 61(2):R1048–R1051.
- Sorensen, C. M. (2001). Light scattering by fractal aggregates: A review. *Aerosol Science and Technology*, 35(2):648–687.

- Stockman, M. I., Shalaev, V. M., Moskovits, M., Botet, R., and George, T. F. (1992). Enhanced raman scattering by fractal clusters: Scale-invariant theory. *Physical Review B*, 46:2821–2830.
- Strogatz, S. H. (1994). *Nonlinear dynamics and chaos : with applications to physics, biology, chemistry, and engineering*. Studies in nonlinearity. Westview Press, Cambridge (Mass.). Autre(s) tirage(s) : 2000.
- Tang, C. J., Zhan, P., Cao, Z. S., Pan, J., Chen, Z., and Wang, Z. L. (2011). Magnetic field enhancement at optical frequencies through diffraction coupling of magnetic plasmon resonances in metamaterials. *Physical Review B*, 83(4):041402.
- Tang, J., Xiao, Z., Xu, K., Ma, X., Liu, D., and Wang, Z. (2016). Cross polarization conversion based on a new chiral spiral slot structure in thz region. *Optical and Quantum Electronics*, 48(2):1–11.
- Temnov, V. V., Armelles, G., Woggon, U., Guzatov, D., Cebollada, A., Garcia-Martin, A., Garcia-Martin, J.-M., Thomay, T., Leitenstorfer, A., and Bratschitsch, R. (2010). Active magneto-plasmonics in hybrid metal-ferromagnet structures. *Nature Photonics*, 4(2):107–111.
- Tong, L., Miljkovic, V. D., and Kall, M. (2010). Alignment, rotation, and spinning of single plasmonic nanoparticles and nanowires using polarization dependent optical forces. *Nano Letters*, 10(1):268–273. PMID: 20030391.
- Torrado, J. F., Gonzalez-Diaz, J. B., Gonzalez, M. U., Garcia-Martin, A., and Armelles, G. (2010). Magneto-optical effects in interacting localized and propagating surface plasmon modes. *Optics Express*, 18(15):15635–15642.
- Tsai, D. P., Kovacs, J., Wang, Z., Moskovits, M., Shalaev, V. M., Suh, J. S., and Botet, R. (1994). Photon scanning tunneling microscopy images of optical excitations of fractal metal colloid clusters. *Physical Review Letters*, 72:4149–4152.
- Tsai, W.-Y., Huang, J.-S., and Huang, C.-B. (2014). Selective trapping or rotation of isotropic dielectric microparticles by optical near field in a plasmonic archimedes spiral. *Nano Letters*, 14(2):547–552.
- Unnikrishnan, G., Joseph, J., and Singh, K. (2000). Optical encryption by double-random phase encoding in the fractional Fourier domain. *Optics Letters*, 25(12):887–889.
- Van Thourhout, D. and Roels, J. (2010). Optomechanical device actuation through the optical gradient force. *Nature Photonics*, 4(4):211–217.
- Velev, O. D. and Bhatt, K. H. (2006). On-chip micromanipulation and assembly of colloidal particles by electric fields. *Soft Matter*, 2:738–750.

- Verma, R., Banerjee, V., and Senthilkumaran, P. (2012). Redundancy in Cantor Diffractals. *Optics Express*, 20(8):8250–8255.
- Verma, R., Sharma, M. K., Banerjee, V., and Senthilkumaran, P. (2013). Robustness of Cantor Diffractals. *Optics Express*, 21(7):7951–7956.
- Vuong, L. T., Adam, A. J. L., Brok, J. M., Planken, P. C. M., and Urbach, H. P. (2010). Electromagnetic spin-orbit interactions via scattering of subwavelength apertures. *Physical Review Letters*, 104(8):083903.
- Weiner, J., Bagnato, V., Zilio, S., and Julienne, P. (1999). Experiments and theory in cold and ultracold collisions. *Reviews of Modern Physics*, 71(1):1–85.
- Wu, X., Meng, Y., Wang, L., Tian, J., Dai, S., and Wen, W. (2016). Anisotropic metasurface with near-unity circular polarization conversion. *Applied Physics Letters*, 108(18).
- Yan, Z., Jureller, J. E., Sweet, J., Guffey, M. J., Pelton, M., and Scherer, N. F. (2012a). Three-dimensional optical trapping and manipulation of single silver nanowires. *Nano Letters*, 12(10):5155–5161.
- Yan, Z., Pelton, M., Vigderman, L., Zubarev, E. R., and Scherer, N. F. (2013a). Why single-beam optical tweezers trap gold nanowires in three dimensions. *ACS Nano*, 7(10):8794–8800.
- Yan, Z. and Scherer, N. F. (2013). Optical vortex induced rotation of silver nanowires. *Journal of Physical Chemistry Letters*, 4(17):2937–2942.
- Yan, Z., Shah, R. a., Chado, G., Gray, S. K., Pelton, M., and Scherer, N. F. (2013b). Guiding spatial arrangements of silver nanoparticles by optical binding interactions in shaped light fields. *ACS Nano*, 7(2):1790–1802.
- Yan, Z., Sweet, J., Jureller, J. E., Guffey, M. J., Pelton, M., and Scherer, N. F. (2012b). Controlling the position and orientation of single silver nanowires on a surface using structured optical fields. *ACS Nano*, 6(9):8144–8155.
- Yang, S., Liu, Z., Xia, X., E, Y., Tang, C., Wang, Y., Li, J., Wang, L., and Gu, C. (2016). Excitation of ultrasharp trapped-mode resonances in mirror-symmetric metamaterials. *Physical Review B*, 93(23).
- Yannopapas, V. (2009). Circular dichroism in planar nonchiral plasmonic metamaterials. *Optics Letters*, 34(5):632–634.
- Yu, N., Genevet, P., Kats, M. A., Aieta, F., Tetienne, J.-P., Capasso, F., and Gaburro, Z. (2011). Light Propagation with Phase Discontinuities: Generalized Laws of Reflection and Refraction. *Science*, 334(6054):333–337.

- Zhang, S., Wei, H., Bao, K., Håkanson, U., Halas, N. J., Nordlander, P., and Xu, H. (2011). Chiral surface plasmon polaritons on metallic nanowires. *Physical Review Letters*, 107:096801.
- Zhang, W., Zhu, W. M., Chia, E. E. M., Shen, Z. X., Cai, H., Gu, Y. D., Ser, W., and Liu, A. Q. (2014). A pseudo-planar metasurface for a polarization rotator. *Optics Express*, 22(9):10446–10454.
- Zhao, Y. and Alu, A. (2011). Manipulating light polarization with ultrathin plasmonic metasurfaces. *Physical Review B*, 84(20).